FAKULTÄT FÜR PHYSIK
Institute for Photon Science
and Synchrotron Radiation (IPS)

Non-local and non-linear aspects of Fresnel diffractograms

(Nicht lokale und nicht lineare Aspekte von Fresnel Diffraktogrammen)

Master thesis
of

Fabian Trost

at the Institute for Photon Science
and Synchrotron Radiation (IPS)

Reviewer:	Prof. Dr. T. Baumbach
Second Reviewer:	PD Dr. R. Hofmann

Erklärung zur Selbstständigkeit

Ich versichere, dass ich diese Arbeit selbstständig verfasst habe und keine anderen als die angegebenen Quellen und Hilfsmittel benutzt habe, die wörtlich oder inhaltlich übernommenen Stellen als solche kenntlich gemacht und die Satzung des KIT zur Sicherung guter wissenschaftlicher Praxis in der gültigen Fassung vom 17.05.2010 beachtet habe.

Karlsruhe, den 12.06.2017, _____

Fabian Trost

Als Ansichtsexemplar genehmigt von

Karlsruhe, den 12.06.2017, _____

Prof. Dr. T. Baumbach

In this master thesis we have investigated the propagation of a phase-modulated electo-magnetic wave field through free space and subject to paraxial approximation (Fresnel theory). A good understanding of the diffractograms' (spectrum of the propagated intensity contrast) dependencies on propagation distance and phase-variation strength is essential to classify common phase-retrieval approaches, to point out their limitations and to propose improvements.
We identify a critical transition between an over-damped and an oscillatory spectral shape of the diffractogram depending on propagation distance and phase-variation strength. Also, we spectrally analyze scaling linearity (how linearly the diffractogram responds to a scaling of the phase-map). In case of a Gausian phase-map we can identify a single physical frequency modulus where the diffractogram scales in the most linear way. Furthermore, we identify regions within more general diffractogram where good scaling-linearity takes place. We investigate commonly applied single-distance phase-retrieval approaches (TIE and CTF) with respect to the modulation transfer and we demonstrate how this knowledge of scaling-linearity can be applied to improve linear phase-retrieval algorithms.

In der vorliegenden Masterarbeit untersuchen wir die Propagation eines phasenmodulierten Wellenfeldes einer elektromagnetischen Welle im freien Raum, im Rahmen der paraxialen Näherung (Fresnel-Theorie). Ein gutes Verständnis über die Abhängigkeit des Diffraktogram (Spektrum des propergierten Intensitätskontrast) von der Propagationsdistanz und der Stärke der Phasenvariation ist essenziell um Phasenrekonstruktionsmethoden zu klassifizieren und deren Beschränkungen aufzuzeigen.
Wir identifizieren einen kritischen Übergang von einer überdämpften zu einer oszillierenden Form des spektralen Diffraktograms in Abhängigkeit der Propagationsdistanz und der Stärke der Phasenvariation. Des Weiteren analysieren wir die spektrale Skalierungslinearität (in wie fern das Diffraktogram linear mit der Stärke der Phasenvariation skaliert). Im Falle einer gaussförmigen Phasenkarte können wir eine physikalische Frequenz isolieren, in welcher das Diffraktogram maximal linear skaliert. Des Weiteren identifizieren wir Regionen im Diffraktogram die eine gute Skalierungslinearität zeigen. Wir untersuchen die bekannten Phasenrekonstruktionsansätze (TIE und CTF) auf ihr Abbildungsvermögen räumlicher Frequenzen und wenden unsere Erkenntnisse über Skalierungslinearität an, um lineare Phasenrekonstruktionsalgorithmen zu verbessern.

Contents

List of Figures

List of Tables

1. Introduction

The discovery of X-rays in 1895 by Wilhelm Conrad Röntgen [1] has laid the foundation for a large amount of imaging methods in medicine, biology, material science and many more. In comparison to visible light, X-rays permeate matter, especially soft matter (with low atomic number), very well. This, for example, was demonstrated in 1896, when X-ray imaging was first applied in clinical use [2].
The X-ray's high energy imply negligibly small scattering of X-ray beams of soft, non-crystalline matter, and therefore is used for projection radiography. Highly absorbing tissues, for example bones or kidney stones, can be visualized as 2D projection in the human body. With the development of powerful computers, projected X-ray images can be used to calculate three-dimensional representations of the probed objects. This computed tomography has first been implemented by Godfrey Hounsfield in 1969 based on the mathematical work of Allan McLeod Cormack [3]. This time neither Cormack nor Hounsfield knew that the inverse problem of projection had already been solved by Johann Radon in 1917 [4].
Nowadays, modern synchrotron radiation facilities can produce X-rays of high brilliance and coherence. Synchrotrons generate high intensity, monochromatic X-ray beams with good spatial- and temporal coherence. With these beams, it is possible to perform phase-contrast imaging. When the beam passes though a sample, with the refractive index $n = 1 - \delta + i\beta$ (with the absorption part β), the wave front is modulated. The induced modulations are given by line integrals of the refractive index along the beam path when considering a sufficiently thin sample. When the modulated wave front propagates to the detector the 2D intensity distribution changes by self interference in dependency of the propagation distance. This propagation is well described by Fresnel theory [5]. Self-interference enables the use of this effect for phase-retrieval, since it is not possible to measure the phase directly (for X-rays at energies of 1keV the electromagnetic field oscillates on a frequency of approximately $2.5 \cdot 10^{17}$Hz).
The refractive index depends on the energy of the probing photons. In Figure 1.1, for example, the refractive index, split in real and imaginary part, of water is plotted as a function of the energy. We see that the ratio δ/β increases for higher energies. Therefore phase-contrast imaging is a possibility to reduce dose, which in particular is important for biological and medical imaging.
The phase-retrieval, based on a single-distance measurement, requires a good understanding of how the intensity contrast changes during the propagation. The present Master Thesis investigates the intensity-contrast spectrum as induced by the projection through pure-phase objects (phase-maps) and subsequent free-space propagation. We start with simple phase-maps (single scale objects) and then increase their complexity. The main focus of the investigations is how the spectra depend on the strength of the phase variation. This is of special interest because the commonly used phase-retrieval approaches (TIE and CTF) presume that the strength of phase variation scales linear with the strength of the diffractogram (Fourier transformed intensity contrast after propagation). Interesting results are e.g., that the shape of the (angular averaged) diffractogram transmutes critically from an damped to an oscillatory form when increasing the propagation distance and/or reducing the phase-variation strength. Also, regions where the diffractrogram scales linearly and where it does not, are identified.

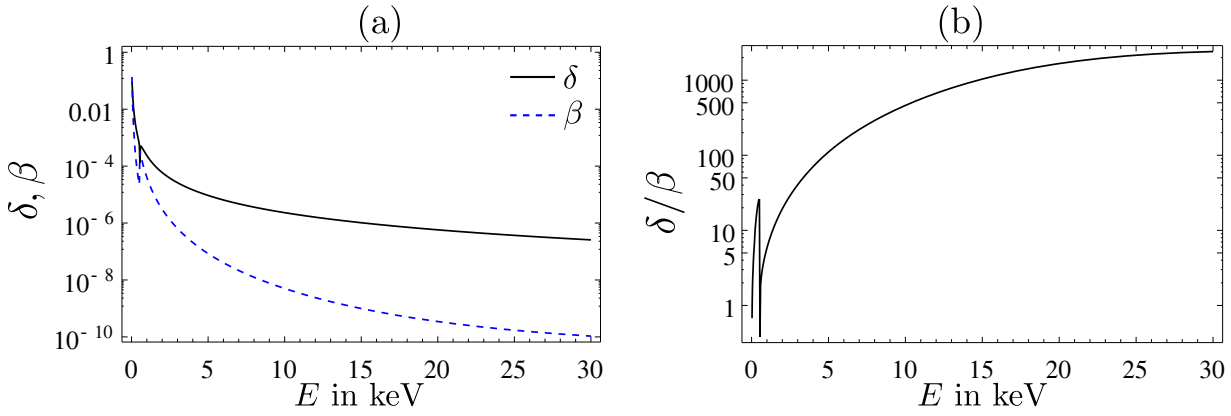

Figure 1.1.: Refractive index of water parameterized by $n = 1 - \delta + i\beta$ as a function of the photon energy $E = \hbar\omega$. (a): δ and β as function of E. (b): Ratio δ/β as function of E. Note that δ/β increases for higher energies. Data from [6]

This thesis itself is structured as follows:
In Chapter 2 we introduce the theoretical background of Fresnel theory. Beginning with Maxwells equation in Section 2.1.1, we deduce the Helmholtz propagator and, by applying the paraxial approximation, the Fresnel propagator in Section 2.1.7. Section 2.2.2 is a short excursion on tomographic reconstruction using the filtered back projection. Guigay's relation between the wave field after the projection through the sample and the intensity contrast at the detector plane is stated and proofed in Section 2.2.3, laying the foundation of the phase-retrieval approaches introduced in Section 2.2.4.
Chapter 3 contains the investigations of the diffractograms. We focus on the effect of phase-variation scaling on the diffractogram.
In Section 3.1 we start our analysis on single scale objects with broad spectrum (SOBS). After introducing a formalism to calculate the diffractogram of a Gaussian phase-map in Section 3.1.1 we investigate the appearance of an additional zero in the low frequency regime in the diffractogram. Section 3.1.2 discusses how the shape of SOBS diffractograms' becomes universal in the extreme far field and that the shape information condenses in scaling information. In Section 3.1.3 the transmutation of the SOBS diffractogram from an over-damped to an oscillatory shape in dependence of the Fresnel number and the scaling factor is investigated. A measure of scaling linearity is introduced in Section 3.1.4. With this measure we identify a single physical frequency at which the SOBS diffractogram scales in a maximally linear way. Also, we identify bands of good scaling linearity in the diffractogram.
We increase the complexity of our phase-map and study two scale objects with broad spectrum (TOBS) in Section 3.2. Thereby we investigate the transition from over-damped to oscillatory behavior of the diffractogram and the movement of the first regular zero as a function of phase-variation strength in Section 3.2.1. Section 3.2.2 contains an investigation on scaling linearity in dependence of the shape of the phase-map. In Section 3.2.3 the extreme far field is discussed and a generalization of diffractograms in the extreme far field for arbitrary phase-maps is introduced.
In Section 3.3 we study the diffractograms induced by multi-scale objects with broad spectrum (MOBS). In analogy to the SOBS and TOBS case we identify bands of linear scaling behavior in Section 3.3.2. We also study phase retrieval approaches in dependence of the phase-variation strength and the propagation distance in Section 3.3.3. Therefore, we perform a systematical investigation on how well the phase retrieval approaches perform in dependence of spatial frequency in the phase-map.
In Chapter 4 we summarize our outcomes, with the focus on the impact on single-distance phase retrieval.

2. Theoretical background

This chapter is about the basics of x-ray imaging and phase-to-contrast transfer. We start with Maxwell's equations and derive phase to contrast transfer (Guigay's relation). We also briefly address tomographic reconstruction and phase retrieval.

2.1. From Maxwell to Fresnel

This section contains the fundamentals of electro magnetic waves and an introduction into some useful approximations for the x-ray regime. Also, the propagation of a monochromatic wave in free space will be discussed and the free-space propagator will be derived. This propagator underlies the derivation of phase to intensity transfer. Therefore, it is at the heart of phase-contrast x-ray imaging.

2.1.1. Macroscopic Maxwell's equations

The most fundamental description of electro magnetic phenomena in classical physics is given by Maxwell's equations [7], in the SI unit system, which will be used in this thesis:

$$\begin{aligned} \nabla \cdot \vec{E} &= \frac{\rho}{\varepsilon_0}\,, \\ \nabla \cdot \vec{B} &= 0\,, \\ \nabla \times \vec{E} + \partial_t \vec{B} &= 0\,, \\ \nabla \times \vec{B} - \mu_0 \varepsilon_0 \partial_t \vec{E} &= \mu_0 \vec{j}\,. \end{aligned} \tag{2.1}$$

These partial differential equations connect the electric charge density ρ and electric current density $\vec{j}$ with the electric field $\vec{E}$ and the magnetic field $\vec{B}$. The physical constants μ_0 and ε_0 are called the vacuum permeability and the vacuum permittivity, respectively[8].
When electromagnetic effects are used to probe materials, like in x-ray imaging, it is obvious that the effect of matter has to be considered. To cope with this in an efficient way, one introduce material properties. For the sake of simplification we impose some restrictions on the material. The first restriction is that only dielectric materials are considered. This means that the material is an electric insulator which can be polarized. Assuming a homogeneous and linear medium, the polarisation $\vec{P}$ is proportional to $\vec{E}$

$$\vec{P} = \varepsilon_0 \chi_\mathrm{e} \vec{E}\,. \tag{2.2}$$

The dimensionless factor χ_e denotes the electric susceptibility χ_e (in the vacuum $\chi_\mathrm{e} = 1$). In general χ_e is a 3D-tensor.

With this polarisation the electric flux density can be defined as

$$\vec{D} := \varepsilon_0 \vec{E} + \vec{P}\,. \tag{2.3}$$

In case of a linear and isotropic dielectric material this relation can be simplified as

$$\vec{D} := \varepsilon_\mathrm{r}\varepsilon_0\vec{E}\,, \tag{2.4}$$

containing the relative permittivity ε_r as a scalar and dimensionless quantity.

In analogy to the relation between $\vec{E}$ and $\vec{D}$, there is a relation between the magnetic field strength $\vec{H}$ and the magnetic flux density $\vec{B} := \mu_\mathrm{r}\mu_0\vec{H}$, including a material dependent, dimensionless tensor μ_r. In case of magnetic isotropy μ_r collapses to a scalar quantity.

With these definitions, Maxwell's equations in matter can be written as

$$\begin{aligned} \nabla\cdot\vec{D} &= \rho_\mathrm{free}\,,\\ \nabla\cdot\vec{B} &= 0\,,\\ \nabla\times\vec{E}+\partial_t\vec{B} &= 0\,,\\ \nabla\times\vec{H}-\partial_t\vec{D} &= \vec{j}_\mathrm{free}\,, \end{aligned} \tag{2.5}$$

including the free electric charges[1] ρ_free and free electric currents $\vec{j}_\mathrm{free}$.

2.1.2. Wave equation and refractive index

Before setting up the wave equations, some assumptions have to be made: the medium is isotropic and has no free charges or free currents ($\rho_\mathrm{free}=0$; $\vec{j}_\mathrm{free}=0$). With these assumptions, the wave equations for $\vec{E}$ and $\vec{H}$ can be derived form Eq. (2.5) as

$$\begin{aligned} \left(\varepsilon_\mathrm{r}\mu_\mathrm{r}\,\varepsilon_0\mu_0\,\partial_\mathrm{t}^2-\triangle\right)\vec{E} &= 0\,,\\ \left(\varepsilon_\mathrm{r}\mu_\mathrm{r}\,\varepsilon_0\mu_0\,\partial_\mathrm{t}^2-\triangle\right)\vec{H} &= 0\,. \end{aligned} \tag{2.6}$$

These two equations can be solved independently, and for isotropic media, the vectorial character can be neglected. We also identify the vacuum speed of light in Eq. (2.6) as $c=\frac{1}{\sqrt{\varepsilon_0\mu_0}}$. This gives us the following, scalar wave equation[2] (d'Alembert equation)

$$\left(\varepsilon_\mathrm{r}\mu_\mathrm{r}\frac{1}{c^2}\partial_\mathrm{t}^2-\triangle\right)\Psi(\vec{x},t)=0\,. \tag{2.7}$$

For monochromatic waves applies

$$\frac{\omega^2}{v^2}-\vec{k}_\omega^{\,2}=0\,, \tag{2.8}$$

where $v=\frac{c}{\sqrt{\varepsilon_\mathrm{r}\mu_\mathrm{r}}}$ denotes the phase velocity, ω the angular frequency and the wave vector $\vec{k}_\omega$. In this case Eq. (2.7) can be solved by

$$\psi_\omega(\vec{x}) = |\psi_\omega|e^{-i\omega t-\vec{k}_\omega\vec{x}}\,. \tag{2.9}$$

When looking at electromagnetic waves in media, it is useful to introduce the refractive index n as the ratio between the vacuum speed of light to the phase velocity v in the medium:

$$n := \frac{c}{v}\,. \tag{2.10}$$

[1] Free electric charge means moveable over macroscopic distances.
[2] Ψ can stand for E or H, we consider the E field only.

In general, n is a function of angular frequency ω of the monochromatic light wave described by Eq. (2.9). When $\partial_\omega n(\omega) \neq 0$ we call the medium dispersive. For example, the fact that glass is a dispersive medium is easily demonstrated by simple white light being broken by a prism into its constituent spectral components. This effect is called dispersion. While n is greater than one for visible light for a large variety of media. In the x-ray regime[3] ($5 - 30$keV) it is usually smaller than one but remains close to unity. Therefore, it is convenient to parametrise n as follows for x-rays

$$n = 1 - \delta + i\beta\,. \tag{2.11}$$

The imaginary part of n, quantified by β, is used to describe the absorption of the medium. Its function will become clear in Section 2.2.1. For energies around 10keV, δ is usually of the order of 10^{-5}. For example δ and β as well as the relation $\frac{\delta}{\beta}$ of water as a function of energy is given in Figure 1.1.

2.1.3. Helmholtz equation

It is possible to factor out the time dependent part of Ψ from Eq. (2.7) to build a superposition of monochromatic waves as

$$\Psi(\vec{x}, t) = \int_0^\infty \psi_\omega(\vec{x}) \cdot e^{-i\omega t} d\omega\,. \tag{2.12}$$

We can now look at each frequency separately, and, by substituting Eq. (2.12) in Eq. (2.7), this yields the Helmholtz equation as

$$\left(\triangle + n^2 K^2\right)\psi = 0\,, \tag{2.13}$$

where the vacuum wave number K is defined as $K = \frac{\omega}{c} = |\vec{K}| = \frac{2\pi}{\lambda}$ with the wave length λ.

When substituting[4] $n = \sqrt{1 + \chi(\vec{x})}$ we obtain

$$\left(\triangle + (1 + \chi(\vec{x}))K^2\right)\psi = 0\,. \tag{2.14}$$

To solve this homogeneous and linear differential equation we first consider the vacuum case ($\chi = 0$), called the free Helmholtz equation

$$(\triangle + K^2)\psi_0 = 0 \tag{2.15}$$

and the associated Green's function

$$(\triangle + K^2)G_0(\vec{x} - \vec{x'}) = \delta^{(3)}(\vec{x} - \vec{x'})\,. \tag{2.16}$$

When ψ_0 and G_0 are known, a formal solution for ψ can be generated as follows[5]

$$\psi(\vec{x}) = \psi_0(\vec{x}) - K^2 \int \chi(\vec{x'}) G_0(\vec{x} - \vec{x'}) \psi(\vec{x'}) d^3x'\,. \tag{2.17}$$

[3] The hardness of a x-ray beam is usually quantified by the energy of the light quanta (photons) it contains with $E = \frac{hc}{\lambda}$, where λ is the wave length and h the Planck constant.

[4] Note that $\chi(\vec{x})$ is used to parameterize n and is not equal to χ_e in Eq. (2.2)

[5] Proof by substitution of Eq.(2.17) into Eq.(2.14): $(\triangle + K^2)\psi(\vec{x}) = 0 - K^2 \int \delta(\vec{x} - \vec{x'})\chi(\vec{x'})\psi(\vec{x'})d^3x' = -K^2\chi(\vec{x})\psi(\vec{x})$.

2.1.4. Kirchhoff-Helmholtz integral theorem

Because it is useful for an eventual reduction of the Helmholtz to Fresnel theory we consider an integral theorem which is based on the free Helmholtz equation (2.15). In general, for two scalar functions $g(\vec{x})$ and $f(\vec{x})$ one has

$$\nabla(g\nabla f) = g\triangle f + (\nabla g)\cdot(\nabla f) \Rightarrow \nabla(g\nabla f - f\nabla g) = g\triangle f - f\triangle g\,. \tag{2.18}$$

Using Stokes' theorem[6] we obtain

$$\int_\Omega (g\triangle f - f\triangle g)d^3x = \int_{\partial\Omega}\left(g\frac{\partial f}{\partial\hat{n}} - f\frac{\partial g}{\partial\hat{n}}\right)dS\,, \tag{2.19}$$

where $\partial\hat{n}$ denotes the derivative normal to the surface $\partial\Omega$ given by $\partial\hat{n} = \hat{n}\cdot\nabla$. This equation is Green's second vector identity and can be applied to the Green's function, $g = G_0(\vec{x} - \vec{x'})$, and the free-space solution of the Helmholtz equation, $f = \psi_0(\vec{x'})$, from Eq. (2.15) and Eq. (2.16). Therefore, Eq.(2.19) becomes

$$\int_{\partial\Omega}\left(G_0\partial_{\hat{n}'}\psi_0 - \psi_0\partial_{\hat{n}'}G_0\right)dS' = \int_\Omega\left(G_0\triangle\psi_0 - \psi_0\triangle G_0\right)d^3x'\,. \tag{2.20}$$

The term on the right hand side can be modified with a little trick: We add zero in terms of $G_0K\psi_0 - \psi_0KG_0 = 0$ and obtain

$$\int_\Omega\Big(G_0(\triangle + K^2)\psi_0 - \psi_0(\triangle + K^2)G_0\Big)\,d^3x' = -\int_\Omega \delta^{(3)}(\vec{x} - \vec{x'})\psi_0(\vec{x'})d^3x' = -\psi_0(\vec{x}),\ \vec{x}\,\epsilon\,\Omega\,. \tag{2.21}$$

By integrating the right hand side, we receive the "Kirchhoff-Helmholtz integral theorem"[10]:

$$\int_{\partial\Omega}\Big(G_0(\vec{x} - \vec{x'})\partial_{\hat{n'}}\psi_0(\vec{x'}) - \psi_0(\vec{x'})\partial_{\hat{n'}}G_0(\vec{x} - \vec{x'})\Big)\,dS' = -\psi_0(\vec{x}),\ \forall\ \vec{x}\ \epsilon\ \Omega\,. \tag{2.22}$$

This theorem states that the wave function ψ_0 inside of Ω is determined by its values and its derivatives on the boundary $\partial\Omega$ as well as by the Green's function G_0.

2.1.5. Rayleigh - Sommerfeld diffraction integral

A Green's function can be constructed in such a way that either the minuend or the subtrahend in Eq. (2.22) (left-hand side) becomes zero. Consider the half-space $z > 0$ and a boundary at $z = 0$. Furthermore, we enforce $G_{0,D}(z = 0 \text{ or } z' = 0, \vec{x}_\perp - \vec{x}'_\perp) = 0$ (first case, Dirichlet boundary condition)[7]. The Green's function can be constructed as follows:

$$G_{0,D}(z, z', \vec{x}_\perp - \vec{x}'_\perp) = G_0(z - z', \vec{x}_\perp - \vec{x}'_\perp) - G_0(z + z', \vec{x}_\perp - \vec{x}'_\perp)\,. \tag{2.23}$$

With this the minuend in Eq. (2.22) is zero:

$$\psi_0(z > 0, \vec{x}_\perp) = \int \psi_0(\vec{x}'_\perp, z' = 0)\partial_{z'}G_{0,D}(z, z' = 0, \vec{x}_\perp - \vec{x}'_\perp)d^2x'_\perp\,. \tag{2.24}$$

We call this equation the "Rayleigh - Sommerfeld integral of the first kind".

Alternatively, the Green's function can be constructed such that the subtrahend in Eq.(2.22) is zero (Neumann boundary condition), $\partial_z G_{0,\mathrm{N}}(z = 0 \text{ or } z' = 0, \vec{x}_\perp - \vec{x}'_\perp) = 0$:

$$G_{0,\mathrm{N}}(z, z', \vec{x}_\perp - \vec{x}'_\perp) = G_0(z - z', \vec{x}_\perp - \vec{x}'_\perp) + G_0(z + z', \vec{x}_\perp - \vec{x}'_\perp)\,. \tag{2.25}$$

As a consequence, we obtain the "Rayleigh - Sommerfeld integral of the second kind":

$$\psi_0(z > 0, \vec{x}_\perp) = -\int G_{0,\mathrm{N}}(z, z' = 0, \vec{x}_\perp - \vec{x}'_\perp)\partial_{z'}\psi_0(\vec{x}'_\perp, z' = 0)d^2x'_\perp\,. \tag{2.26}$$

[6] $\int_\Omega \nabla f dV = \int_{\partial\Omega} f d\vec{A}$ where $\int_{\partial\Omega} d\vec{S}$ is the integral over the boundary of some orientable manifold Ω, with $d\vec{S} = \hat{n}dS$, $\hat{n}$ denotes the normal to this boundary, and $\int_\Omega \nabla dV$ of the integral over Ω. Stokes theorem is proven in [9] p.34, ff.

[7] We split $\vec{x}$ into its z-component and the component perpendicular to z: $\vec{x} = \vec{x}_\perp + z\hat{e}_z$.

2.1.6. Green's function of Helmholtz theory in Weyl representation

Here, we introduce a useful representation of the Green's function, which can be written in term of its 3D Fourier transform as

$$G_0(\vec{x}) = \frac{1}{(2\pi)^2} \int \tilde{G}_0^K(\vec{k}) e^{i\vec{k}\vec{x}} d^3k \,. \tag{2.27}$$

This is done because Eq. (2.16) reads in Fourier space as

$$\left(-\vec{k}^2 + K^2\right) \tilde{G}_0^K(\vec{k}) - 1 = 0 \Rightarrow \tilde{G}_0^K(\vec{k}) = \frac{1}{K^2 - \vec{k}^2} \,. \tag{2.28}$$

We split $\vec{k} = \vec{k}_\perp + k_z \hat{e}_{k_z}$ in its components, and substitute Eq. (2.28) into Eq. (2.27),

$$G_0(\vec{x}) = -\frac{1}{(2\pi)^2} \int e^{i\vec{k}_\perp \vec{x}_\perp} \int \frac{e^{ik_z \cdot z}}{\vec{k}_\perp^2 + k_z^2 - K^2} dk_z d^2 dk_\perp \,. \tag{2.29}$$

The inner integral ($\int [...] dk_z$) can be carried out[8], and the Weyl representation of the Green's function Eq. (2.16) appears as follows

$$G_0(\vec{x}) = -\frac{i}{8\pi^2} \int \frac{e^{i\vec{k}_\perp \vec{x}_\perp} e^{i\sqrt{K^2 - \vec{k}_\perp^2} z}}{\sqrt{K^2 - \vec{k}_\perp^2}} dk_\perp \,. \tag{2.30}$$

2.1.7. Helmholtz and Fresnel propagator

The Green's function in Weyl representation (Eq. (2.30)) can be substituted into the Rayleigh-Sommerfeld integral of the first kind, Eq. (2.24):

$$\begin{aligned}
\psi_0(\vec{x}_\perp, z > 0) &= \int \psi_0(\vec{x}'_\perp, z' = 0)\, \partial_{z'} G_{0,D}(z, z' = 0, \vec{x}_\perp - \vec{x}'_\perp) d^2 x'_\perp \\
&= \int \psi_0(\vec{x}'_\perp, z' = 0)\, \partial_{z'} \left(G_0(z - z', \vec{x}_\perp - \vec{x}'_\perp) - G_0(z + z', \vec{x}_\perp - \vec{x}'_\perp) \right) \Big|_{z'=0} d^2 x'_\perp \\
&= -\frac{i}{8\pi^2} \int \psi_0(\vec{x}'_\perp, z' = 0) \int \frac{e^{i\vec{k}_\perp (\vec{x}_\perp - \vec{x}'_\perp)}}{\sqrt{K^2 - \vec{k}_\perp^2}} \times \\
&\partial_{z'} \left(e^{i\sqrt{K^2 - \vec{k}_\perp^2} z} e^{-i\sqrt{K^2 - \vec{k}_\perp^2} z'} - e^{i\sqrt{K^2 - \vec{k}_\perp^2} z} e^{i\sqrt{K^2 - \vec{k}_\perp^2} z'} \right) \Big|_{z'=0} d^2 k_\perp d^2 x'_\perp \\
&= \frac{1}{4\pi^2} \int \psi_0(\vec{x}'_\perp, z' = 0) \int e^{i\vec{k}_\perp (\vec{x}_\perp - \vec{x}'_\perp)} e^{i\sqrt{K^2 - \vec{k}_\perp^2} z} d^2 k_\perp d^2 x'_\perp \,.
\end{aligned} \tag{2.31}$$

This describes how a given wave field $\psi_0(\vec{x}_\perp, z = 0)$ changes (by self-interference) after propagating across a distance z. We can now identify the Helmholtz propagator P^k as the inner integral:

$$P^K(z, \vec{x}_\perp - \vec{x}'_\perp) = \frac{1}{4\pi^2} \int e^{i\vec{k}_\perp (\vec{x}_\perp - \vec{x}'_\perp)} e^{i\sqrt{K^2 - \vec{k}_\perp^2} z} d^2 k_\perp \,. \tag{2.32}$$

Using this, we can describe the propagation by calculating the 2D-convolution as

$$\psi_0(\vec{x}_\perp, z > 0) = \int \psi_0(\vec{x}'_\perp, z = 0) \cdot P^K(z, \vec{x}_\perp - \vec{x}'_\perp) d^2 x_\perp =: \psi_0(\vec{x}_\perp, z = 0) * P^K(z, \vec{x}_\perp) \,. \tag{2.33}$$

The propagator P^K also tells us something about the resolution in the far field. For $k_\perp^2 > K^2$ the exponent in $e^{i\sqrt{K^2 - \vec{k}_\perp^2} z}$ becomes real and negative. Thus perpendicular wave components, which are smaller than the wave length of the incident wave, will be suppressed in the far field. This limits

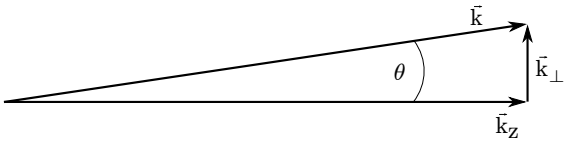

Figure 2.1.: Small-angle approximation in Fourier space $k_z \gg |\vec{k}_\perp| \Leftrightarrow \theta \ll 1$, this implies that fast oscillations of $\vec{k}_\perp$ are neglected. $|\vec{k}| \approx K$ because $|\vec{k}| > K$ is suppressed in far-field. The optical axis is the z axis.

resolution in the far field of compareable order of the wave length. For example, for x-rays the wave length is in the magnitude of 1 Ångström ($\lambda(10\text{keV}) \approx 1.24\text{Å}$).

In the following, we make the assumption that incident x-rays are propagating as plane waves along the z-direction. This means that $k_z \gg |\vec{k}_\perp|$, as illustrated in Figure 2.1. We can now approximate k_z by truncating the expansion of the square root $\sqrt{\vec{k}^2 - \vec{k}_\perp^2}$ at quadratic order in $k_\perp$

$$k_z = \sqrt{\vec{k}^2 - \vec{k}_\perp^2} \approx |\vec{k}| \left(1 - \frac{k_\perp^2}{2k^2}\right) . \tag{2.34}$$

This motivates to factor out the unscattered propagation in z-direction:

$$\psi(\vec{x}) = \tilde{\psi}(\vec{x}) e^{iKz} . \tag{2.35}$$

$\tilde{\psi}$ now represents the scattered part of the wave. Eq. (2.35) can be substituted into Eq. (2.13). Also the Laplacian can be separated into a perpendicular and parallel to z-part component $\triangle = \triangle_\perp + \partial_z^2$. Thus, we obtain

$$\left(\triangle_\perp + K^2(n^2 - 1) + 2iK\partial_z + \partial_z^2\right) \tilde{\psi}(\vec{x}) = 0 . \tag{2.36}$$

If the transverse variation of $\tilde{\psi}$ is much greater than the longitudinal variation, then the second derivative $\partial_z^2 \tilde{\psi}$ can be neglected. In this case, the wave is called beam like, and we obtain the Fresnel equation as

$$\left(\triangle_\perp + K^2(n^2 - 1) + 2iK\partial_z\right) \tilde{\psi}(\vec{x}) = 0 . \tag{2.37}$$

This equation can be interpreted as a (2+1)dimensional Schrödinger equation with the z component as time t, $-K^2(n^2 - 1)$ as the potential V, $1 \to \frac{\hbar^2}{2m}$ and $2iK = i\hbar$. Indeed, with these substitutions we obtain

$$\left(-\frac{\hbar}{2m}\triangle_\perp + V\right) \psi = i\hbar\partial_t \psi . \tag{2.38}$$

The time evolution, known from quantum mechanics, can therefore thought of as a z-evolution in Fresnel theory.

[8] This is done by using Cauchy's residue theorem $\left(\oint_\gamma f(z)dz = 2\pi i \sum_k \text{Res}(f, a_k)\right)$, because there are two poles on the k_z axis. Here we choose to include the pole at $k_z^2 = K^2 - \vec{k}_\perp^2$ and restrict the Green's function to waves with positive phase velocity in z direction.

After this little excursion, we go back to the Helmholtz propagator and apply the paraxial approximation ($K \gg k_\perp$). To do this we perform the following expansion

$$e^{i\sqrt{K^2-k_\perp^2}z} \approx e^{iKz}e^{-i\frac{k_\perp^2}{2K}z}\,, \tag{2.39}$$

compare with Eq. (2.34). This can be substituted into Eq. (2.32):

$$\bar{P}^K(z,\vec{x}_\perp - \vec{x}'_\perp) = \frac{1}{4\pi^2}e^{iKz}\int e^{i\vec{k}_\perp(\vec{x}_\perp-\vec{x}'_\perp)}e^{-i\frac{k_\perp^2}{2K}z}d^2k_\perp\,. \tag{2.40}$$

Performing the 2D Fourier transform of the Gaussian in Eq. (2.40), we obtain an expression for the Fresnel propagator $\bar{P}^K$ as

$$\bar{P}^K(z,\vec{x}_\perp - \vec{x}'_\perp) = -\frac{iK}{2\pi z}e^{iKz}e^{i\frac{K}{2z}(\vec{x}_\perp-\vec{x}'_\perp)^2}\,. \tag{2.41}$$

This propagator can be used, the same way as the Helmholtz propagator, by convolution with the wave function but now in 2D.

2.2. Guigay's relation

This section contains the basic principles of phase-contrast imaging as well as the fundamentals of phase retrieval. Also a short introduction into tomographic reconstruction will be given.

2.2.1. Projection approximation

We neglect scattering under large angles. Usually, this is a good approximation for thin objects without any long range order (which excludes crystals). When we have a look at the Fresnel equation, this approximation means that the perpendicular Laplacian can be neglected ($\triangle_\perp \to 0$). Eq.(2.37) then becomes

$$\left(2iK\partial_z + K^2(n^2-1)\right)\psi(\vec{r}) = 0\,. \tag{2.42}$$

Looking at the refractive index $n = 1 - \delta + i\beta$, we impose the restriction that n deviates very little from unity ($\delta^2 + \beta^2 \ll 1$). Thus, we can approximate: $n^2 \approx 1 - 2\delta + 2i\beta$. Substituting this into Eq. (2.42) and dividing by $2K$ we receive

$$\left(i\partial_z + K(\delta - i\beta)\right)\psi(\vec{x}_\perp, z) = 0\,. \tag{2.43}$$

This ordinary differential equation is solved by simple integration. We set the integration boundaries, specifying the thickness of the projected object, as $[-a, 0]$. This yields

$$\begin{aligned}\psi(\vec{x}_\perp, z=0) &= \psi(\vec{x}_\perp, z=-a)e^{-ik\int_{-a}^{0}(\delta(\vec{x}_\perp,z')-i\beta(\vec{x}_\perp,z'))dz'} \\ &= \psi(\vec{x}_\perp)e^{i\phi(\vec{x}_\perp)-B(\vec{x}_\perp)}\,.\end{aligned} \tag{2.44}$$

Here the intensity contrast at $z = 0$ is determined by $B(\vec{x}_\perp)$ and the phase-shift by $\phi(\vec{x}_\perp)$, as the projection of the refractive index n parallel to the z-axis. In what follows, $\phi(\vec{x}_\perp, z = 0)$ is referred to as "phase-map".

2.2.2. Tomographic reconstruction

In the previous section we have described the projection through an sample characterized by $\mu(\vec{x})$. Here we consider a more general representation $\mu(x, y, z)$ which induce intensity contrast, phase contrast or any projectable quantity. For the reconstruction we need a stack of projection data, which can be, for example, obtained by rotating the sample between the projections. Here we set x, y and z as coordinates of the samples reference system. We are projecting though the x-y plane, and we will treat it as an 2D problem ($\mu(x, y)$). Resolving in z could be obtained by either moving the sample or the projecting parallel beam along z but this is not part of the discussion in this section. An illustration of a possible setting is given in Figure 2.2. We can define the projection under a certain angle as transition from the coordinate system (x, y) to a new system (θ, s). Therefore it is convenient to consider a fixed angel θ and realize the coordinate transformation $(x, y) \to (r', s)$ as

$$\begin{aligned}x(r') &= r'\cos\theta + s\sin\theta\,, \\ y(r') &= r'\sin\theta - s\cos\theta\,.\end{aligned} \tag{2.45}$$

With this parametrisation the transformation can be formulated as

$$P_\theta(s) = \int \mu\left(r'\cos\theta + s\sin\theta, r'sin\theta - s\cos\theta\right)dr'\,, \tag{2.46}$$

which, in turn, is expressible as

$$P_\theta(s) = \int\int \mu(x, y)\delta(s - x\sin\theta + y\cos\theta)dxdy\,. \tag{2.47}$$

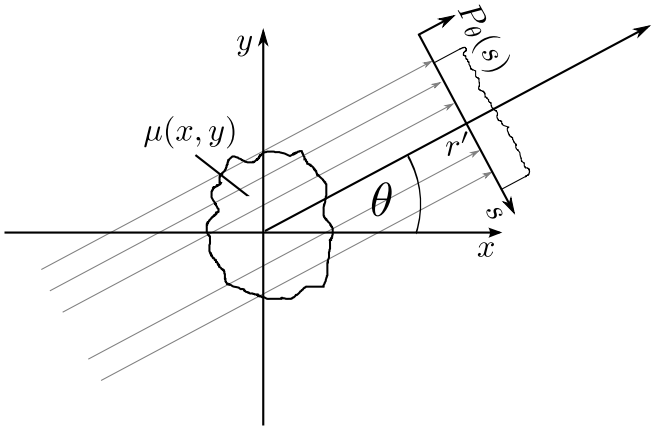

Figure 2.2.: Illustration of a projection through a sample under a certain angle θ. Such a projection is a transformation from $\mu(x,y)$ to $P(\theta,s)$, which is called Radon transform of $\mu(x,y)$.

We want to prove the equality of Eq.(2.46) and Eq. (2.47) by looking at the case $\theta = 0$ at first

$$P_{\theta=0}(s) = \int\int \mu(x,y)\delta(s+y)dxdy = \int \mu(x,-s)dx\,, \tag{2.48}$$

which is Eq. (2.46) with $\theta = 0$. We can restore the case of arbitrary θ by rotating the reference frame by $\theta' = -\theta$. This yields after transformation (rotation with $x = x'\cos\theta' - y\sin\theta'$; $y = x'\sin\theta' + y'\cos\theta'$) and simplification

$$P_\theta(s) = \int \mu\left(x'\cos\theta + s\sin\theta, x'sin\theta - s\cos\theta\right)dx'\,. \tag{2.49}$$

We can see that Eq. (2.49) is equivalent to Eq. (2.46), and therefore the equality of Eq.(2.46) and Eq.(2.47) is proven. These both equations are representations of the so called Radon transform [4].

For the inversion of this transform we require the following relation (known as projection-slice theorem):

$$\mathfrak{F}^{(2)}[\mu(x,y)]\left(\vec{\xi}\right) = \mathfrak{F}^{(1)}[P_\theta(s)]\left(\xi_\theta\right)\,. \tag{2.50}$$

We use $\mathfrak{F}^{(1)}[f(x)](\xi)$ to denote a 1D Fourier transform and respectively $\mathfrak{F}^{(2)}[f(\vec{x})](\vec{\xi})$ to denote a 2D Fourier transform. Note also the equality $\vec{\xi} = \begin{pmatrix} \xi_\theta\sin\theta \\ -\xi_\theta\cos\theta \end{pmatrix}$ in Eq. (2.50).

To prove Eq . (2.50) we start with the 1D Fourier transform:

$$\mathfrak{F}^{(1)}[P_\theta(s)]\left(\xi_\theta\right) = \int e^{-2\pi is\xi_\theta}\int\int \mu(x,y)\delta(s - x\sin\theta + y\cos\theta)dxdyds\,. \tag{2.51}$$

The delta-distribution can be replaced by $\delta(x-y) = \int e^{2\pi ia(x-y)}da$. Therefore, we have

$$\mathfrak{F}^{(1)}[P_\theta(s)]\left(\xi_\theta\right) = \int e^{-2\pi is\xi_\theta}\int\int \mu(x,y)\int e^{2\pi ia(s-x\sin\theta+y\cos\theta)}dadxdyds\,. \tag{2.52}$$

This can be recast in term of a new delta distribution by performing the integration over s

$$\mathfrak{F}^{(1)}[P_\theta(s)]\left(\xi_\theta\right) = \int\int\int \mu(x,y)\delta(a-\xi_\theta)e^{2\pi i(-ax\sin\theta+ay\cos\theta)}dadxdy\,. \tag{2.53}$$

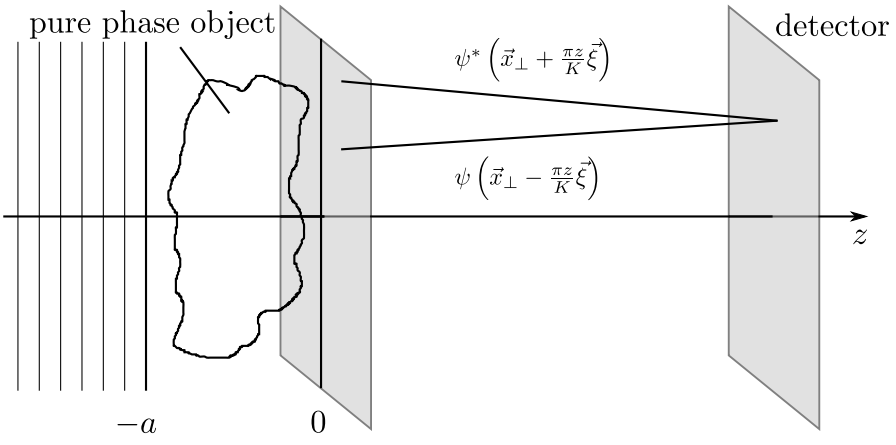

Figure 2.3.: Illustration of a setting for Guigay's relation.

Upon integrating over a and substituting $\begin{pmatrix} \xi_\theta \sin\theta \\ -\xi_\theta \cos\theta \end{pmatrix} = \begin{pmatrix} \xi_\mathrm{x} \\ \xi_\mathrm{y} \end{pmatrix} = \vec{\xi}_\perp$ we obtain

$$\mathfrak{F}^{(1)}[P_\theta(s)]\,(\xi_\theta) = \int\int \mu(x,y) \int e^{-2\pi i(x\xi_\mathrm{x}+y\xi_\mathrm{y})} dxdy = \mathfrak{F}^{(2)}[\mu(x,y)]\left(\vec{\xi}\right)\,, \tag{2.54}$$

which proves Eq.(2.50).

To carry out the reconstruction, we perform the inverse Fourier transform in polar coordinates. Here we use the fact that $P_\theta(s) = P_{\theta+\pi}(-s)$ is symmetric, so only projections with $0 \leqslant \theta \leqslant \pi$ are needed. We obtain

$$\mu(x,y) = \int_0^\pi \int_{-\infty}^\infty |\vec{\xi}| \mathfrak{F}^{(1)}[P_\theta(s)]\,(\xi_\theta)\, e^{2\pi i \xi_\theta (x\sin\theta - y\cos\theta)} ds d\theta\,. \tag{2.55}$$

This is the **F**iltered **B**ack **P**rojection (FBP) with the ramp-filter $|\vec{\xi}| \equiv |\xi_\theta|$ identified as the Jacobian of the transition to polar coordinates.
The resolution of $\mu(x,y)$ is restricted by the number of projections, this is the number of angular steps one has taken to scan the range $[0,\pi]$. We state without proof, that for a resolution of $N \times N$ pixels in the field of view a minimum of $\frac{\pi}{2}N$ projections is required.

2.2.3. Statement and proof of Guigays relation

When it comes to phase retrieval we have to face the fact that detectors only detect intensity, a direct measurement of the phase is not possible because of too rapid oscillations ($\omega \approx 10^{18}$Hz). When the wave propagates, after passing the sample, it interferes with itself, and thus the intensity contribution changes in dependence of distance to the detector. Guigay discovered in [11] an important relation between the wave field ψ_0 at the exit wave plane (after the projection towards $z = 0$) and the intensity at the detector plane (I_z)

$$\mathfrak{F}^{(2)}\left[I_\mathrm{z}\right]\left(\vec{\xi}\right) = \int \psi_0\left(\vec{x}_\perp - \frac{\pi z}{K}\vec{\xi}\right) \psi_0^*\left(\vec{x}_\perp + \frac{\pi z}{K}\vec{\xi}\right) e^{-2\pi i \vec{\xi}\vec{x}_\perp} d^2\vec{x}_\perp\,. \tag{2.56}$$

Eq. (2.56) is extremely important for our further treatment of diffraction physics. We refer to it as Guigay's relation. An illustration of a setting for this relation is given in Figure 2.3.

To prove this we start with

$$\begin{aligned}\mathfrak{F}^{(2)}\left[I_z\right]\left(\vec{\xi}\right) = \int e^{-2\pi i\xi\vec{x'}_\perp}\left(\int \bar{p}^K(z,\vec{x}'_\perp-\vec{y}_\perp)\psi_0(z=0,\vec{y}_\perp)\,d^2y_\perp\right)\times \\ \left(\int \bar{p}^{K*}(z,\vec{x}'_\perp-\vec{\omega}_\perp)\psi_0^*(z=0,\vec{\omega}_\perp)\,d^2\omega_\perp\right)d^2x'_\perp\,,\end{aligned} \tag{2.57}$$

with the Fourier transformed intensity at z as $\mathfrak{F}^{(2)}\left[I_z\right]\left(\vec{\xi}\right) = \mathfrak{F}^{(2)}\left[\psi_0(z,\vec{x}'_\perp)\psi_0^*(z,\vec{x}'_\perp)\right]\left(\vec{\xi}\right)$ and the wave function $\psi_0(z,\vec{x}'_\perp) = \bar{p}^k * \psi_0(\vec{x'}_\perp, z=0)$ propagated by the Fresnel propagator (see Eq. (3.54)).

Both propagators can be combined, and Eq. (2.57) is thus converted into

$$\begin{aligned}\mathfrak{F}^{(2)}\left[I_z\right]\left(\vec{\xi}\right) = \left(\frac{K}{-2\pi z}\right)^2\int\int\int e^{2\pi i\vec{\xi}\vec{x}'_\perp}\times \\ e^{\frac{iK}{2z}(2\vec{x}'_\perp(\vec{\omega}_\perp-\vec{y}_\perp)^2+(\vec{y}_\perp+\vec{\omega}_\perp)(\vec{y}_\perp-\vec{\omega}_\perp))}\psi_0\psi_0^*d^2y_\perp d^2\omega_\perp d^2x'_\perp\,.\end{aligned} \tag{2.58}$$

Performing the integration over $d^2x'_\perp$, we arrive at the delta-distribution[9]

$$\begin{aligned}\int e^{2\pi i\vec{x}'_\perp\left(-\vec{\xi}+\frac{K}{2\pi z}(\vec{\omega}_\perp-\vec{y}_\perp)\right)}d^2x'_\perp &= \delta^{(2)}\left(-\vec{\xi}+\frac{K}{2\pi z}(\vec{\omega}_\perp-\vec{y}_\perp)\right) \\ &= \left(\frac{K}{2\pi z}\right)^2\delta^{(2)}\left(\vec{\omega}_\perp-\vec{y}_\perp-\frac{2\pi z}{K}\vec{\xi}\right)\,.\end{aligned} \tag{2.59}$$

With this delta-distribution the integrals over $\vec{\omega}_\perp$ and $\vec{y}_\perp$ are trivial, and Eq. (2.58) becomes

$$\mathfrak{F}^{(2)}\left[I_z\right]\left(\vec{\xi}\right) = \int e^{2\pi i\vec{\xi}\left(\vec{\omega}_\perp+\frac{\pi z}{x}\vec{\xi}\right)}\psi_0\left(\vec{\omega}_\perp-\frac{2\pi z}{K}\vec{\xi}\right)\psi_0^*\left(\vec{\omega}_\perp\right)d^2\omega_\perp\,. \tag{2.60}$$

Because we are performing this integration over all $\vec{\omega}_\perp$ we can shift our integration variable as

$$\vec{\omega}_\perp \to \vec{\omega}_\perp + \frac{\pi z}{x}\vec{\xi} =: \vec{x}_\perp\,. \tag{2.61}$$

In a real experiment there is no infinite field of view. Thus we have to assure that the sample is much smaller than the field of view.

With this shift we finish the proof and obtain Eq. (2.56)

$$\mathfrak{F}^{(2)}\left[I_z\right]\left(\vec{\xi}\right) = \int \psi_0\left(\vec{x}_{\perp,-}\right)\psi_0^*\left(\vec{x}_{\perp,+}\right)e^{-2\pi i\vec{\xi}\vec{x}_\perp}d^2\vec{x}_\perp\,, \tag{2.62}$$

with the shorthand notation $\vec{x}_{\perp,\pm} = \vec{x}_\perp \pm \frac{\pi z}{K}\vec{\xi}$.

[9] The relation $\delta^{(n)}(ax) = \frac{1}{a^n}\delta^{(n)}(x)$ is used.

2.2.4. Linear model and phase retrieval

We consider pure-phase objects, so that by the projection through the sample no intensity is lost ($B(\vec{x}_\perp)) = 0$). The whole information of the projection is given by phase map $\phi(\vec{x}_\perp)$, which we would like to retrieve.
For pure-phase objects the wave function can be written as

$$\psi_0(z=0,\vec{x}_\perp) = \sqrt{I_0} e^{i\phi(\vec{x}_\perp)} \,. \tag{2.63}$$

Thus Eq. (2.62) becomes (with $\phi_\pm = \phi(\vec{x}_{\perp,\pm})$)

$$\mathfrak{F}^{(2)}\left[I_z\right]\left(\vec{\xi}\right) = \int I_0 e^{i\phi_-} e^{-i\phi_+} e^{-2\pi i \vec{\xi}\vec{x}_\perp} d^2\vec{x}_\perp \,. \tag{2.64}$$

This can not be solved analytically because in Fourier-space we encounter infinite many convolutions between ϕ_+ and ϕ_-. Before we continue, we introduce a scale factor $S \geqslant 0$ adjusting the strength of phase variations

$$e^{i\phi(\vec{x}_\perp)} \to e^{iS\phi(\vec{x}_\perp)} \,. \tag{2.65}$$

Let us first consider small S only, such that the according expansion in S can be truncated at linear order

$$e^{iS\phi_-} e^{-iS\phi_+} = 1 + S(\phi_- - \phi_+) + \mathcal{O}(S^2) \,. \tag{2.66}$$

With this linear approximation Eq. (2.62) becomes

$$\mathfrak{F}^{(2)}\left[I_z\right]\left(\vec{\xi}\right) = I_0 S \left(\delta^{(2)}\left(\vec{\xi}\right) + \int i\phi\left(\vec{x}_{\perp,-}\right) e^{-2\pi i \vec{\xi}\vec{x}_\perp} d^2x_\perp - \int i\phi\left(\vec{x}_{\perp,+}\right) e^{-2\pi i \vec{\xi}\vec{x}_\perp} d^2x_\perp \right) . \tag{2.67}$$

We define the intensity contrast at z as $g_z = \frac{I_z - I_0}{I_0}$ and, hereafter, we also define the shorthand notation

$$\begin{aligned} \mathfrak{F}g_z &:= \mathfrak{F}^{(2)}\left[g_z\right]\left(\vec{\xi}\right) \,, \\ \mathfrak{F}\phi &:= \mathfrak{F}^{(2)}\left[\phi\right]\left(\vec{\xi}\right) \,. \end{aligned} \tag{2.68}$$

In the remaining integrations the integration variables can be separated into $\vec{x}'_{\perp,\pm} = \vec{x}_\perp \pm \frac{\pi z}{K}\vec{\xi}$ for $\phi_\pm$. Eq. (2.67) becomes

$$\begin{aligned} \mathfrak{F}g_z = S \int_{-\infty}^{\infty} i\phi(\vec{x}'_{\perp,-}) e^{-2\pi i \vec{\xi}\vec{x}'_{\perp,-}} e^{-2\pi i \frac{\pi z}{K}\xi^2} d^2x'_{\perp,-} \\ - S \int_{-\infty}^{\infty} i\phi(\vec{x}'_{\perp,+}) e^{-2\pi i \vec{\xi}\vec{x}'_{\perp,+}} e^{+2\pi i \frac{\pi z}{K}\xi^2} d^2x'_{\perp,+} \,. \end{aligned} \tag{2.69}$$

Defining the dimensionless quantity $\sigma := \frac{2\pi^2 z}{K}\vec{\xi}^2$, we thus obtain

$$\mathfrak{F}g_z = S\mathfrak{F}\phi \cdot 2\sin\sigma \,, \tag{2.70}$$

or

$$S\mathfrak{F}\phi = \frac{\mathfrak{F}g_z}{2\sin\sigma} \,. \tag{2.71}$$

In Fourier space, this yields phase map in the exit-plane in term of the intensity contrast at the detector plane. Eq. (2.70) is a representation of the so called **C**ontrast **T**ransfer **F**unction (CTF) [12], [13] and solving this for $\mathfrak{F}\phi$ (Eq.(2.71)) is known as the CTF approach to phase retrieval. It is a "linear model" due to the linearisation in Eq. (2.66). This method requires $\mathfrak{F}g_z$ to be exactly zero when $\sin\sigma = 0$ otherwise poles arises in $\mathfrak{F}\phi$ and therefore artifacts in $\phi(\vec{x}_\perp)$ [14]. One possible approach to get rid of

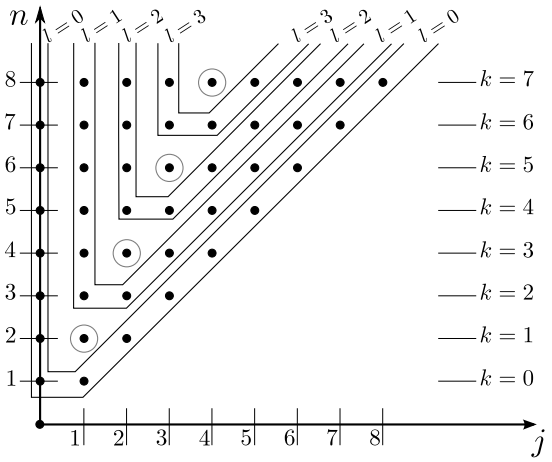

Figure 2.4.: Onion-shell expansion: n, j are the summation variables of the non linearity expansion (Eq. (2.75)) and l, k of the non locality expansion (Eq. (2.79)). Every point stands for one summand in Eq. (2.75). The points in the "shells" are summarized in $C_{\cos,l}$ and $C_{\sin,l}$, the points in the circles in $C_{\text{cen},l}$, see Eq. (2.81)

this problem is to simplify our relation even more and consider only small σ and/or small propagation distances and therefore linearize in σ. We obtain the **T**ransport of **I**ntensity **E**quation (TIE)[10] as

$$S\mathfrak{F}\phi = \frac{\mathfrak{F}g_z}{2\sigma}\,. \tag{2.72}$$

It should be mentioned that TIE approach phase retrieval is effectively a low pass filter for spatial frequencies in our phase-map, and therefore reduces the resolution when using larger propagation distances.

For further discussion of phase contrast, we will make use of the concept of a diffractogram. We define the diffractogram as the angular averaged $\mathfrak{F}g_z$ as a function of σ

$$\mathfrak{F}g_z(\sigma) = \frac{1}{2\pi}\int_0^{2\pi} \mathfrak{F}g_z\left(\vec{\xi} = \sqrt{\sigma\frac{K}{2\pi^2 z}}\begin{pmatrix}\cos\varphi\\ \sin\varphi\end{pmatrix}\right) d\varphi\,. \tag{2.73}$$

2.2.5. Non-locality expansion: Onion shells

To determine under which condition the linear model (CTF) or even the TIE approach is sufficient we need to estimate the influence of non-linear and non-local effects on diffractograms. Therefore, we will again expand ψ in powers of S, but this time we do not truncate the expansion

$$e^{iS\phi_-}e^{-iS\phi_+} = \sum_{n=0}^{\infty}\frac{(iS)^n}{n!}(\phi_- - \phi_+)^n\,. \tag{2.74}$$

Using the binomial theorem[11], we have

$$e^{iS\phi_-}e^{-iS\phi_+} = \sum_{n=0}^{\infty}\frac{(iS)^n}{n!}\sum_{j=0}^{n}\frac{(-1)^j n!}{(n-j)!j!}\phi_-^{n-j}\phi_+^j\,. \tag{2.75}$$

This is a non-linearity expansion including all powers of S. Also, we have non-local terms ($\phi_+^a\phi_-^b \mid a, b \neq 0$) in these sums, which leads to 2D convolutions[12] when performing the Fourier transform of Eq. (2.62)

[10] Other approaches to deduce TIE can be found in [15] and [16].
[11] Binomial Theorem: $(a+b)^n = \sum_{j=0}^{n}\frac{n!}{(n-j)!j!}a^{n-j}b^j$.
[12] See Fourier convolution theorem: $\mathfrak{F}[f\cdot g] = \mathfrak{F}[f] * \mathfrak{F}[g]$.

separately for ϕ_+ and ϕ_-.

We can rearrange Eq. (2.75), separating the local terms and the non-local terms. To do this we rearrange summands as illustrated in Figure 2.4, so we have a systematic expansion in powers of the bilocal product $\phi_-\phi_+$.

The summands can be sorted in three categories:

- The central term with $n = j$:

$$C_{\text{cen},l} = S^{2l}\frac{1}{(l!)^2}(\phi_-\phi_+)^l(1-\delta_{0,l})\,, \tag{2.76}$$

- the sine like term with n odd:

$$C_{\text{sin},l} = iS^{2l}(\phi_-\phi_+)^l\sum_{k=l}^{\infty}\frac{(-1)^{k+l}S^{2(k-l)+1}}{(2k+1-l)!l!}\left(\phi_-^{2(k-l)+1}-\phi_+^{2(k-l)+1}\right)\,, \tag{2.77}$$

- and the cosine like term with n even:

$$C_{\cos,l} = S^{2l}(\phi_-\phi_+)^l\sum_{k=l+1}^{\infty}\frac{(-1)^{k+l}S^{2(k-l)}}{(2k-l)!l!}\left(\phi_-^{2(k-l)}+\phi_+^{2(k-l)}\right)\,. \tag{2.78}$$

Thus, Eq. (2.75) equals

$$e^{iS\phi_-}e^{-iS\phi_+} = \sum_{l=0}^{\infty}\left(C_{\text{cen},l}+C_{\text{sin},l}+C_{\cos,l}\right)\,. \tag{2.79}$$

These parts can be Fourier transformed separately, and we can express Eq. (2.62) as

$$\mathfrak{F}g_{\text{z}} = \sum_{l=0}^{\infty}\left(\mathfrak{F}\left[C_{\text{cen},l}\right]+\mathfrak{F}\left[C_{\text{sin},l}\right]+\mathfrak{F}\left[C_{\cos,l}\right]\right) =: \sum_{l=0}^{\infty}\mathfrak{F}g_{\text{z},l} \tag{2.80}$$

with

$$\begin{aligned}
\mathfrak{F}\left[C_{\text{cen},l}\right] &= S^{2l}\frac{1}{(l!)^2}(1-\delta_{0,l})\mathfrak{F}\left[(\phi_-\phi_+)^l\right]\,,\\
\mathfrak{F}\left[C_{\text{sin},l}\right] &= 2S^{2l}\mathfrak{F}\left[(\phi_-\phi_+)^l\right] * \left(\sin\sigma\sum_{k=l}^{\infty}\frac{(-1^{k+l})S^{2(k-l)+1}}{(2k+1-l)!l!}\mathfrak{F}\left[\phi^{2(k-l)+1}\right]\right)\,,\\
\mathfrak{F}\left[C_{\cos,l}\right] &= 2S^{2l}\mathfrak{F}\left[(\phi_-\phi_+)^l\right] * \left(\cos\sigma\sum_{k=l+1}^{\infty}\frac{(-1^{k+l})S^{2(k-l)}}{(2k-l)!l!}\mathfrak{F}\left[\phi^{2(k-l)}\right]\right)\,.
\end{aligned} \tag{2.81}$$

Here $*$ denotes 2D-convolution. Because of the shape of this expansion in n, j-"space", as given in Figure 2.4, we call this expansion "onion-shell expansion" [17] and refer to $\mathfrak{F}g_{\text{z,l}}$ as the lth onion shell. In case of ϕ being a sufficiently localized function, the 0th onion shell dominates all higher shells we then obtain

$$\mathfrak{F}g_{\text{z},0} = 2\cos\sigma\sum_{k=1}^{\infty}\frac{(-1)^kS^{2k}}{(2k)!}\mathfrak{F}\left[\phi^{2k}\right]+2\sin\sigma\sum_{k=0}^{\infty}\frac{(-1)^kS^{2k+1}}{(2k+1)!}\mathfrak{F}\left[\phi^{2k+1}\right]\,. \tag{2.82}$$

This local case is relevant for a very small support in the phase-map and a large propagation distance z. Examples for this case are given in Section 3.1.2.

3. Scaling behavior of the diffractogram

In Section 2.2.4, we derived an approximation to phase retrieval, the so called "linear model". However, this method was derived under the assumption of small phase variations, which justifies a truncation of the diffractogram's expansion in powers of S at linear order. This chapter investigates effects induced by scaling the phase-map, and we perform a specialized study under which condition linear scaling can be assumed.

3.1. Single scale objects with broad spectrum (SOBS)

To systematically study the influence of non-linear and non-local contributions to the diffractogram we start with very simple phase maps. We will use "single scale objects with a broad spectrum (SOBS)" as phase maps, which are isotropic (rotationally invariant) and contain only one spacial degree of freedom (scale). Examples of SOBS are the circular disk (with the radius as scale) or the 2D-Gaussian, which we will mainly use.
All numerical evaluations in this Chapter suffers an insignificant uncertainty, whose extend is estimated in the Appendix A.1.

3.1.1. Onion shell expansion for Gaussian phase-map

To discuss the case of a 2D-Gaussian we can perform, the full onion-shell expansion as derived in Section 2.2.5. The phase-map is defined to be

$$\phi(\vec{x}_\perp) = Se^{-\frac{\vec{x}_\perp^2}{2\omega}} . \tag{3.1}$$

Where $0 \leq S$ is a scaling factor do determine the strength of phase variation.
The onion-shell expansion for this phase-map is performed by inserting ϕ into Eq. (2.76), Eq. (2.77) and Eq. (2.78), and executing the 2D-Fourier transform:

$$\begin{aligned}
\mathfrak{F}\left[C_{\mathrm{cen},l}\right] &= \frac{1}{(l!)^2}\frac{\omega\pi}{l}S^{2l}e^{-\frac{\pi\lambda z l}{2\omega}\vec{\xi}^2}e^{-\frac{\pi^2\omega}{l}\vec{\xi}^2}\left(1-\delta_{l,0}\right) , \\
\mathfrak{F}\left[C_{\mathrm{sin},l}\right] &= \frac{4\pi\omega}{2k+1}\sum_{k=l}^{\infty}\frac{(-1)^{k+l}}{(2k+1-l)!l!}S^{2k+1}e^{-\frac{\lambda^2 z^2(4kl+2l-2l^2)}{4\omega(2k+1)}\vec{\xi}^2}e^{-\frac{2\pi^2\omega}{2k+1}\vec{\xi}^2}\sin\left(\frac{\pi\lambda z\omega(2k-2l+1)}{2k+1}\vec{\xi}^2\right) , \\
\mathfrak{F}\left[C_{\cos,l}\right] &= \frac{4\pi\omega}{2k}\sum_{k=l+1}^{\infty}\frac{(-1)^{k+l}}{(2k-l)!l!}S^{2k}e^{-\frac{\lambda^2 z^2(2kl-l^2)}{4\omega k}\vec{\xi}^2}e^{-\frac{-\pi^2\omega}{k}\vec{\xi}^2}\cos\left(\frac{\pi\lambda z(k-l)}{k}\vec{\xi}^2\right) .
\end{aligned} \tag{3.2}$$

A dimensionless representation can be obtained by appealing to $\sigma = \pi\lambda z\vec{\xi}^2$ (as already introduced in Section 2.2.4) and introducing the Fresnel number as $F_\omega = \frac{\omega}{\lambda z}$. Upon performing these substitutions, Eq. (3.2) becomes

$$\begin{aligned}
\mathfrak{F}\left[C_{\mathrm{cen},l}\right] &= \frac{1}{(l)^2}\frac{\pi\omega}{l}S^{2l}e^{-\sigma\left(\frac{l}{2\omega}+\frac{\pi F_\omega}{l}\right)}\left(1-\delta_{l,0}\right)\,, \\
\mathfrak{F}\left[C_{\mathrm{sin},l}\right] &= \sum_{k=l}^{\infty}\frac{4\pi\omega}{2k+1}\frac{(-1)^{l+k}}{(2k-l+1)!l!}S^{2k+1}e^{-\sigma\left(\frac{2\pi F_\omega}{2k+1}+\frac{2kl-l^2+l}{2\pi F_\omega(2k+1)}\right)}\sin\left(\frac{2k-2l+1}{2k+1}\sigma\right), \\
\mathfrak{F}\left[C_{\mathrm{cos},l}\right] &= \sum_{k=l+1}^{\infty}\frac{4\pi\omega}{2k}\frac{(-1)^{l+k}}{(2k-l)!l!}S^{2k}e^{-\sigma\left(\frac{\pi F_\omega}{k}+\frac{2kl-l^2}{4\pi F_\omega k}\right)}\cos\left(\frac{k-l}{k}\sigma\right).
\end{aligned} \tag{3.3}$$

Although, this is an exact expansion it contains infinite series in powers of S for each onion-shell, which need to be truncated in numerical evaluations. To get stable results within each onion-shell one can consider the case $F_\omega = 0$ where the summation can be performed exactly. For finite F_ω correction terms can be included. Exemplary, this is done for the zeroth onion shell ($l = 0$). The following relations are used

$$\begin{aligned}
\sum_{k=k}^{\infty}\frac{S^{2k+1}(-1)^k}{2k+1} &= \int_0^S\frac{\sin t}{t}dt =: SI(S)\,, \\
\sum_{k=1}^{\infty}\frac{S^{2k}(-1)^k}{2k(2k)!} &= \int_0^S\frac{\cos t-1}{t}dt =: CI(S)\,.
\end{aligned} \tag{3.4}$$

We call SI the sine integral and CI the cosine integral[1]. With these relations the zeroth onion shell can be approximated as

$$\begin{aligned}
\frac{\mathfrak{F}\left[C_{l=0}\right]}{4\pi\omega} \approx \sin\sigma &\left(SI(S)+\sum_{k=0}^{c}\frac{S^{2k+1}}{2k+1}\frac{(-1)^k\left(e^{-\sigma\frac{2\pi F_\omega}{2k+1}}-1\right)}{(2k+1)!}\right) \\
&+\cos\sigma\left(CI(S)+\sum_{k=1}^{c}\frac{S^{2k}}{2k}\frac{(-1)^k\left(e^{-\sigma\frac{2\pi F_\omega}{2k}}-1\right)}{(2k)!}\right).
\end{aligned} \tag{3.5}$$

The integer c determines the precision. This and the expressions for the first nine onion-shells of a Gaussian phase-map have already been published in [19]. An example diffractogram is given in Fig. 3.1. This example motivates the importance to have a closer look at the scaling behavior, because the assumed scaling linearity in the linear model is definitely not strictly valid. Clear indications are the different positions of the zero points for different S. A more detailed representation of Gaussian SOBS scaling behavior is given in Section 3.1.4.

In case of locality, valid for negligible bilocality, the zeroth onion-shell is a good approximation. To specify this case, we demand that $\frac{\phi_-\phi_+}{S^2} \ll e^{-2}$, and obtain the condition

$$8F_\omega \ll \frac{\sigma}{\pi}\,. \tag{3.6}$$

A second condition for good locality is, that in Eq. (3.5) the absolute value of the exponent for $k = 0$ is much smaller than unity[17]. Both conditions combined state

$$8F_\omega \ll \frac{\sigma}{\pi} \ll \frac{1}{2\pi^2F_\omega}\,. \tag{3.7}$$

[1]Notice that in the literature, the cosine integral is defined slightly differently, see [18] p.54.

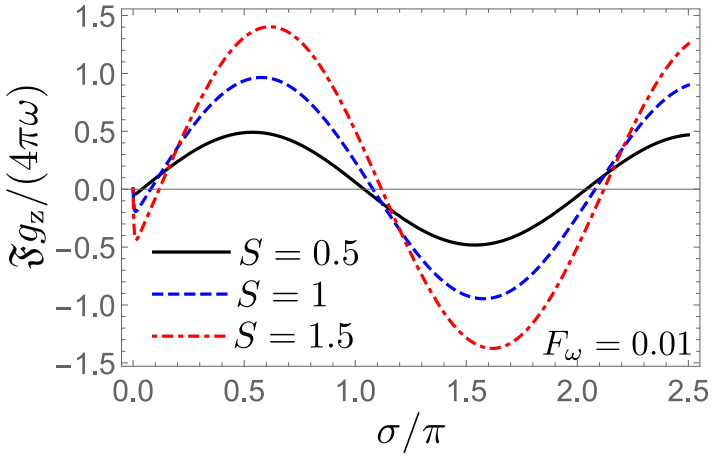

Figure 3.1.: Diffractograms for phase-map $\phi(\vec{x}_\perp) = Se^{-\frac{\vec{x}_\perp^2}{2\omega}}$ with $F_\omega = 0.01$ and scaling factors $S = \{0.5, 1, 1.5\}$. Note the shift of the zeros in dependence of S.

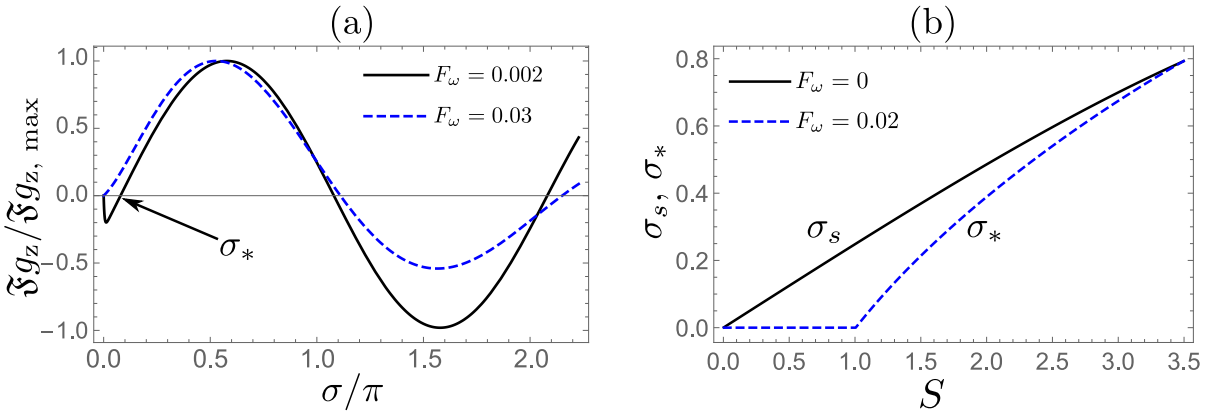

Figure 3.2.: Low frequency region of normalized diffractogram $\mathfrak{F}g_z$ of a Gaussian phase-map. (a): $\mathfrak{F}g_z$ for $F_\omega = 0.001$ (solid, overcritical) and $F_\omega = 0.03$ (dashed, subcritical) at $S = 1$. Note the additional zero σ_* in the overcritical case. (b): S dependence of $\sigma_s = \sigma_*(S)$ at $F\omega = 0$ (solid) and $\sigma_*(S)$ at $F\omega = 0.02$ (dashed).

Therefore, in far-field limit $F_\omega \to 0$ the zeroth onion-shell becomes exact for all $\sigma > 0$. The case $\sigma = 0$ violates the condition in Eq. (3.6) and therefore can not be represented by the zeroth onion shell. However, we know that $\mathfrak{F}g_z(\sigma = 0) = 0$ is valid for all phase-maps, because of energy conservation in free space propagation.

For the far-field limit $F_\omega \to 0$, the zeroth onion-shell is exact for $\sigma > 0$ and reads

$$\begin{aligned} \lim_{F_\omega \to 0} \frac{\mathfrak{F}g_{z,0}(\sigma, F_\omega)}{4\pi\omega} &= \sin(\sigma) SI(S) + \cos(\sigma) CI(S) \\ &= \sqrt{SI^2(S) + CI^2(S)} \sin(\sigma - \sigma_s), \end{aligned} \tag{3.8}$$

where

$$\sigma_s = \left| \arctan\left(\frac{CI(S)}{SI(S)} \right) \right|. \tag{3.9}$$

This σ_s is an additional zero in comparison to the linear model. An additional zero σ_* also exists for small F_ω (see Fig. 3.2 (a)) exhibiting critical behavior for increasing S and/or decreasing F_ω: Whether this zero exists depends on whether the point (S, F_ω) is left (subcritical) or right (overcritical) to the line

$$F_\omega = \frac{S}{16\pi} \tag{3.10}$$

in the $S - F_\omega$ plane [17], see Fig. 3.2 (a), 3.2 (b). A more detailed discussion about this additional zero can be found in [17] and [19].

3.1.2. The extreme far field

The fact that the zeroth onion-shell is exact in the extreme far-field limit ($F_\omega = \frac{\omega}{\lambda z} \to 0$) for $\sigma > 0$ motivates the search for universal aspects of the diffractogram in this regime[2]. In particular, we consider the normalized diffractograms induced by the following three SOBS phase-maps.

Gaussian phase-map

$$\phi(\vec{x}_\perp) = Se^{-\frac{\vec{x}_\perp^2}{2\omega}}\,, \tag{3.11}$$

circular disk phase-map[3]

$$\phi(\vec{x}_\perp) = S\Theta(\sqrt{\omega} - |\vec{x}_\perp|)\,, \tag{3.12}$$

exponential phase-map

$$\phi(\vec{x}_\perp) = Se^{-\frac{|\vec{x}_\perp|}{\sqrt{\omega}}}\,. \tag{3.13}$$

Let us discuss each of this cases.

Gaussian phase-map
The zeroth onion-shell was derived in Eq. (3.3) ($l = 0$), so we can directly perform the limit $F_\omega \to 0$ as

$$\begin{aligned}\lim_{F_\omega\to 0}\frac{\mathfrak{F}g_{\mathrm{z},0}}{4\pi\omega} &= \lim_{F_\omega\to 0}\left(\sin(\sigma)\sum_{k=0}^{\infty}\frac{S^{2k+1}}{2k+1}\frac{(-1)^k e^{-\sigma\frac{2\pi F_\omega}{2k+1}}}{(2k+1)!} + \cos(\sigma)\sum_{k=1}^{\infty}\frac{S^{2k}}{2k}\frac{(-1)^k e^{-\sigma\frac{2\pi F_\omega}{2k}}}{(2k)!}\right)\\ &= \sin(\sigma)\sum_{k=0}^{\infty}\frac{S^{2k+1}}{2k+1}\frac{(-1)^k}{(2k+1)!} + \cos(\sigma)\sum_{k=1}^{\infty}\frac{S^{2k}}{2k}\frac{(-1)^k}{(2k)!}\,.\end{aligned} \tag{3.14}$$

Circular disk phase-map
We obtain the zeroth onion-shell by substituting Eq. (3.12) into Eq. (2.82). The result is

$$\begin{aligned}\mathfrak{F}g_{\mathrm{z},0} = {}& 2\sin(\sigma)\sum_{k=0}^{\infty}\frac{(-1)^k}{(2k+1)!}S^{2k+1}\mathfrak{F}\left[\Theta^{2k+1}\left(\sqrt{\omega} - |\vec{x}_\perp|\right)\right] +\\ & 2\cos(\sigma)\sum_{k=1}^{\infty}\frac{(-1)^k}{(2k)!}S^{2k}\mathfrak{F}\left[\Theta^{2k}\left(\sqrt{\omega} - |\vec{x}_\perp|\right)\right]\,.\end{aligned} \tag{3.15}$$

With the identity $\Theta^n(x) = \Theta(x)$ for $n \neq 0$ and the 2D-Fourier transform of the disc, we have

$$\mathfrak{F}^{(2)}\left[\Theta\left(\sqrt{\omega} - |\vec{x}_\perp|\right)\right](\vec{\xi}) = 2\pi\omega\frac{J_1(2\pi\sqrt{\omega}|\vec{\xi}|)}{2\pi|\vec{\xi}|}\,. \tag{3.16}$$

Here the Bessel function of the first kind J_1 occurs. It is defined by the series

$$J_1(x) := \sum_{m=0}^{\infty}\frac{(-1)^m}{m!(m+1)!}\left(\frac{x}{2}\right)^{2m+1}\,. \tag{3.17}$$

Now we can execute the far-field limit as

[2]The content of this section has already been elaborated and published by Yannick Müller in [19].

$$\begin{aligned}\lim_{F_\omega\to 0}\frac{\mathfrak{F}g_{\mathrm{z},0}}{4\pi\omega} &= \lim_{F_\omega\to 0}\left(\sin(\sigma)\sin(S)+\cos(\sigma)\left(\cos(S)-1\right)\right)\frac{J_1(2\sqrt{\sigma F_\omega})}{2\sqrt{\sigma F_\omega}}\\ &= \frac{1}{2}\left(\sin(\sigma)\sin(S)+\cos(\sigma)\left(\cos(S)-1\right)\right)\,.\end{aligned} \tag{3.18}$$

Exponential phase-map

The zeroth onion-shell, after substituting Eq. (3.13) into Eq. (2.82) and performing the 2D-Fourier transform, reads

$$\begin{aligned}\frac{\mathfrak{F}g_{\mathrm{z},0}}{4\pi\omega} = \sin(\sigma)\sum_{k=1}^{\infty}\frac{(-1)^k}{(2k+1)!}\frac{(2k+1)S^{2k+1}}{\left((2k+1)^2+4\pi^2\vec{\xi}^2\omega\right)^{3/2}}+\\ \cos(\sigma)\sum_{k=0}^{\infty}\frac{(-1)^k}{(2k)!}\frac{(2k)S^{2k}}{\left((2k)^2+4\pi^2\vec{\xi}^2\omega\right)^{3/2}}\,.\end{aligned} \tag{3.19}$$

Doing the far-field limit, we obtain

$$\begin{aligned}\lim_{F_\omega\to 0}\frac{\mathfrak{F}g_{\mathrm{z},0}}{4\pi\omega} &= \lim_{F_\omega\to 0}\left(\sin(\sigma)\sum_{k=0}^{\infty}\frac{(-1)^k S^{2k+1}(2k+1)}{(2k+1)!\left((2k+1)^2+4\pi\sigma F_\omega\right)^{3/2}}+\cos(\sigma)\sum_{k=1}^{\infty}\frac{(-1)^k S^{2k}(2k)}{(2k)!\left(4k^2+4\pi\sigma F_\omega\right)^{3/2}}\right)\\ &= \sin(\sigma)\sum_{k=0}^{\infty}\frac{(-1)^k S^{2k+1}}{(2k+1)!(2k+1)^2}+\cos(\sigma)\sum_{k=1}^{\infty}\frac{(-1)^k S^{2k}}{(2k)!(2k)^2}\,.\end{aligned} \tag{3.20}$$

The extreme far-field limit is equivalent to the case of extremely small objects $\omega\to 0$. But objects with no extent obviously can not induce phase contrast. Therefore, we need to enforce non-trivial phase contrast by introducing a normalization N_ω such that

$$\lim_{\omega\to 0}N_\omega^{-1}\phi(\vec{x}_\perp)|_{S=1}=\delta^{(2)}(\vec{x}_\perp)\,. \tag{3.21}$$

For our three phase maps we obtain

$$N_\omega=\begin{cases}2\pi\omega & \text{for Gaussian phase-map,}\\ \pi\omega & \text{for circular disc phase-map,}\\ 2\pi\omega & \text{for exponential phase-map.}\end{cases} \tag{3.22}$$

In general a normalized diffractogram (for $\sigma>0$) in the extreme far-field limit can be defined as

$$\begin{aligned}\lim_{F_\omega\to 0}\frac{\mathfrak{F}g_{\mathrm{z}}}{N_\omega} &= 2\sin(\sigma)\sum_{k=0}^{\infty}\frac{(-1)^k}{(2k+1)!}S^{2k+1}C(2k+1)+2\cos(\sigma)\sum_{k=1}^{\infty}\frac{(-1)^k}{(2k)!}S^{2k}C(2k)\\ &=: S_s(S)\sin(\sigma)+S_c\cos(\sigma)\,.\end{aligned} \tag{3.23}$$

The coefficient $C(j)$ can be read of from the last line in Eq. (3.14), Eq. (3.18) and Eq. (3.20) as

$$C(j)=\begin{cases}j^{-1} & \text{for Gaussian phase-map,}\\ 1 & \text{for circular disc phase-map,}\\ j^{-2} & \text{for exponential phase-map.}\end{cases} \tag{3.24}$$

Thus, we may state that the phase-shape information, which is different for each of these three phase maps, transmutes into information residing in the scaling functions $S_s(S)$ and $S_c(S)$ of Eq. (3.23) in terms of the coefficients $C(j)$. Except for this S-scaling the diffractogram is σ-universal in the extreme far-field.

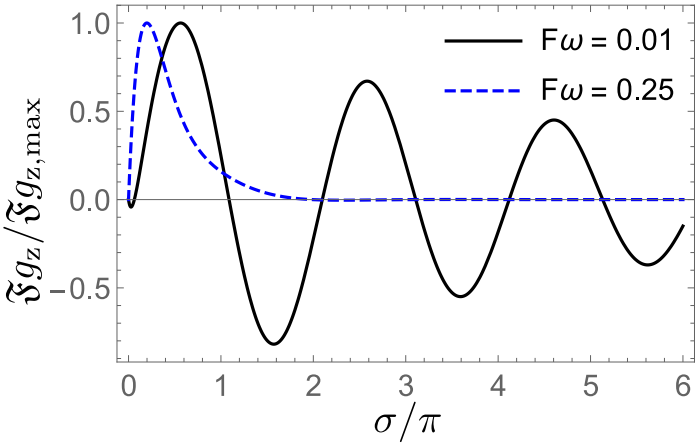

Figure 3.3.: Diffractogram of Gaussian phase-map at $S = 1$ and $F_\omega = 0.01$ (oscillatory), $F_\omega = 0.25$ (overdamped non-oscillatory).

3.1.3. From oscillatory to damped diffractogams

For small F_ω the diffractogram has an oscillatory form while for larger F_ω it becomes overdamped and non-oscillatory, see Figure 3.3. Motivated by this, we take a closer look at the transition between these two regimes. A measure for the strength of oscillatory behavior needs to be defined. To do this, we take a look at the 1D-Fourier transform of the diffractogram

$$\widetilde{\mathfrak{F}g_z}(k, F_\omega) = \int e^{-2\pi\sigma k} \mathfrak{F}g_z(\sigma, F_\omega) d\sigma \,. \tag{3.25}$$

This is plotted for different values of F_ω and $S = 1$ in Figure 3.4 (a).

Inspecting the positive branch $k \geqslant 0$, the (pseudo) frequency $k_{\max}$ at the maximum of $\widetilde{\mathfrak{F}g_z}(k, F_\omega)$ determines the dominant oscillation frequency (inverse of twice the distance between adjacent zero crossings in $\mathfrak{F}g_z(\sigma, F_\omega)$). During the transition to the damped regime, by increasing F_ω, the curve $\widetilde{\mathfrak{F}g_z}(k)$ becomes wider, and the maximum moves to lower k-values. Therefore, we use

$$\frac{k_{\max}(F_\omega)}{k_{\max}(F_\omega = 0)} \,, \tag{3.26}$$

as measure of the strength of oscillatory behavior.

In Figure 3.4 (b) $\frac{k_{\max}(F_\omega)}{k_{\max}(F_\omega=0)}$ is plotted in dependence of F_ω. We can see that $k_{\max}(F_\omega)$ behaves like an order parameter of a second order phase transition with the critical drop at $F_\omega = 0.12$ exhibiting a critical exponent $\nu = 0.37$ for $S = 1$. This behavior also is seen at other values of S, see Table 3.1. We can see that this transition depends on S. Larger values of S imply transitions at smaller F_ω.
Motivated by this S-dependency we use $k_{\max}$ as a function of S at a fixed F_ω. In Figure 3.5 (a) $\frac{k_{\max,F_\omega=0.12}(S)}{k_{\max,F_\omega=0.12}(S=0.005)}$ is plotted and we see a shape similarly to the shape in Figure 3.4 (b) with a critical drop at $S = 1$. In Figure 3.5 (b) some positions of the critical drop in the F_ω-S-plane are plotted to illustrate their dependency.

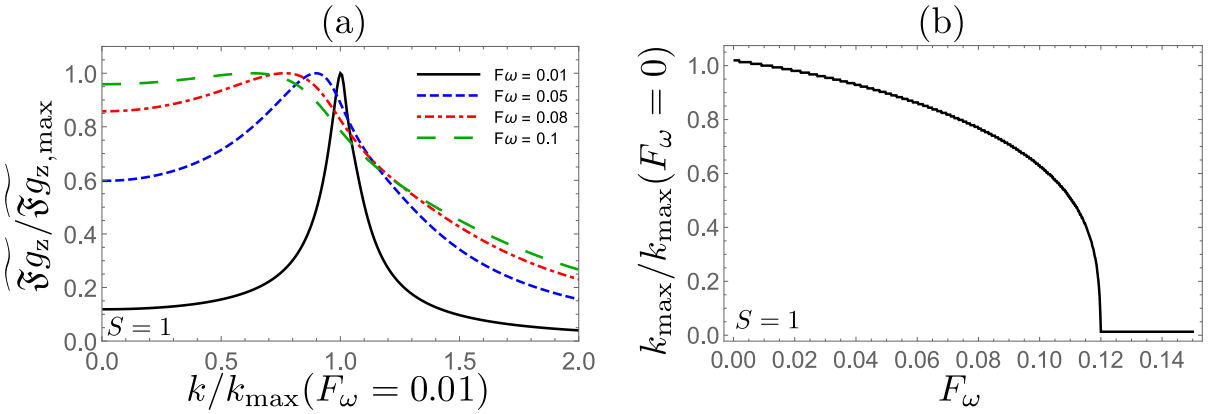

Figure 3.4.: Oscillatory behavior of diffractograms described by Fourier analysis as a function of F_ω. (a): Positive k-branch of 1D Fourier transformed diffractogram, see Eq. (3.25). (b): Normalized $k_{\max}(F_\omega, S = 1)$. Note the critical drop at $F_\omega(S = 1) = 0.12$ which is associated with a critical exponent of $\nu(S = 1) = 0.37$.

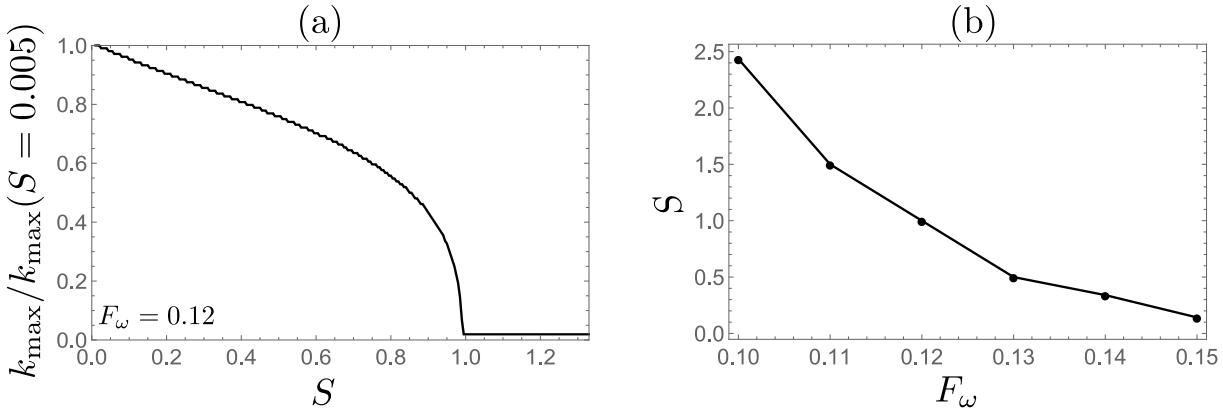

Figure 3.5.: Oscillatory behavior of diffractograms described by Fourier analysis as a function of S. (a): Normalized $k_{\max}(S, F_\omega = 0.12)$. Note the critical drop at $S(F_\omega = 0.12) = 1$. (b): Positions of the critical drop of $k_{\max}$ in the F_ω-S-plane.

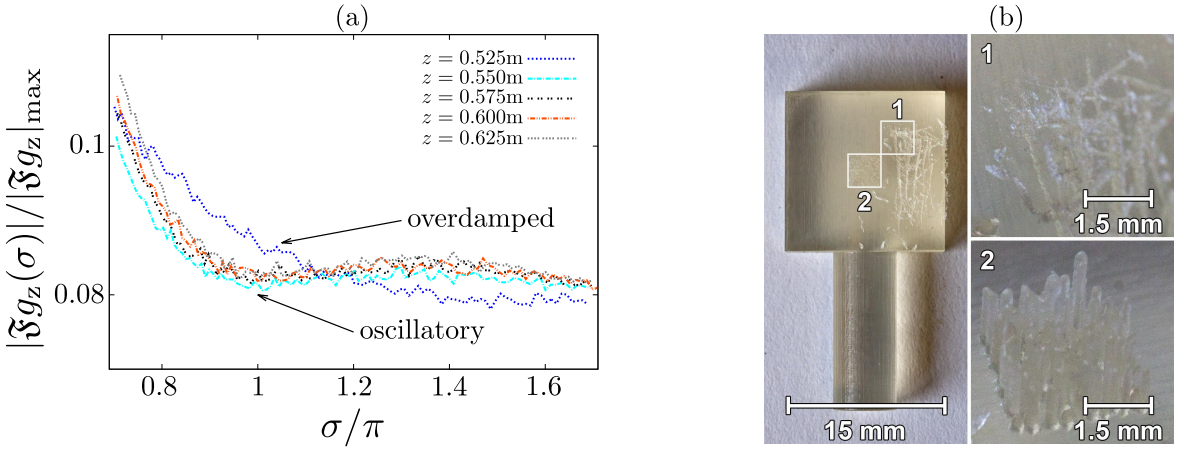

Figure 3.6.: (a): ESRF experiment with $E = 17.5$keV, $\Delta E/E = 0.03$, effective pixel size $\Delta x = 1.6\mu$m at various propagation distances z. The sample (see (b)) creates weak phase variation (scratched). Note the overdamped behavior at $z = 0.525$m and the (damped) oscillatory behavior for $z \geq 0.55$m. For more details about this experiment and the samples used see [17]. (b): 3D printed sample including holding shaft (left) and magnified scratched (1) and Manhattan (2) region.

Table 3.1.: Critical F_ω and exponents for the transition of oscillatory to over-damped non-oscillatory behavior of SOBS-diffractograms at different scaling factors S.

scaling factor S	critical F_ω	critical exponent ν
0.5	0.13	0.51
1.0	0.12	0.37
1.5	0.11	0.27

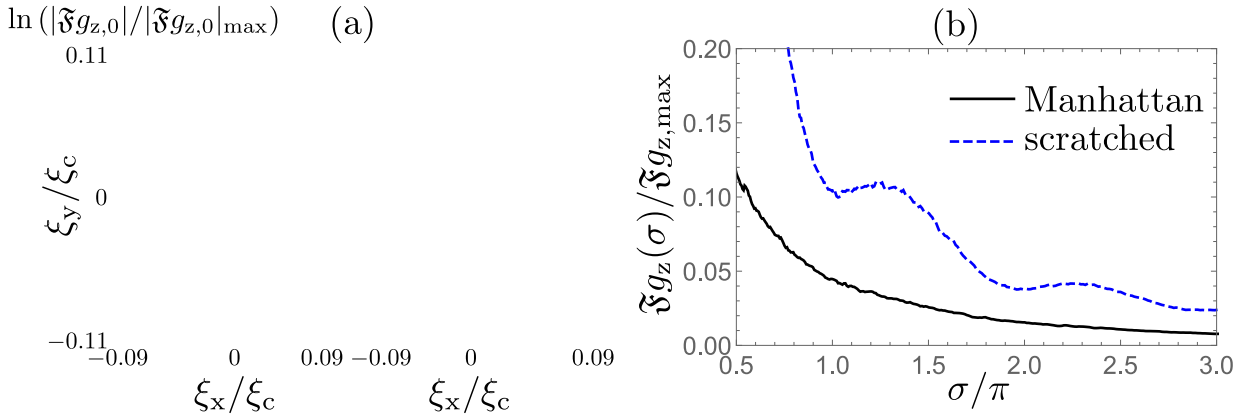

Figure 3.7.: ESRF experiment with $E = 17.5$keV, $\Delta E/E = 0.03$, effective pixel size $\Delta x = 1.6\mu$m and propagation distance $z = 3.6$m. The sample consists of two regions creating weak (scratched) and strong (Manhattan) phase variation. (a) $\ln(1 + |\mathfrak{F}g_z|/|\mathfrak{F}g_{z,\max}|)$ for the scratched and the Manhattan sample. (b) diffractogram (angular averaged, see Eq.(2.73)) $\mathfrak{F}g_z(\sigma)$. Note the over damped case (Manhattan, solid) in comparison to the oscillating case (scratched, dashed). For more details see [17].

The transition between oscillatory and damped behavior can be observed in experiments by changing the propagation distance. This has been done for an multi-scale object with weak phase variation (scratched) at the European Synchrotron Radiation Facility (ESRF) ([17], Fig. 3). We can see in Figure 3.6 an overdamped case at small propagation distance ($z = 0.525$m) and an still damped but clearly oscillatory behavior at larger z.

Also this scaling dependent effect was observed in this experiment ([17], Fig. 3), here with an additional object creating larger phase variations. The diffractogram of two pure-phase objects, one with a weak phase variation (scratched) according to a small S and one with strong phase variation (Manhattan) according to a larger S, have been measured, see Figure 3.7. The object with smaller phase variation (scratched) according to small S has a slight oscillatory behavior, while these oscillations can not be observed in the case of larger phase variation. But we need to be cautious here because we do not have real scaling, because two completely different phase-maps were used.

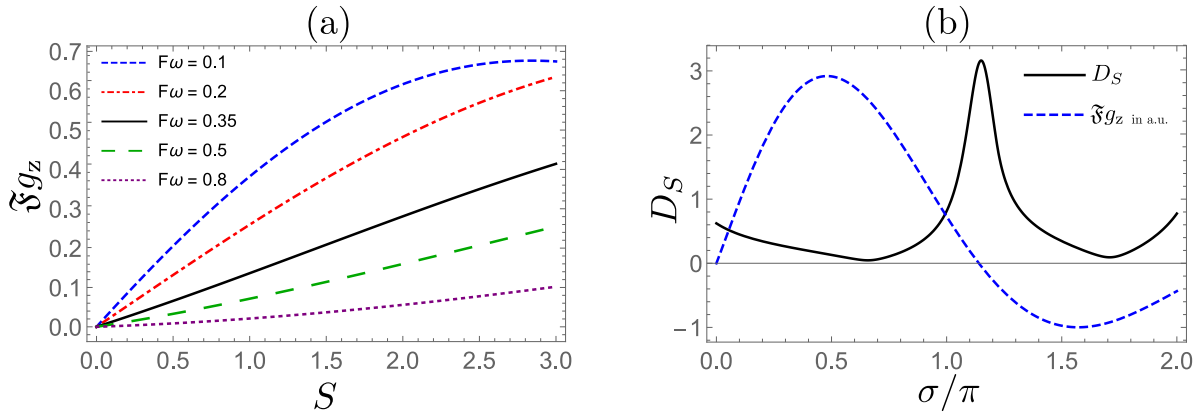

Figure 3.8.: Examples for S-scaling linearity for Gaussian phase-map. (a): $\mathfrak{F}g_z(S)$ at $\sigma = 0.25\pi$ for various F_ω. Note the transition between convex and concave S-scaling at $F_\omega = 0.35$. (b): Scaling linearity D_S plotted over σ, for $F_\omega = 0.05$, $S_1 = 0.001$, $S_2 = 1.5$. Also $\mathfrak{F}g_z(S = 1)$ in arbitrary units, note the maximum of D_S around the zero of $\mathfrak{F}g_z$.

3.1.4. Scaling linearity

The scaling dependent effects of Section 3.1.1 (for example the additional zero) and 3.1.3 indicate that the linear approximation in Section 2.2.4, Eq. (2.70) enjoys limited applicability only. However, this linear model is important for phase retrieval. Therefore, this motivates to have a closer look where and how strong non-linear effects appear. In Figure 3.8 (a) $\mathfrak{F}g_z(S)$ is plotted for a constant value of $\sigma/\pi = 0.25$ and various values of F_ω. The curve has a convex shape for small F_ω and transmutes into a concave shape for large F_ω. At $F_\omega = 0.35$ the curve is nearly a straight line, and therefore represents linear scaling behavior.
To analyse scaling behavior in the general case, we require an according measure. Therefore, the standard deviation of the functions first derivative has been chosen. Consider a diffractogram $\mathfrak{F}g_z(\sigma, F_\omega, S)$ with small derivations in S. In the linear case the first derivative $\frac{d}{dS}\mathfrak{F}g_z(\sigma, F_\omega, S)$ is constant. The less linear the function is the more the first derivative varies. We introduce the standard deviation of the first derivative between S_1 and S_2, and we subsequently normalize it to the mean value of the diffractogram

$$D_S\,(S_1, S_2, \sigma, F_\omega) = \frac{\sqrt{\int_{S_1}^{S_2} \left| \frac{\mathfrak{F}g_z(\sigma,F_\omega,S_2) - \mathfrak{F}g_z(\sigma,F_\omega,S_1)}{S_2 - S_1} - \frac{d}{dS}\mathfrak{F}g_z(\sigma, F_\omega, S) \right|^2 dS}}{\int_{S_1}^{S_2} |\mathfrak{F}g_z(\sigma, F_\omega, S)|\, dS} . \tag{3.27}$$

The smaller D_S the more linear $\mathfrak{F}g_z$ behaves in S. In Figure 3.8 (b) D_S and $\mathfrak{F}g_z(\sigma, S = 1)$ are plotted as a function of σ. We recognize that the maximal non-linearity accrues within a region centered around the zeros of $\mathfrak{F}g_z$. Recall that these zeros are shifted under changes of S, see Figure 3.1.

In the next step, we have a look at the scaling linearity in the low frequency regime $\sigma < \pi/2$ for $0 < F_\omega < 1$. In Figure 3.9 (a) D_S is plotted against the $F_\omega - \sigma$-plane, and a nearly linear region becomes visible. The minimum σ of D_S, is plotted in Figure 3.9 (b) and can be fitted to the following model

$$\sigma_{\mathrm{ml}}(A, B, F_\omega) = A F_\omega^B . \tag{3.28}$$

Figure 3.9 implies a satisfactory coincidence between $\sigma(F_\omega)$ and the best-fit model of Eq. (3.28) with $A = 0.064$ and $B = -1.04$. It should be mentioned that A and B depends on S_2. The extracted values for A and B for various S_2 can be found in Table 3.2. For a certain scaling window, bounded by $S_1 = 0$ and $S_2 \approx 1.4$, we can exploit that $\sigma = \frac{\pi\omega}{F_\omega}\xi^2$. Setting $B = -1$, we infer the physical frequency modulus

$$\xi_{\mathrm{ml}} = \left|\vec{\xi}_{\mathrm{ml}}\right| , \tag{3.29}$$

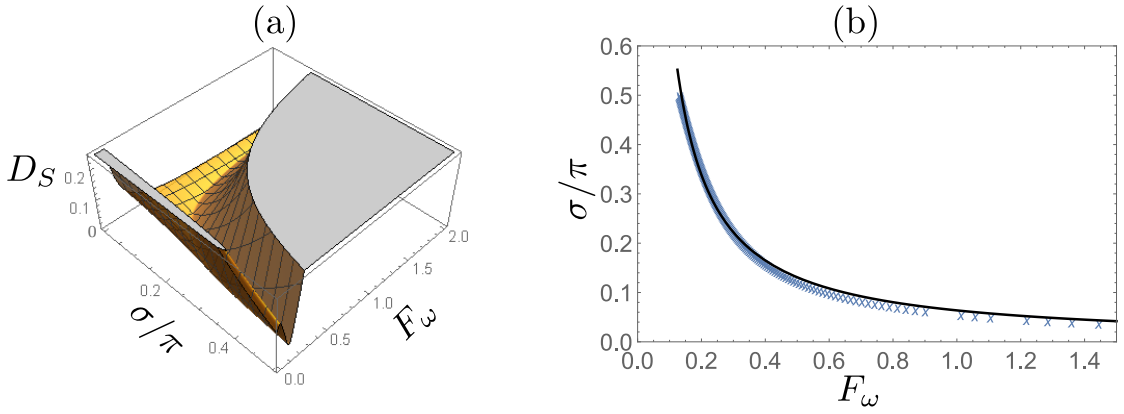

Figure 3.9.: D_S for low frequencies σ. The function, as defined in Eq.(3.27), is evaluated for a scaling window $[S_1 = 0.001, S_2 = 1.5]$. (a): D_S plotted as a function of F_ω and σ. (b): Minima of D_S (crosses) and best-fit model Eq. (3.28) (solid line) for $A = 0.064$ and $B = -1.04$.

where maximal S-scaling linearity occurs, is independent of F_ω. Namely,

$$\xi_{\mathrm{ml}} = \sqrt{\frac{A}{\pi\omega}} \approx (0.143 \pm 0.001)\sqrt{\omega}^{-1}\,. \tag{3.30}$$

For scaling window$[S_1 = 0, S_2 = 1.4]$ Eq. (3.30) states, that nearly independently of the propagation "distance" λz, there exists a single physical frequency modulus ξ_{ml} at which the diffractogram scales in a maximally linear way with S.

Table 3.2.: Fit parameter for Eq. (3.28) at scaling window $[S_1 = 0, S_2]$ (for estimation of scaling linearity, see Eq. (3.27)).

S_2	A	B
1.7	$(6.20 \pm 0.06) \cdot 10^{-2}$	-1.091 ± 0.006
1.6	$(6.30 \pm 0.07) \cdot 10^{-2}$	-1.064 ± 0.007
1.5	$(6.37 \pm 0.07) \cdot 10^{-2}$	-1.037 ± 0.008
1.4	$(6.44 \pm 0.08) \cdot 10^{-2}$	-1.011 ± 0.007
1.35	$(6.48 \pm 0.08) \cdot 10^{-2}$	-0.997 ± 0.007
1.3	$(6.53 \pm 0.08) \cdot 10^{-2}$	-0.983 ± 0.007
1.25	$(6.55 \pm 0.09) \cdot 10^{-2}$	-0.970 ± 0.008
1	$(6.81 \pm 0.10) \cdot 10^{-2}$	-0.900 ± 0.008
0.5	$(6.26 \pm 0.08) \cdot 10^{-2}$	-0.869 ± 0.007

Let us have a look at the scaling behavior for higher σ in the (damped) oscillatory case. Due to the shifting zeros under scaling there are maxima in $D_S(\sigma)$, as already mentioned. Between this maxima are areas (σ-bands) with a more linear scaling behavior, we will refer to them as D_S-bands (D_B), where $D_S < D_{\mathbf{thr}}$. For our further discussion we choose, as $D_{\mathbf{thr}}$, the arbitrary value $D_{\mathbf{thr}} = 0.25$. In Figure 3.10 are examples of $\mathfrak{F}g_z(S)$ with σ and F_ω chosen the way that $D_S = 0.25$ and we see that the curves are not really straight lines, but the curvature is still small.

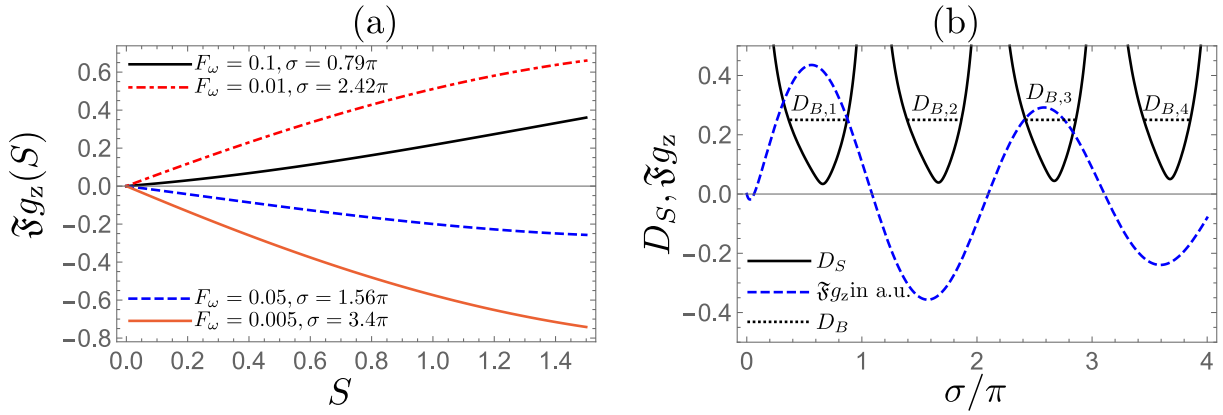

Figure 3.10.: Example of D-bands, where $D_S < 0.25$. (a) Examples of $\mathfrak{F}g_z(S)$, where $D_S = 0.25$, ensured by the choice of σ and F_ω. (b) $\mathfrak{F}g_z(\sigma)$ in arbitrary units with $F_\omega = 0.01$ and corresponding D_S with $S_1 = 0, S_2 = 1.5$, note the D-bands $D_{B,n}\,|n = 1, 2, 3, 4$, where $D_S \leqslant 0.25$.

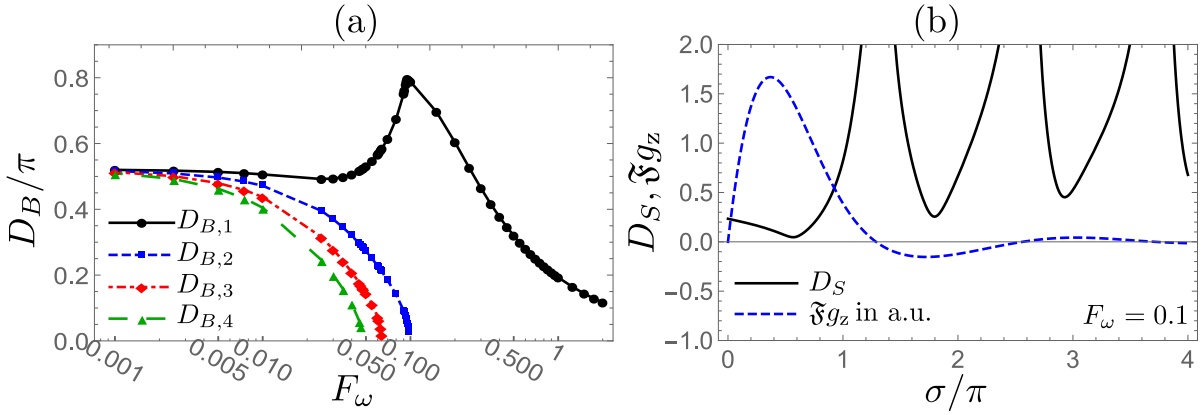

Figure 3.11.: (a)First four D-bands $D_{B,1}, D_{B,2}, D_{B,3}, D_{B,4}$ at various F_ω (connected for better visibility). Note the convergence for small F_ω to the value $D_{B,n} = 0.521\pi$ for $F_\omega = 0$. (b) $D_S(S)$ and $\mathfrak{F}g_z(\sigma)$ in arbitrary units at $F_\omega = 0.1$, note the damped behavior and the enlarged $D_{B,1}$ (see (a)) due to the lack of the additional zero even at large S. The length of $D_{B,1}$ reaches its maximum around the F_ω value of the oscillatory-to-overdamped transition.

These $D_{B,n}$ for the first four bands ($n = 1, 2, 3, 4$) are plotted for various F_ω in Figure 3.11. We see a decrease of $D_{B,n+1} < D_{B,n}$ for larger σ, so we can state that the regions of linear scaling are decreasing for higher spatial frequencies, with the exception of $D_{B,1}$. These differences of $D_{B,n}$ are converging for $F_\omega \to 0$ to $D_{B,n,F_\omega=0} = 0.521\pi\,|\forall n$. Also, it should be mentioned that in the oscillatory case (at sufficiently small F_ω) $D_{B,1}$ does not include $\sigma = 0$, because of the existence of the additional zero σ_* as described in Section 3.1.1.

When moving to larger F_ω and therefore leaving the oscillatory regime the higher bands $D_{B,n}\,|n > 1$ are getting smaller and finally disappear. On the other hand, $D_{B,1}$ becomes larger and includes $\sigma = 0$ at sufficiently large F_ω. One could think, that the enlarged $D_{B,1}$ and the fact that it includes $\sigma = 0$ may justify a phase retrieval according to linearization in the sense of TIE but in this near-field, over-damped regime non-local effects are dominant which is contradictory to the assumptions made in TIE (recall Section 2.2.4). The maximal length of $D_{B,1}$ is at around point where the diffractogram changes its behavior from oscillatory to overdamped. For even larger F_ω $D_{B,1}$ decreases but so does also the width in σ where we have an non-negligible value of the diffractogram.

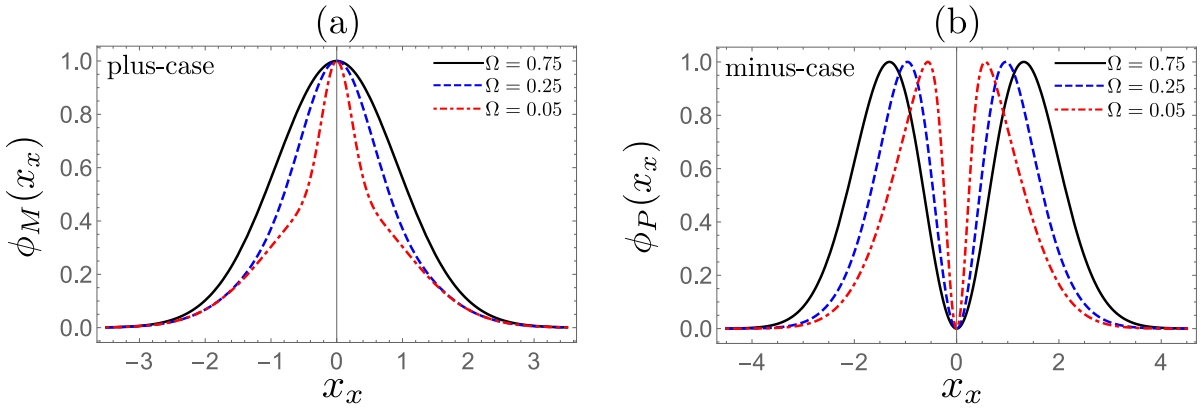

Figure 3.12.: 1D visualization of 2D TOBS phase-maps, with second scale factors $\Omega = 0.75, 0.25, 0.05$. (a) plus-case ϕ_{P}. (b) minus-case ϕ_{M}.

3.2. Two-scale objects with broad spectrum (TOBS)

After the investigation of Gaussian SOBS diffractograms we increase the complexity of the phase map by an additional scale. These two-scale objects with broad spectrum (TOBS) can be constructed by combining two SOBSs. We use a 2D-Gaussian, and add or subtract a second 2D-Gaussian, with a smaller width (determined by the factor $\Omega \leq 1$). That way, we obtain two phase maps (the plus- and the minus-case)

For the plus-case the phase-map reads

$$\phi_{\mathrm{P}}(\vec{x}_\perp) = \frac{1}{2}\left(e^{-\frac{\vec{x}_\perp^2}{2\omega}} + e^{-\frac{\vec{x}_\perp^2}{2\Omega\omega}}\right), \tag{3.31}$$

and the minus-case phase-map results in

$$\phi_{\mathrm{M}}(\vec{x}_\perp) = \frac{\Omega^{\frac{\Omega}{\Omega-1}}}{1-\Omega}\left(e^{-\frac{\vec{x}_\perp^2}{2\omega}} - e^{-\frac{\vec{x}_\perp^2}{2\Omega\omega}}\right). \tag{3.32}$$

The pre-factor (0.5 (plus-case) $\frac{\Omega^{\frac{\Omega}{\Omega-1}}}{1-\Omega}$ (minus-case)) is chosen to enforce that the maxima of these phase-maps are unity. In the minus case this leads to the effect that the width of the phase-map support increases for larger Ω.
Visualisations of Eq. (3.31) and Eq. (3.32) are given in Figure 3.12. For $\Omega = 1$ in the plus-case, the two scale object becomes a Gaussian (SOBS), the same is true in the limit $\Omega \to 0$ for the minus-case.

3.2.1. Non-linearity expansion and diffractogram properties

The diffractogram of the phase-maps Eq. (3.31) and Eq. (3.32) can be represented by a non-linearity expansion[4]. All numerical evaluations in this Chapter suffers an insignificant uncertainty, whose extend is estimated in the Appendix A.3.
We calculate both cases at once by combining these two equations into

$$\phi_{\mathrm{P/M}}(\vec{x}_\perp) = a_\pm \left(e^{-\frac{\vec{x}_\perp^2}{2\omega}} \pm e^{-\frac{\vec{x}_\perp^2}{2\Omega\omega}} \right) , \tag{3.33}$$

with $a_+ = 0.5$ and $a_- = \frac{\Omega^{\frac{\Omega}{\Omega-1}}}{1-\Omega}$.
After the substitution of Eq. (3.33) into Eq. (2.75) and performing the binomial expansions and Fourier transform we obtain the non-linearity expansion, in Fourier space, as

$$\mathfrak{F}g_{\mathrm{z},\pm} = 2\pi\omega\Omega \sum_{n=1}^{\infty} \frac{(iSa_\pm)^n}{n!} \sum_{j=0}^{n} \frac{(-1)^j n!}{(n-j)!j!} \sum_{k=0}^{n-j} \frac{(n-j)!}{(n-j)!j!} \sum_{l=0}^{j} \frac{j! e^{\frac{\sigma(k-k\Omega+(-j+n-2iF_\omega\pi)\Omega)(l-l\Omega+(j+2iF_\omega\pi)\Omega)}{2F_\omega\pi\Omega(k(\Omega-1)+l(\Omega-1)-n\Omega)}} (\pm 1)^{k+l}}{((j-l)!l!)(k(\Omega-1)+l(\Omega-1)-n\Omega} . \tag{3.34}$$

For the plus-case ($\mathfrak{F}g_{\mathrm{z},+}$) diffractogramms[5] at various Ω and $F_\omega = 0.01$ (a) as well as $F_\omega = 0.1$ (b) are plotted in Figure 3.13. At $F_\omega = 0.01$ the diffractograms show clearly oscillatory behavior, while at $F_\omega = 0.1$ the diffractogram transmute into a damped shape.
This transmution from an oscillatory to a damped behavior depends strongly on Ω, as we can see in Figure 3.13 (c). This is expected since we have admitted an additional small scale in our phase-map when we set Ω at a small value.

In the minus-case ($\mathfrak{F}g_{\mathrm{z},-}$) our diffractogram also shows oscillatory behavior at $F_\omega = 0.01$, see Figure 3.14 (a). In general, diffractograms, induced by arbitrary phase-maps of finite extent, are in oscillatory form for sufficiently large propagation distances (here represented by a small value of F_ω). In Section 3.1.2 we already investigated SOBS in the extreme far-field limit. The same is done for TOBS in Section 3.2.3. This extreme far-field representation is also generalized for multi-scale objects, and this generalization proves the statement of oscillatory behavior for arbitrary phase-maps in the far-field.
For $F_\omega = 0.1$ the diffractogram is in a damped form for small Ω but shows an oscillatory behavior for larger Ω, see Figure 3.14 (b). When we look at the Fourier transform of the diffractogram, see Figure 3.15, the plus-case (a) has one dominant frequency, which is sharper in comparison to the Gaussian SOBS case (recall Figure 3.4). The minus-case (b), on the other hand, has two maxima in its 1D Fourier transformed diffractogram. At small F_ω these maxima are close together and therefore appear like one dominant frequency (see Figure 3.14 (a)). The larger F_ω the further the two maxima are separated. The shift of the second maximum toward higher values of k for larger F_ω represents a higher frequency component in the diffractogram's oscillation. This effect can be observed in Figure 3.15. Note the shift of the first extrema towards lower values of σ for higher values of F_ω.

[4] See Eq.(2.75) for the generalized non-linearity expansion in real space.
[5] The definition $F_\omega = \frac{\omega}{\lambda z}$ is still given but can not be iterpreted as Fresnel number any more, due to the fact that we have now more than one scale. F_ω is still used to parameterize near or far-field regime.

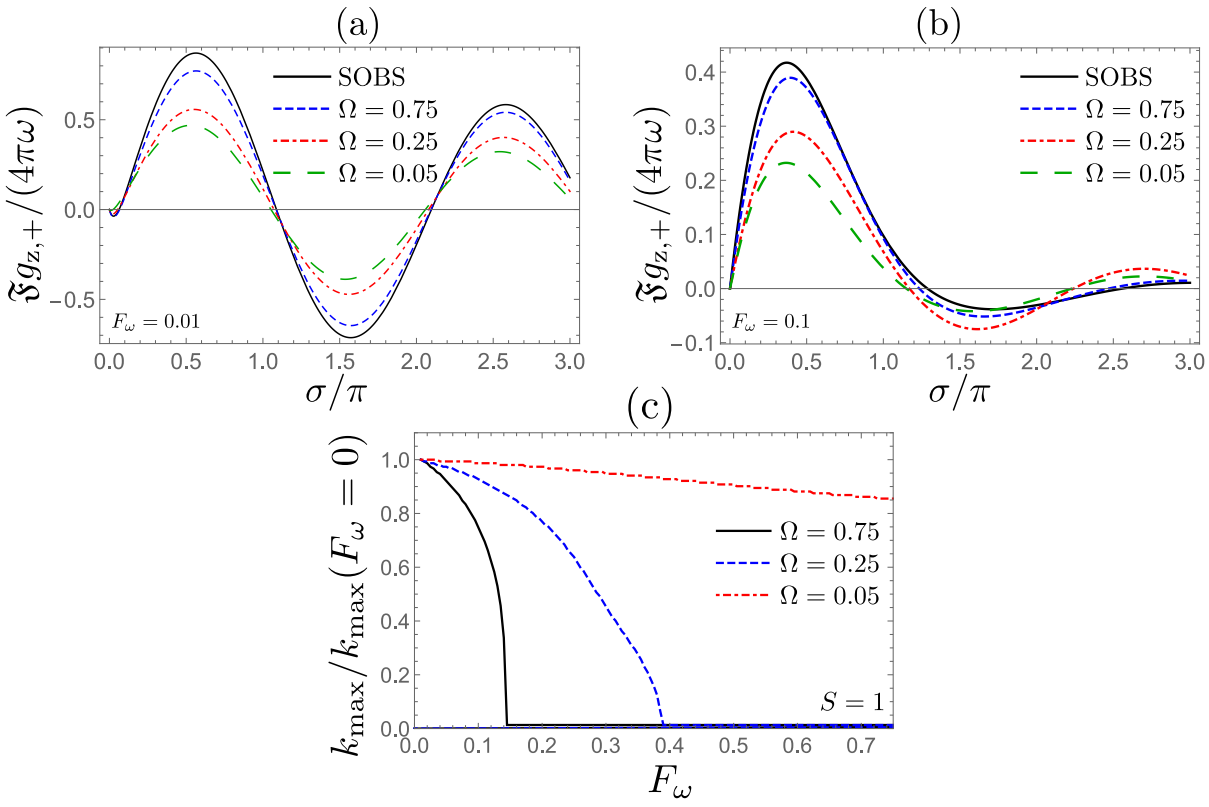

Figure 3.13.: Diffractograms of TOBS plus-case ($\mathfrak{F}g_{z,+}$) for $\Omega = 0.05, 0.25, 0.75$ and the Gaussian SOBS. (a): $F_\omega = 0.01$. (b): $F_\omega = 0.1$. (c): Transition from oscillatory to damped behavior represented by the normalized $k_{max}(F_\omega, S = 1)$ (analogue to Figure 3.4). Note the critical drops for the cases $\Omega = 0.75$ and $\Omega = 0.25$.

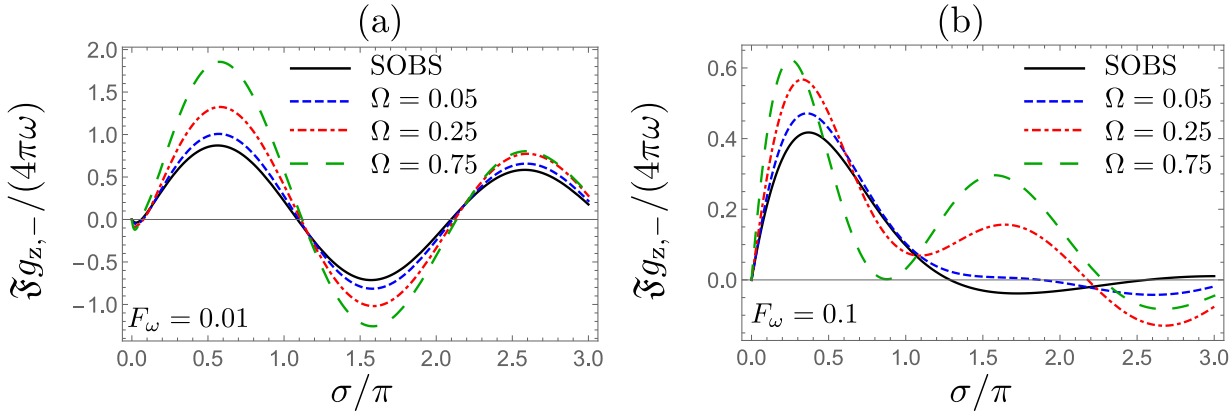

Figure 3.14.: Diffractograms of TOBS minus-case ($\mathfrak{F}g_{z,-}$) for $\Omega = 0.75, 0.25, 0.05$ and the Gaussian SOBS case. (a): $F_\omega = 0.01$. (b): $F_\omega = 0.1$.

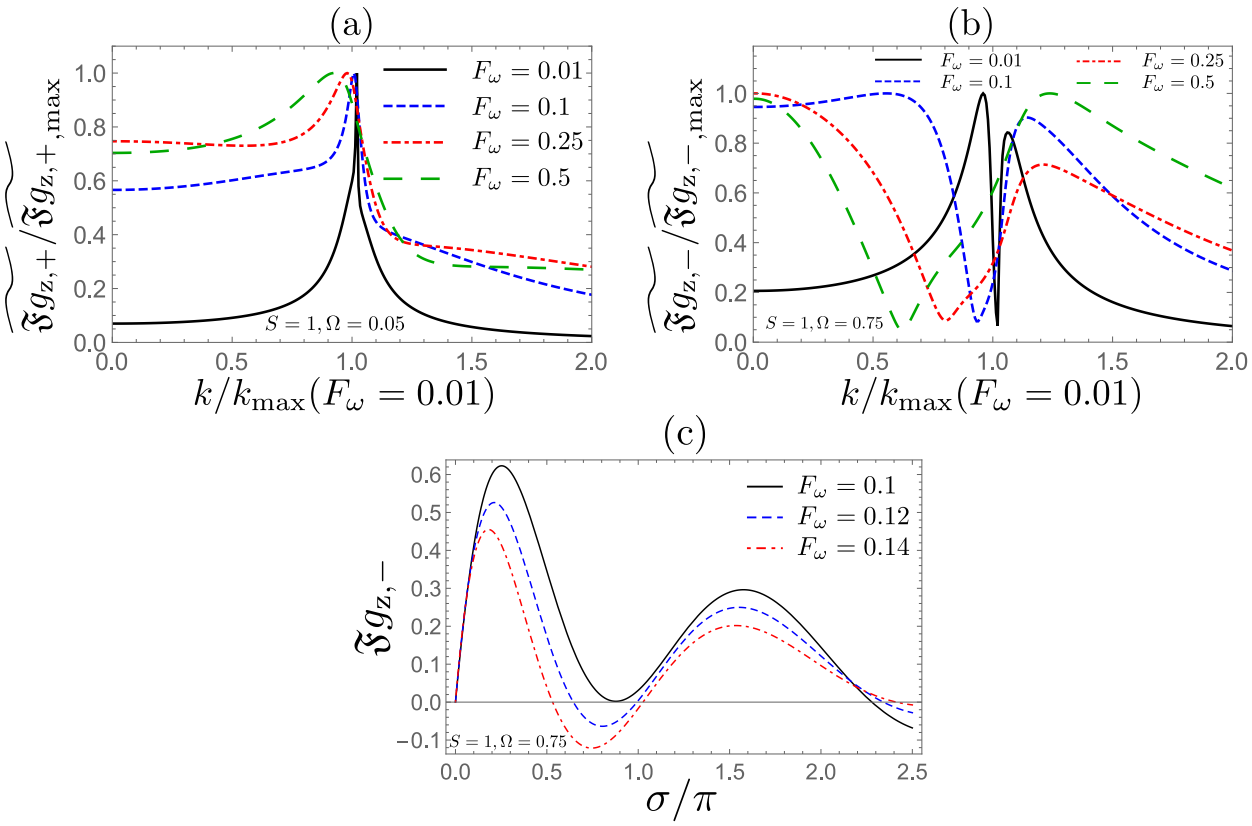

Figure 3.15.: Fourier transform of TOBS diffractograms. (a): Positive k-branche of 1D Fourier transformed diffractogram for $\Omega = 0.05$ and $S = 1$. Note the deformed shape of the peak for $F_\omega = 0.01$ in comparison to the SOBS-case in Figure 3.4 (a). (b): Positive k-branche of 1D Fourier transformed diffractogram for $\Omega = 0.75$ and $S = 1$. Note that the two maxima move away from each other when increasing F_ω. (c): TOBS minus-case diffractograms with $\Omega = 0.75$ and $F_\omega = 0.1, 0.12, 0.14$. Note the shift of the first two extrema towards lower values of σ for larger values of F_ω, indicating the shift of the second peak in (b) towards higher values of k.

To examine this additional oscillation in the minus-case we investigate the Fourier transform of the TOBS phase map and compare the plus- with the minus-case. In the plus-case as well as for the Gaussian SOBS phase-map the Fourier transform of all powers of ϕ is positive definite:

$$\begin{aligned}\mathfrak{F}^{(2)}\left[(\phi_{\text{Gaussian SOBS}}(\vec{x}_\perp))^n = e^{-\frac{\vec{x}_\perp^2}{2w}n}\right]\left(\vec{\xi}\right) &= \frac{2\pi\omega}{n}e^{\frac{2\pi^2\omega}{n}\vec{\xi}^2}\,,\\ \mathfrak{F}^{(2)}\left[(\phi_{\mathrm{P}}(\vec{x}_\perp))^n = (a_+)^n\left(e^{-\frac{\vec{x}_\perp^2}{2\omega}} + e^{-\frac{\vec{x}_\perp^2}{2\Omega\omega}}\right)^n\right]\left(\vec{\xi}\right) &= 2\pi\omega\Omega a_+^n\sum_{k=0}^{n}\frac{n!}{(n-k)!k!}\frac{e^{-\frac{2\pi^2\omega\Omega}{k+n\Omega-k\Omega}\vec{\xi}^2}}{k+n\Omega-k\Omega}\,,\end{aligned} \tag{3.35}$$

with $a_+ = 0.5$.

This is not given for the minus-case (note the $(-1)^k$ term):

$$\mathfrak{F}^{(2)}\left[(\phi_{\mathrm{M}}(\vec{x}_\perp))^n = (a_-)^n\left(e^{-\frac{\vec{x}_\perp^2}{2\omega}} - e^{-\frac{\vec{x}_\perp^2}{2\Omega\omega}}\right)^n\right]\left(\vec{\xi}\right) = 2\pi\omega\Omega a_-^n\sum_{k=0}^{n}\frac{n!}{(n-k)!k!}\frac{(-1)^k e^{-\frac{2\pi^2\omega\Omega}{k+n\Omega-k\Omega}\vec{\xi}^2}}{k+n\Omega-k\Omega}\,, \tag{3.36}$$

with $a_- = \frac{\Omega^{\frac{\Omega}{\Omega-1}}}{1-\Omega}$. Recall the onion-shell expansion of Eq. (2.80) and Eq. (2.81). There oscillations are caused in the far-field (small F_ω) by the $\sin\sigma$ term, the $\cos\sigma$ term and the local part $(\mathfrak{F}^{(2)}[\phi])^n$. When $(\mathfrak{F}^{(2)}[\phi])^n$ is positive definite and compact the dominant oscillation frequency is given by the $\sin\sigma$ and $\cos\sigma$ terms. Also, the Fourier transformed bilocal part $(\mathfrak{F}^{(2)}[\phi_+\phi_-])^n = \left(\mathfrak{F}^{(2)}[\phi_+] * \mathfrak{F}^{(2)}[\phi_-]\right)^n$ stays positive definite, so no additional oscillations with higher frequencies are expected for larger F_ω.
In the minus-case this Fourier transformed phase-map is not positive definite and therefore is able to induces the observed extra oscillations which becomes more relevant in the non-local regime (at larger F_ω).

In Gaussian SOBS diffractograms we observed that the first "regular" zero (we will refer to the zero around $\sigma/\pi = 1$ as the "first regular zero".) moves when we change the scaling factor S (recall Figure 3.1). This zero also moves in a TOBS diffractogram but its direction now depends on the shape of the phase-map. It is even possible to construct TOBS phase-maps, such that the first zero does not move to larger σ for increasing S as we can see in Figure 3.16 (a). The position of the first regular zero as a function for S is plotted in Figure 3.16 (b) for the Gaussian SOBS and the TOBS minus-case with $\Omega = 0.8$. Not only does the zero move in the opposite direction for our TOBS but the magnitude of speed is also much smaller.
This indicates that the scaling behavior depends on the phase-map shape, and therefore we will investigate the scaling linearity of our TOBS phase-maps in Section 3.2.2. This motivates investigations how this TOBS phase-maps influences the scaling linearity of the diffractogram.

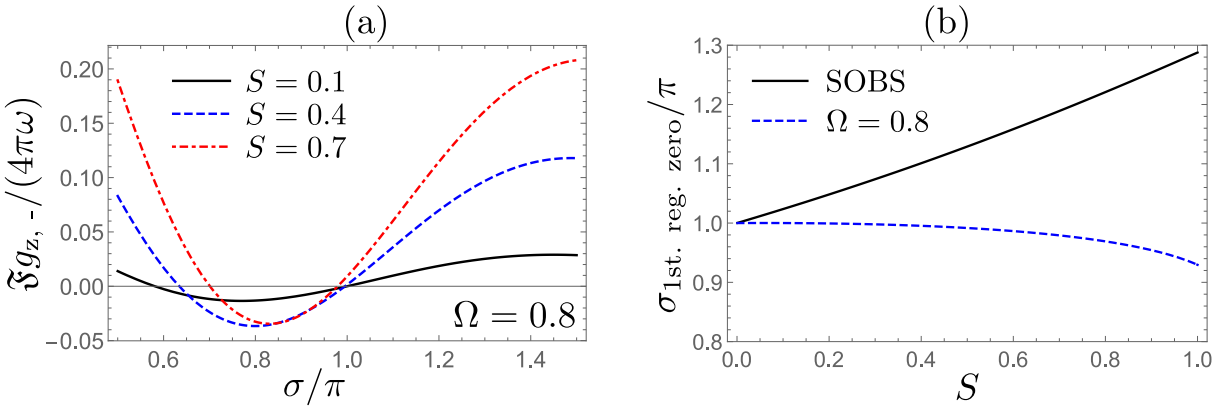

Figure 3.16.: Movement of first regular zero near $\sigma/\pi = 1$ in TOBS diffractogram (minus-case) when changing the scaling factor. (a): $\mathfrak{F}g_{z,-}(\sigma)$ at $F_\omega = 0.1$ and $\Omega = 0.8$ for various S. (b): Position of the first regular zero as function of S for the Gaussian SOBS and the TOBS minus-case with $\Omega = 0.8$. Note the different direction of movement.

3.2.2. Scaling linearity

In analogy to Section 3.1.4, we use D_S (defined in Eq. (3.27)) as measure of "scaling linearity" in our TOBS diffractograms.

In Figure 3.17 D_S is plotted as a function of F_ω and σ (analogue to Figure 3.9) for the plus-case and various values of Ω. The region of good scaling linearity (small D_S) increases the more the phase-map differs form the Gaussian SOBS phase-map. We note, for now, that the additional scale can lead to an increased region of good scaling-linearity.
The same region, for the minus-case, is plotted in Figure 3.18. Here we can see an additional region of non-linear scaling behavior, which is provoked by the shift of the additional zero and the intersections between diffractograms at different scaling factors, see Figure 3.19 (a). This leads to significant deviations from linear scaling behavior as we can see in Figure 3.19 (b). Here the appearence of the additional scale lead to a shrinkage of the continuous area of good scaling linearity in the F_ω-σ plane. Therefore, it is not possible to formulate universal statements on whether more scales always lead to better or worse scaling linearity.

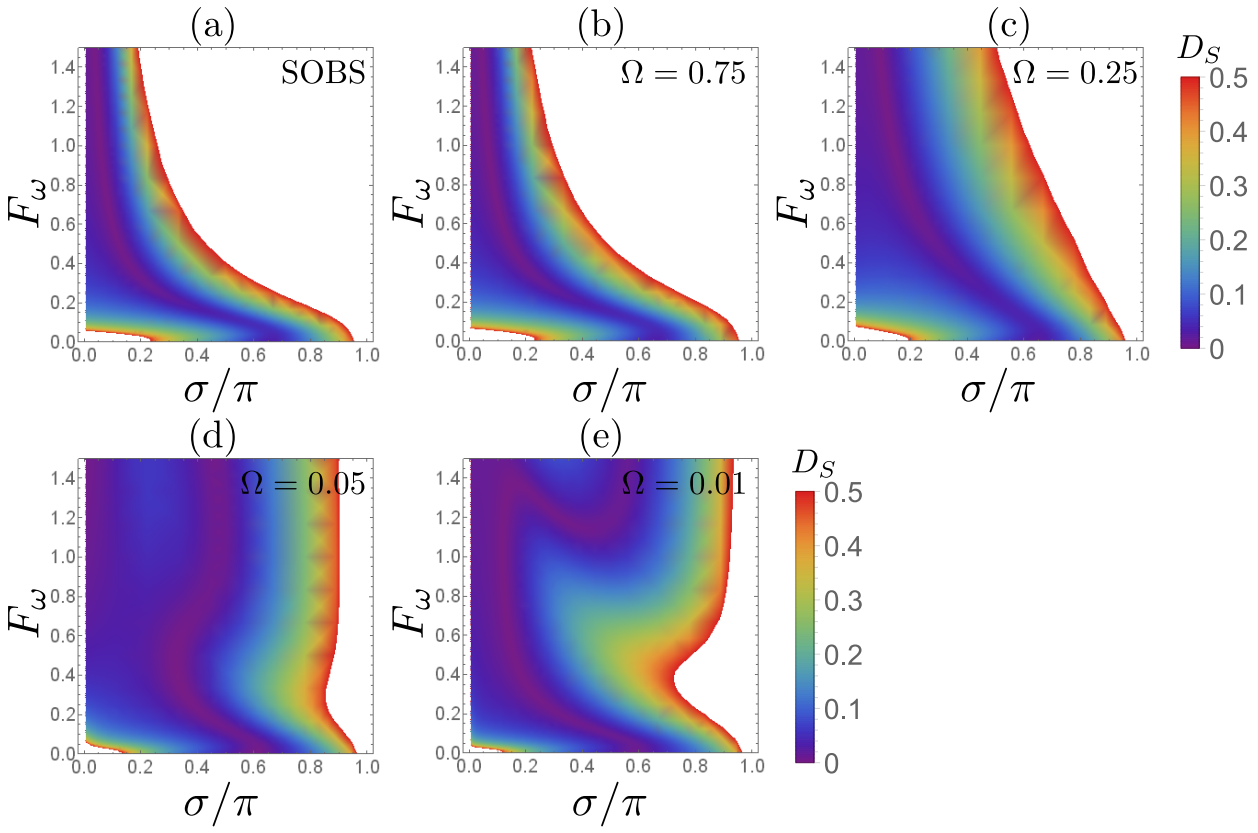

Figure 3.17.: D_S (for definition see Eq. (3.27)) of TOBS-diffractograms (plus-case) as a function of F_ω and $\sigma \leq 1$. The white regions represents $D_S > 0.5$. (a): The SOBS case ($\Omega = 1$), equal to Figure 3.9 (a). (b): $\Omega = 0.75$. (c): $\Omega = 0.25$. (d): $\Omega = 0.05$. (e): $\Omega = 0.01$. Note the increasing area of mostly linear scaling behavior the more the phase-map differs from the SOBS case.

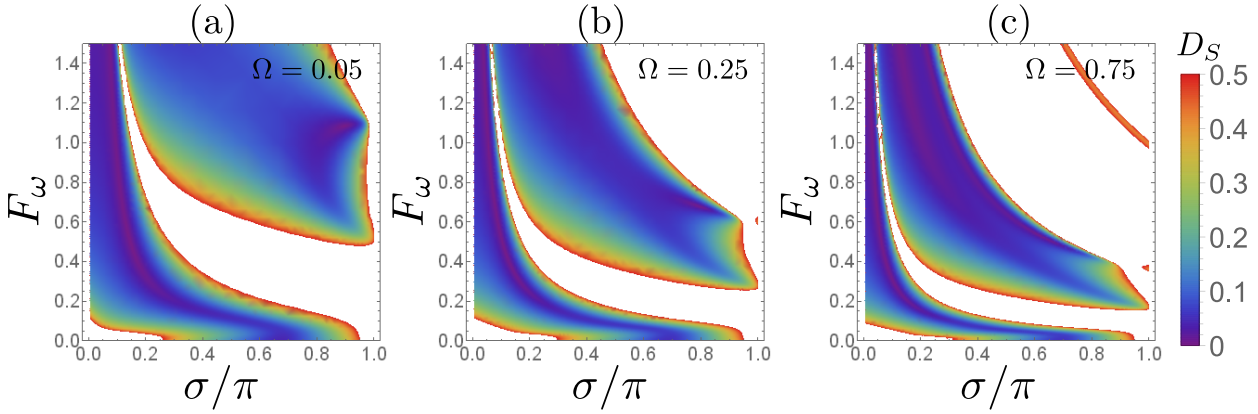

Figure 3.18.: D_S of TOBS-diffractograms (minus-case) as a function of F_ω and $\sigma \leq 1$. The white regions represents $D_S > 0.5$. (a): $\Omega = 0.05$. (b): $\Omega = 0.25$. (c): $\Omega = 0.75$. Note the small region of strong non-linear behavior induced by the movement of the additional zero (caused by the shape of the phase-map).

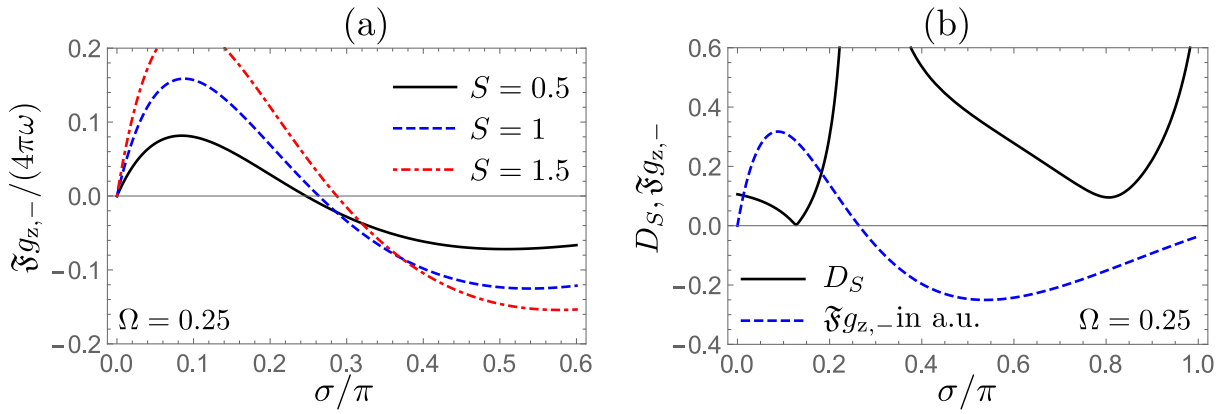

Figure 3.19.: Movement of additional zero under change of the scaling factor (a) and D_S (b) for TOBS diffractrogram (minus case $\Omega = 0.25$, $F_\omega = 0.4$).

In Figure 3.20 D_S is plotted as a function of Ω and σ for the plus- and minus-case and at $F_\omega = 0.1$, $F_\omega = 0.05$ and $F_\omega = 0.01$. The plus-case at $\Omega = 1$ is equal to the Gaussian SOBS case. We observe that the width of the D_S-bands in the plus-case does depend on Ω, but for $F_\omega = 0.1$ the first band[6] is relatively stable under changes in Ω. For decreasing F_ω this stability increases over the next bands, and at $F_\omega = 0.01$ we recognize only small changes within the bands. We also see an increase of the D_S-bands for smaller Ω, as we already observed in Figure 3.17.
The situation for the minus-case, on the other hand, is more complicated at small F_ω. The existence of the additional zero and its movement causes the bands to strongly depend on Ω. Only the first band (at $0 \leq \sigma/\pi \leq$) is continuous in Ω for $F_\omega = 0.1$ and relatively stable at $F_\omega = 0.05$. At $F_\omega = 0.01$ the bands are more or less constant in width and more stable in Ω.
In the extreme far-field limit $F_\omega \to 0$ all bands[7] $D_{B,n}$ exhibit the same shape and extension but the width still depends on Ω. In Figure 3.21 $D_{B,1}$ with $D_{\text{thr}} = 0.25$ is plotted as a function of Ω.

[6] We refer to the regions of good scaling linearity between integer σ/π as bands.
[7] For the definition of $D_{B,n}$ see Section 3.1.4.

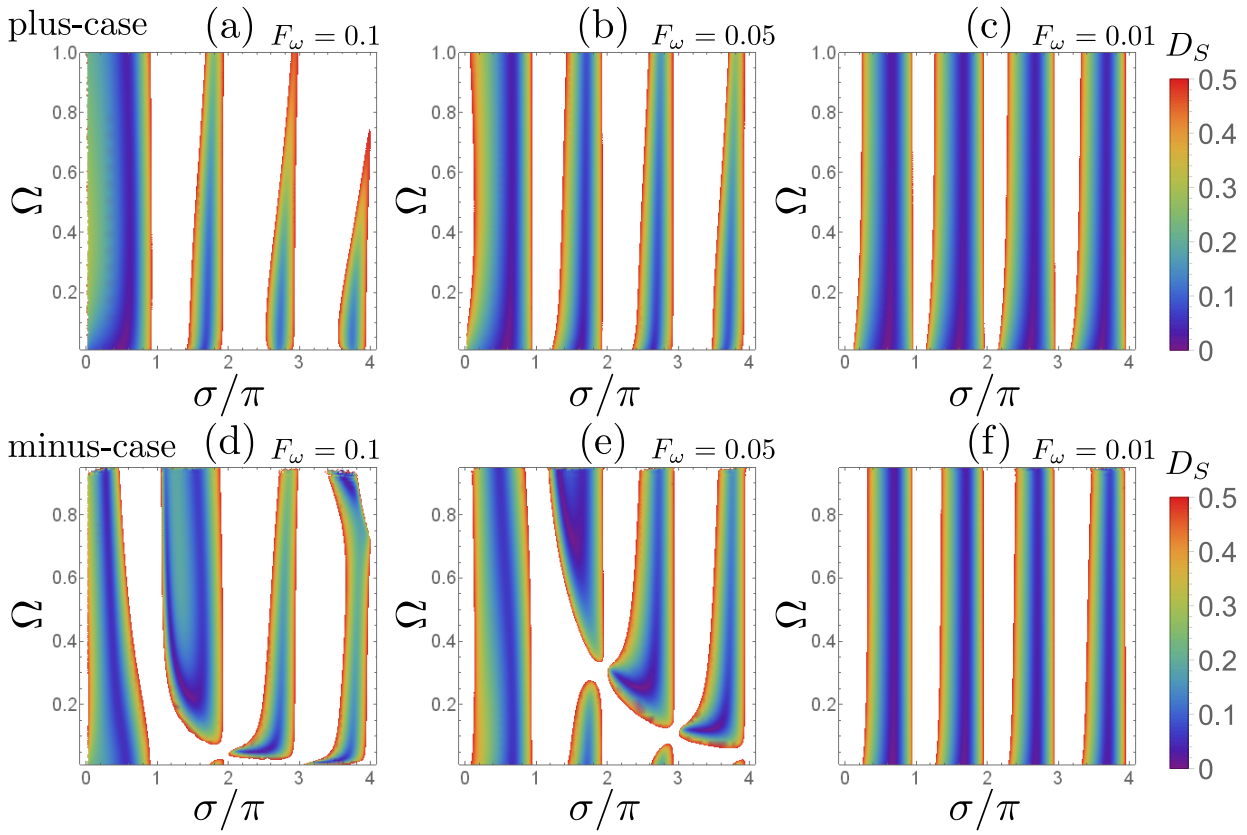

Figure 3.20.: D_S of TOBS-diffractograms plus- and minus-case as a function of Ω and σ. Plus-case: (a) $F_\omega = 0.1$ note the increased first "band". (b) $F_\omega = 0.05$. (c) $F_\omega = 0.01$ note the nearly equal wide "bands". Minus-case: (d) $F_\omega = 0.1$. (e)$F_\omega = 0.05$ note the more irregular behavior in comparison to the plus-case. (f) $F_\omega = 0.01$.

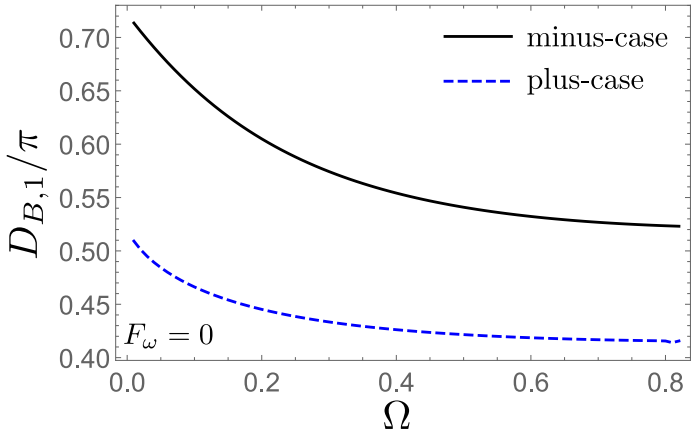

Figure 3.21.: First D-band $D_{B,1}$ of TOBS-diffractograms (plus- and minus-case) as a function of Ω at $F_\omega = 0$. The bands are defined by $D_S \leq 0.25$.

3.2.3. The extreme far-field

We discuss the extreme far-field of TOBS phase-maps in analogy to the SOBS-case in Section 3.1.2. As we already know, in the extreme far-field $F_\omega \to 0$ the zeroth onion-shell is a good approximation and is exact for $F_\omega = 0$. The zeroth onion-shell for our TOBS (**plus- and minus-case**) reads

$$\begin{aligned}\mathfrak{F}g_{\mathrm{z},0,\pm} = 4\pi\omega\Omega\cos(\sigma)\sum_{k=1}^{\infty}\frac{(-1)^k S^{2k}a_\pm^{2k}}{(2k)!}\sum_{j=0}^{2k}\frac{(2k)!(\pm1)^j}{((2k-j)!j!)(j+2k\Omega-j\Omega)}e^{-\frac{2\pi\Omega F_\omega}{j+2k\Omega-j\Omega}\sigma}\\ + 4\pi\omega\Omega\sin(\sigma)\sum_{k=0}^{\infty}\frac{(-1)^k S^{2k+1}a_\pm^{2k+1}}{(2k+1)!}\sum_{j=0}^{2k+1}\frac{(2k+1)!(\pm1)^j}{((2k+1-j)!j!)(j+(2k+1)\Omega-j\Omega)}e^{-\frac{2\pi\Omega F_\omega}{j+(2k+1)\Omega-j\Omega}\sigma}.\end{aligned} \tag{3.37}$$

We consider the limit $F_\omega = \frac{\omega}{\lambda z} \to 0$ and obtain

$$\begin{aligned}\lim_{F_\omega\to0}\mathfrak{F}g_{\mathrm{z},0,\pm} = 4\pi\omega\Omega\cos(\sigma)\sum_{k=1}^{\infty}\frac{(-1)^k S^{2k}a_\pm^{2k}}{(2k)!}\sum_{j=0}^{2k}\frac{(2k)!(\pm1)^j}{((2k-j)!j!)(j+2k\Omega-j\Omega)}\\ + 4\pi\omega\Omega\sin(\sigma)\sum_{k=0}^{\infty}\frac{(-1)^k S^{2k+1}a_\pm^{2k+1}}{(2k+1)!}\sum_{j=0}^{2k+1}\frac{(2k+1)!(\pm1)^j}{((2k+1-j)!j!)(j+(2k+1)\Omega-j\Omega)}.\end{aligned} \tag{3.38}$$

The generalization $N_{\omega,\Omega}$ of N_ω, introduced in Eq. (3.21), reads

$$N_{\omega,\Omega} = \begin{cases}\pi\omega(1+\Omega) & \text{for } \phi_P \text{ (plus-case)},\\ 2\pi\omega\Omega^{\frac{\Omega}{\Omega-1}} & \text{for } \phi_M \text{ (minus-case)}.\end{cases} \tag{3.39}$$

The coefficient $C(j)$ for the normalized diffractogram (for $\sigma > 0$) in the extreme far-field limit, as defined in Eq.(3.23), can be read from Eq. (3.38) as

$$C(j) = \begin{cases}\frac{4\cdot(\frac{1}{2})^j}{j(1+\Omega)}\sum_{k=0}^{j}\frac{j!}{(j-k)!k!}\frac{1}{k+j\Omega-k\Omega} & \text{for } \phi_P \text{ (plus-case)},\\ 2\Omega^{\frac{1}{1-\Omega}}\left(\frac{\Omega^{\frac{\Omega}{\Omega-1}}}{1-\Omega}\right)^j\sum_{k=0}^{j}\frac{(-1)^k j!}{(j-k)!k!}\frac{1}{k+j\Omega-k\Omega} & \text{for } \phi_M \text{ (minus-case)}.\end{cases} \tag{3.40}$$

A third example for a TOBS is an **elliptical phase-map**

$$\phi(x,y) = e^{-\frac{x^2}{2\omega} - \frac{y^2}{2\Omega\omega}}\,, \tag{3.41}$$

which is also an example for a non-isotropic phase-map.
The normalization $N_{\omega,\Omega}$ is given for the elliptical case by

$$N_{\omega,\Omega} = 2\pi\omega\sqrt{\Omega}\,. \tag{3.42}$$

The 2-D Fourier transform of ϕ^j reads

$$\mathfrak{F}[\phi^j(x,y)](\xi_x,\xi_y) = \frac{2\pi\omega\sqrt{\Omega}}{j} e^{-\frac{\pi^2\omega}{j}\left(\xi_x^2+\Omega\xi_y^2\right)}\,, \tag{3.43}$$

and in the limit $\omega \to 0$ reduces to (with the normalization $N_{\omega,\Omega}$)

$$\lim_{\omega\to 0} \mathfrak{F}[\phi^j(x,y)](\xi_x,\xi_y)\cdot N_{\omega,\Omega}^{-1} = \lim_{\omega\to 0} \frac{1}{j} e^{-\frac{\pi^2\omega}{j}\left(\xi_x^2+\Omega\xi_y^2\right)} = \frac{1}{j}\,. \tag{3.44}$$

And therefore we can read off the scaling coefficient as

$$C(j) = j^{-1}\,. \tag{3.45}$$

Comparing Eq. (3.45) with Eq. (3.24), we can see that in the extreme far-field it is not possible to distinguish between an elliptical and a Gaussian phase-map.

The extreme far-field of multi scale objects with broad spectrum (MOBS)[8]
MOBS phase-maps of spatial scales $\{\omega_i\}$ in the extreme far-field limit need to be normalized such that

$$\lim_{\kappa\to 0} N^{-1}_{\{\kappa\omega_i\}}\phi_{\{\kappa\omega_i\}}(\vec{x}_\perp)|_{S=1} = \delta^{(2)}(\vec{x}_\perp)\,. \tag{3.46}$$

Eq. (3.46) generalizes Eq. (3.21). We can write the phase-map as

$$\phi_{\{\omega_i\}}(\vec{x}_\perp) = SN_{\{\omega_i\}}\delta_{\{\omega_i\}}(\vec{x}_\perp)\,, \tag{3.47}$$

with

$$\lim_{\kappa\to 0}\delta_{\{\kappa\omega_i\}}(\vec{x}_\perp) = \delta^{(2)}(\vec{x}_\perp)\,. \tag{3.48}$$

The zeroth onion-shell, as given in Eq. (2.82), demands the evaluation of $\mathfrak{F}\left[\phi^j_{\{\omega_i\}}\right]$ for $j = 1, 2, ...$ Appealing to the Fourier convolution theorem, we have

$$\lim_{\kappa\to 0}\mathfrak{F}\left[\phi^j_{\{\omega_i\}}(\vec{x}_\perp)\right] = S^j \lim_{\kappa\to 0} N_{\{\kappa\omega_i\}}N^{j-1}_{\{\kappa\omega_i\}}\underbrace{\mathfrak{F}\left[\delta_{\{\kappa\omega_i\}}\right] * ... * \mathfrak{F}\left[\delta_{\{\kappa\omega_i\}}\right]}_{j-1 \text{ convolutions}}\,. \tag{3.49}$$

Let us define the dimensionless quantity

$$W(j-1,\{\kappa\omega_i\}) := N^{j-1}_{\{\kappa\omega_i\}}\underbrace{\mathfrak{F}\left[\delta_{\{\kappa\omega_i\}}\right] * ... * \mathfrak{F}\left[\delta_{\{\kappa\omega_i\}}\right]}_{j-1 \text{ convolutions}}\,. \tag{3.50}$$

The coefficients $C(j)$ can be identified as

$$C(j) = \lim_{\kappa\to 0} W(j-1,\{\kappa\omega_i\})\,. \tag{3.51}$$

The dependence of $C(j)$ on the dimensionless ratios $\omega_i/\omega_j\,|\,(i > j)$ is strong suppressed. Thus the extreme far-field limit of the normalized diffractogram, in analogy to Eq. (3.23), reads

$$\begin{aligned}\lim_{\kappa\to 0}\frac{\mathfrak{F}g_z}{N_{\{\kappa\omega_i\}}} &= 2\sin(\sigma)\sum_{k=0}^{\infty}\frac{(-1)^k}{(2k+1)!}S^{2k+1}C(2k+1) + 2\cos(\sigma)\sum_{k=1}^{\infty}\frac{(-1)^k}{(2k)!}S^{2k}C(2k)\\ &= S_s(S)\sin(\sigma) + S_c\cos(\sigma)\,.\end{aligned} \tag{3.52}$$

This proves that an arbitrary phase-map has oscillatory behavior in the far-field. Also, it is conceivable that Eq.(3.52) has practical implications if phase-maps can be scaled physically, because the phase-map's entire shape information is given by $C(j)$. Note that there can be different shaped phase-maps who exhibit same the same $C(j)$ as we can see by comparing (3.45) to Eq. (3.24).

[8]This calculation has already been done in [19].

3.3. Multi-scale objects with broad spectrum (MOBS)

Phase-maps induced by projection through real samples usually contain a huge amount of scales. Therefore, we investigate multi-scale objects of broad spectrum in this section. We were able to treat the SOBS- and TOBS-case semi-analytically by performing the non-linearity or the onion-shell expansions, however we have to resort to a numerical treatment here, which requires the use of a pixelized field of view.

3.3.1. MOBS diffractograms

We permit arbitrary phase-maps $\phi(\vec{x}_\perp)$ but quantize $\vec{x}_\perp = \begin{pmatrix} x \cdot \triangle x \\ y \cdot \triangle x \end{pmatrix}$ with integer x, y and the pixel-size (edge-size) $\triangle x$. We still consider only pure-phase objects, so that the wave field at the exit plane ($z = 0$) reads

$$\psi(\vec{x}_\perp, z = 0) = \sqrt{I_0} e^{i\phi(\vec{x}_\perp, z=0)} \,. \tag{3.53}$$

To obtain the intensity at the detector-plane we need to propagate the wave field to the distance z. This is done by convolution with the Fresnel propagator (for a derivation see Section 2.1.7). The Fresnel propagator reads

$$\bar{P}^K(z, \vec{x}_\perp) = -\frac{i}{\lambda z} e^{i\frac{2\pi z}{\lambda}} e^{i\frac{\pi}{\lambda z}(\vec{x}_\perp)^2} \,, \tag{3.54}$$

subject to wave length λ.
Because the Fresnel propagator is defined for arbitrarily large $|\vec{x}_\perp|$, it is not convenient to perform the convolution numerically. Instead we exploit the Fourier convolution theorem[9]. The Fourier representation of the Fresnel propagator reads

$$\widetilde{\bar{P}^K} = \mathfrak{F}^{(2)} \left[\bar{P}^K(\vec{x}_\perp, z) \right] \left(\vec{\xi}, z \right) = e^{i\frac{2\pi z}{\lambda}} e^{-i\pi\lambda z \vec{\xi}^2} \,. \tag{3.55}$$

Because we are only interested in the intensity at z

$$I_\mathrm{z} = \psi^* \psi \,, \tag{3.56}$$

we can neglect the constant factor $e^{i\frac{2\pi z}{\lambda}}$ in Eq.(3.55). Therefore, we obtain the intensity at the detector plane (z) as

$$I_\mathrm{z}(\vec{x}_\perp) = \left| \mathfrak{F}_\mathrm{D}^{(-2)} \left[\mathfrak{F}_\mathrm{D}^{(2)} \left[e^{i\phi(\vec{x}_\perp, z=0)} \right] \left(\vec{\xi} \right) \cdot e^{-i\pi\lambda z \vec{\xi}^2} \right] (\vec{x}_\perp) \right|^2 \,, \tag{3.57}$$

where $\mathfrak{F}_\mathrm{D}^{(2)}$, $\mathfrak{F}_\mathrm{D}^{(-2)}$ denote the 2D discrete Fourier transform (DFT) and the 2D inverse discrete Fourier transform (iDFT), respectively.
We perform the 2D DFT of the intensity contrast g_z (defined by $g_\mathrm{z} = \frac{I_0 - I_\mathrm{z}}{I_0}$)

$$\mathfrak{F} g_\mathrm{z} \left(\vec{\xi} \right) = \mathfrak{F}_\mathrm{D}^{(2)} \left[g_\mathrm{z}(\vec{x}_\perp) \right] \left(\vec{\xi} \right) \,. \tag{3.58}$$

Note that the DFT is defined for infinite periodical signals, which is not the case for g_z. To nevertheless obtain decent results, it is convenient to frame g_z (which is stored as a matrix) with a sufficiently large number of elements with the value zero (zero-padding).
To obtain the diffractogram, as defined in Section 2.2.4, we perform the angular average, and make the substitution $\sigma = \frac{2\pi^2 z}{K} \vec{\xi}^2$

$$\mathfrak{F} g_\mathrm{z}(\sigma) = \frac{1}{2\pi} \int_0^{2\pi} \mathfrak{F} g_\mathrm{z} \left(\vec{\xi} = \sqrt{\sigma \frac{K}{2\pi^2 z}} \begin{pmatrix} \cos\varphi \\ \sin\varphi \end{pmatrix} \right) d\varphi \,, \tag{3.59}$$

[9] Fourier convolution theorem: $\mathfrak{F}[f \cdot g] = \mathfrak{F}[f] * \mathfrak{F}[g]$.

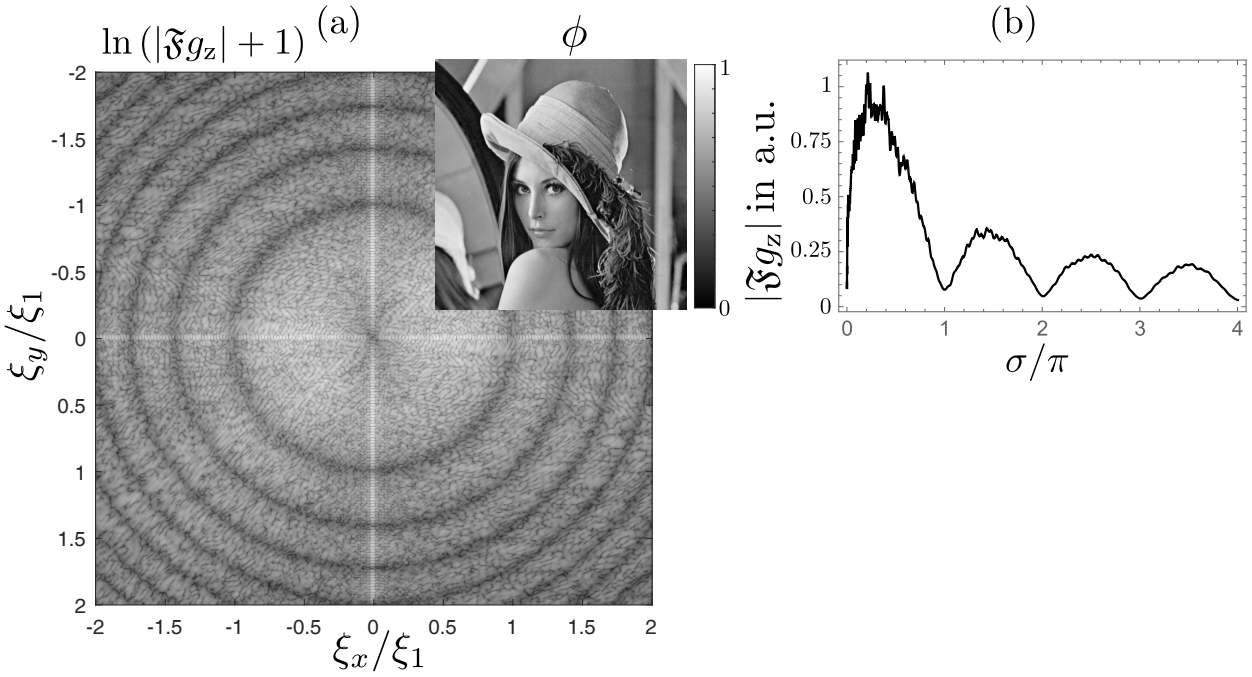

Figure 3.22.: MOBS diffractogram $|\mathfrak{F}g_z(\vec{\xi})|$ and $|\mathfrak{F}g_z(\sigma)|$, simulated with $E = 1\text{keV}$ ($\lambda = 1.2\text{nm}$), $z = 1\text{m}$, $S = 1$, and a pixel size $\Delta x = 1.6\mu\text{m}$ with 1024×1024 pixel. (a): Lena phase-map and 2D diffractogram $|\mathfrak{F}g_z(\vec{\xi})|$ illustrated by $\log(1 + |\mathfrak{F}g_z(\vec{\xi})|)$. The position of the first minimum is at $|\xi| = \xi_1$. (b): Angular averaged diffractogram $|\mathfrak{F}g_z(\sigma)|$ with the substitution $\sigma/\pi = \lambda z\vec{\xi}^2$. The diffractogram has been smoothed by 2D convolution of $\mathfrak{F}g_z(\vec{\xi})$ with a 2D Gaussian filter (variance of 1 pixel which equates a variance of $\sigma_\xi = \frac{1}{2\Delta x}$) before performing the angular average.

An example of $\mathfrak{F}g_z\left(\vec{\xi}\right)$ and the diffractogram $\mathfrak{F}g_z(\sigma)$ for a multi-scale phase-map is given in Figure 3.22. The Fourier transformed intensity contrast $\mathfrak{F}g_z\left(\vec{\xi}\right)$ contains complex values, therefore we use the absolute value of the diffractogram for their further treatment. This is not the case for the Gaussian-SOBS and TOBS phase maps, defined in Section 3.1 and 3.2, because these phase-maps are 2D spherical symmetric. Therefore these SOBS and TOBS phase-maps are even ($\phi(\vec{x}) = \phi(-\vec{x})$), and thus their Fourier transform are real [20].

To investigate the scaling behavior of the MOBS diffractogram we normalize and shift the phase-map so that the maximum $\phi_{\max} = 1$ and the minimum $\phi_{\min} = 0$, respectively. A typical MOBS phase-map is the "Lena test pattern" [21] as illustrated in Figure 3.22 (a).

In Figure 3.23 the diffractogram (normalized to its maximum value) is plotted as a function of σ/π for various S and the propagation distance $z = 0.05\text{m}$ (a) respectively $z = 20\text{m}$ (b). We can see that the diffractogram's shape transmutes in both cases from an oscillatory form at small values of S to a more damped shape at higher values of S.
Analog to the first regular zero, as mentioned in Section 3.2.1, we define σ_1 as the position of the minimum of $|\mathfrak{F}g_z|$ near $\sigma = \pi$.
In Figure 3.23 (c) and (d) σ_1 is plotted as a function of S. For $z = 0.05\text{m}$ (c) we see a small movement of σ_1 until S exceeds a value of around $S \approx 4$. For larger values of S we can observe a rapid upward movement of σ_1. This is caused by the transition to an over-damped shape, where the minima caused by the sine modulation as foreseen by the the zeroth onion-shell (far field situation, recall Eq. 2.82) disappear. The extent of σ_1's movement before the transition to an over-damped shape is very small in comparison to the movement of the first regular zero in the Gaussian SOBS case (recall Figure 3.16 (b)) which likely is caused by the huge amount of scales in the phase-map. As we have discussed in Section

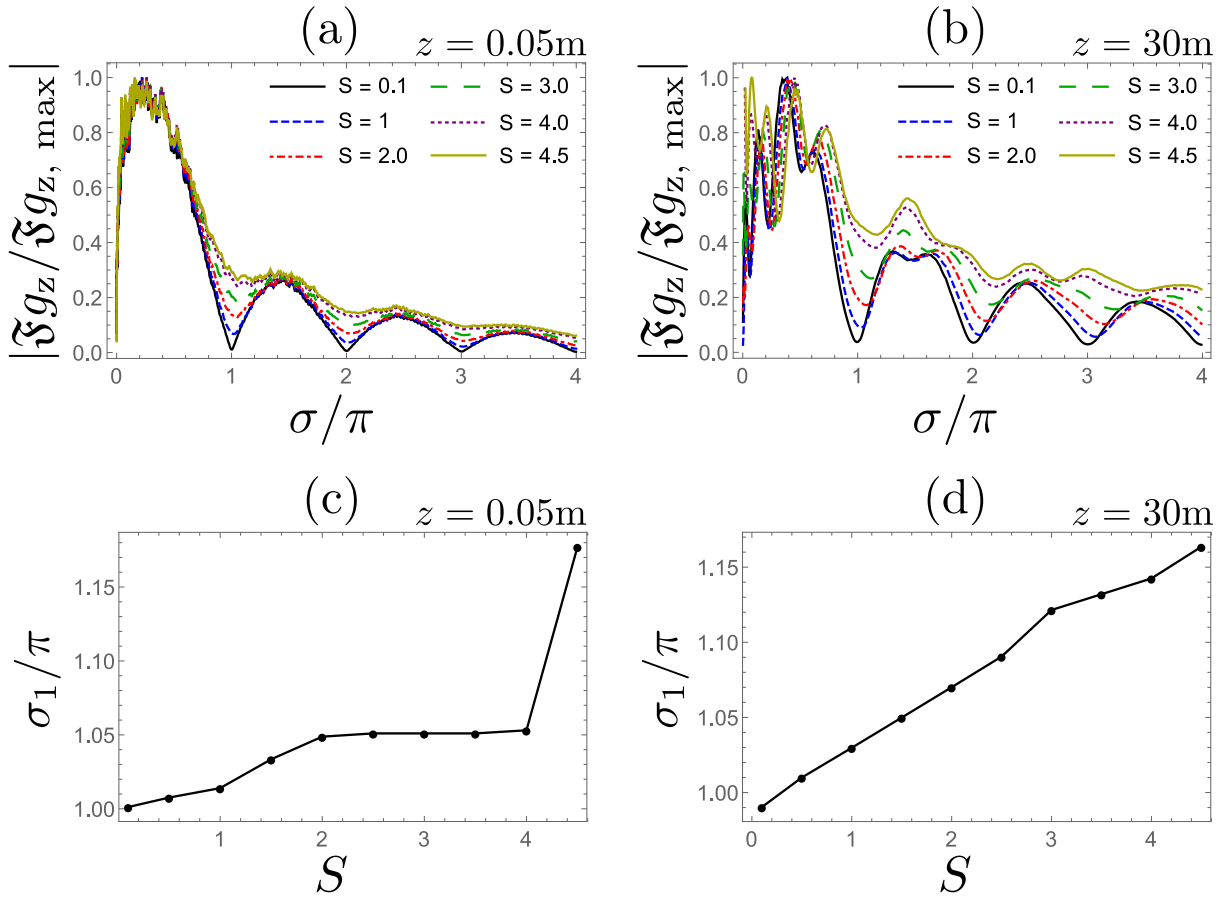

Figure 3.23.: MOBS diffractograms $|\mathfrak{F}g_z(\sigma)/\mathfrak{F}g_{z,\,\max}|$ and position of first minimum as a function of S. Simulated with a pixel size of $\Delta x = 1.6\mu$m with 1024×1024 pixel and $E = 1$keV. (a): Near field $z = 0.05$m, Note the more damped shape for larger values of S. (b): $z = 30$m, note the shift of the first minimum depending on S. (c): Position of the first minimum σ_1 as a function of S at $z = 0.05$m. (d): Position of the first minimum σ_1 as a function of S at $z = 30$m.

3.2.1 it is possible to construct phase-maps where σ_1 moves to lower values for increasing S so it is likely that complex phase-maps with a large amount of independent scales can suppress this movement. At $z = 30$m the movement of σ_1 is smoother in S, see Figure 3.23 (d). Larger values of z correspond to smaller values of F_ω in the Gaussian-SOBS case, where we know that a small value of F_ω requires a larger value of S for the diffractogram to be over-damped. This can explain why we do not see the strong increase of σ_1 at $S \approx 4$ here. Note that the extent of σ_1's movement is, in this case, also much smaller than in the Gaussian-SOBS case.

3.3.2. Scaling linearity

To analyze the scaling linearity we need to adjust our measurement D_S, defined in Eq.(3.27), such that it is useable for discrete and numerically calculated diffractograms.
To calculate D_S, a sufficient number[10] N of diffractograms with S_n ranging between S_1 and S_2 are needed. We define the derivative as

$$\partial_S \mathfrak{F} g_z\left(S_{n'}\right) = \frac{\mathfrak{F} g_z(S_{n+1}) - \mathfrak{F} g_z(S_n)}{S_{n+1} - S_n}\,, \tag{3.60}$$

with $S_{n'} = \frac{S_n + S_{n+1}}{2}$ and $S_{n+1} - S_n = \frac{S_2 - S_1}{N}$. The larger the value of N the better Eq.(3.60) approximates a derivative. Based on a stack of N diffractograms we therefore obtain a stack of $N-1$ derivatives $\partial_S \mathfrak{F} g_z\left(S_{n'}\sigma\right)$.
The standard deviation of the fist derivative reads

$$\mathrm{StDe}(\sigma) = \sqrt{\frac{1}{N-2}\sum_{n'=1}^{N-1}\left|\frac{1}{N-1}\sum_{k=1}^{N-1}\partial_S \mathfrak{F} g_z(S_k,\sigma) - \partial_S \mathfrak{F} g_z(S_{n'},\sigma)\right|^2}\,. \tag{3.61}$$

We normalize $\mathrm{StDe}(\sigma)$ to the mean value of the diffractogram and obtain

$$D_S(\sigma) = \frac{\mathrm{StDe}(\sigma)}{\frac{1}{N}\sum_{n=1}^{N}\mathfrak{F} g_z(S_n,\sigma)}\,. \tag{3.62}$$

In the limit $N \to \infty$ Eq. (3.62) becomes Eq.(3.27).

We use the "Lena phase-map", see Figure 3.22 (a) and the scaling window $S = [0, 1.5]$. The phase-map is normalized and shifted such that its minimum value is $\phi_{\min} = 0$ and its maximum $\phi_{\max} = 1$ at $S = 1$. The diffractogram $|\mathfrak{F} g_z(\sigma)|$ and D_S for $z = 0.2$m are plotted in Figure 3.24 (a).
Like the SOBS (Section 3.1.4) and TOBS (Section 3.2.2) cases, we can see that D_S gets maximal at integer values of σ/π, which is where the minima of the diffractogram are. This maximal non-linear scaling is most likely caused by the movement of the minima in $|\mathfrak{F} g_z(\sigma)|$ when changing the value of S.

In analogy to Section 3.1.4, we can identify D-bands where $D_s < D_{\mathrm{tr}}$. We refer to the bands length as $D_{B,n}$ with $n = 1, 2, \ldots$.
In Figure 3.24 the length of the first four bands, with $D_{\mathrm{tr}} = 0.25$, is plotted as a function of the propagation distance z. Because we can only calculate D_S for discrete values of σ, due to the finite number of pixels, there is an increased uncertainty of $D_{B,n}$ in comparison to the SOBS and TOBS case. This uncertainty has been estimated and is indicated in the plot.
In the range $0.2\mathrm{m} \leq z \leq 10\mathrm{m}$ we can not recognize a uniform dependence of D_B on z in the way we saw in the SOBS case (recall Figure 3.11) for D_B in dependence of F_ω. We also see that the D-bands are wider in the MOBS than in the SOBS case which is in good agreement with the observation that the first minimum moves much slower in the MOBS case than the first regular zero in the SOBS case. This latter observation was discussed in Section 3.3.1.

[10] Here we use $N = 100$. In the appendix A.4 an estimate for the convergence of D_S in N is given.

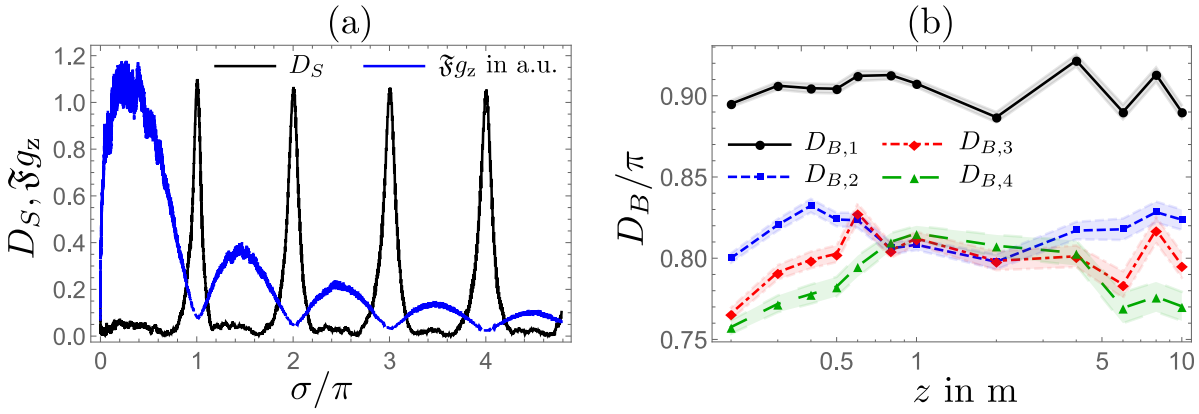

Figure 3.24.: MOBS (Lena phase-map, 1024×1024 pixel) diffractogram and D_S calculated with $E = 1\text{keV}$ and pixel size $\Delta x = 1.6\mu\text{m}$. (a): $|\mathfrak{F}g_z(\sigma)|$ in arbitrary units and $D_S(\sigma)$ at $z = 0.2\text{m}$. (b): First four D-bands $D_{B,1}, D_{B,2}, D_{B,3}, D_{B,4}$ for various z (the points are connected for better visualization).

3.3.3. Modulation contrast transfer of phase retrieval

In Section 2.2.4 we introduced two approaches for phase retrieval. The CTF approach, see Eq. (2.71) and the TIE approach, see Eq.(2.72). Both approaches require $\mathfrak{F}g_z\left(\vec{\xi} = 0\right) = 0$ which can not be assured when we make use of the DFT and finite pixel size. Therefore, we chose a pragmatic regularization [22] and modify Eq.(2.72) (TIE) as follows

$$\mathfrak{F}\phi = \frac{\mathfrak{F}g_z}{2\sigma + \alpha}\,, \tag{3.63}$$

with the regularization parameter $\alpha \ll 1$. For the following treatment we chose $\alpha = 10^{-2.5}$.
In the CTF approach poles arise for non-vanishing $\mathfrak{F}g_z(\vec{\xi})$ at the frequencies $\vec{\xi}^2\lambda z = \sigma/\pi = n$ (n integer). Therefore, we modify Eq. (2.71) as

$$\mathfrak{F}\phi = \mathfrak{F}g_z \frac{\operatorname{sgn}(\sin\sigma)}{2|\sin\sigma| + \alpha}\,, \tag{3.64}$$

where sgn denotes the sign function with $\operatorname{sgn}(x) = \frac{x}{|x|}$ for $x \neq 0$ and $\operatorname{sgn}(0) = 0$.

In Figure 3.25 the phase-map (a) with $S = 0.1$ is propagated (recall Eq. (3.57)) across the distance $z = 1\text{m}$ using a monochromatic beam with $E = 10\text{keV}$ ($\lambda = 0.124\text{nm}$). The intensity I_z at the detector-plane is given in Figure 3.25 (b). The retrieved phase-maps are shown in (c) where retrieved by the TIE approach and (d) by the CTF approach. Differences in the TIE and CTF approach are barley visible here.
We also recognize that the contrast of the retrieved phase-maps is clearly poorer compared to the original phase-map. This effect is even stronger in homogeneous regions, implying that the retrieval of low spatial frequencies suffer from a loss of contrast.

We increase the propagation distance to $z = 10\text{m}$ and repeat the phase retrieval, leaving energy, pixel-size and original phase-map unchanged. The results are given in Figure 3.26, TIE approach in (c) and CTF in (d). Here we can see that the TIE phase-map clearly is restored with a poorer quality than the CTF phase-map. Due to the larger propagation distance the linearization in z causes TIE to become an efficient low-pass filter.
Beside this we recognize that the contrast for lower spatial frequencies is improved in comparison to the case of $z = 1\text{m}$ in Figure 3.25.

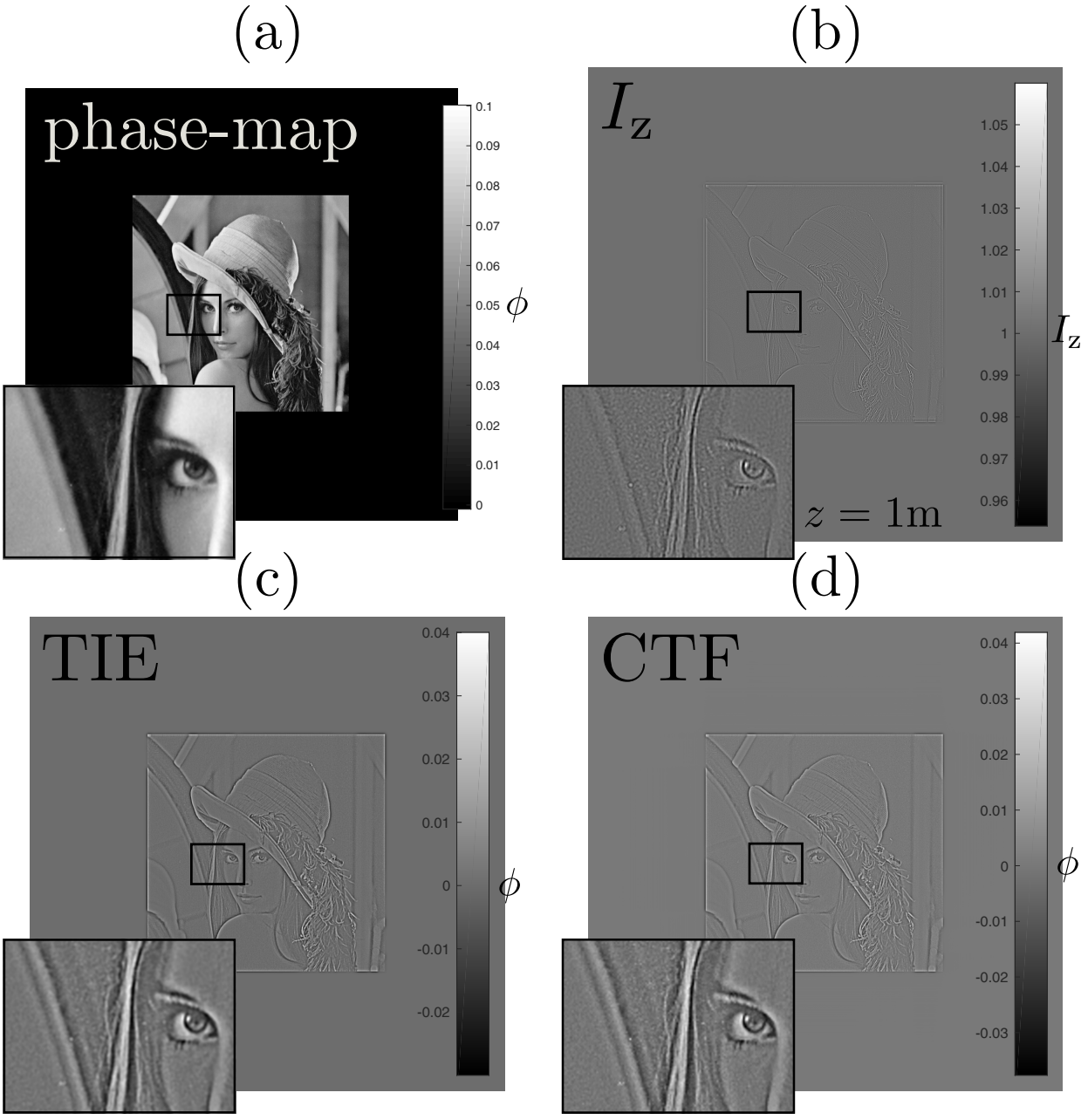

Figure 3.25.: Forward propagation with $E = 10\text{keV}$, $z = 1\text{m}$, phase-map (a) size 4096×4096 pixel (Lena 2048×2048 pixel plus zero-padding), $S = 0.1$, pixel size $\Delta x = 1.6\mu\text{m}$. (b): Intensity I_z at the detector plane. (c): Retrieved phase with TIE approach. (d): Retrieved phase with CTF approach. Note the loss off contrast in comparison to the original phase-map (a).

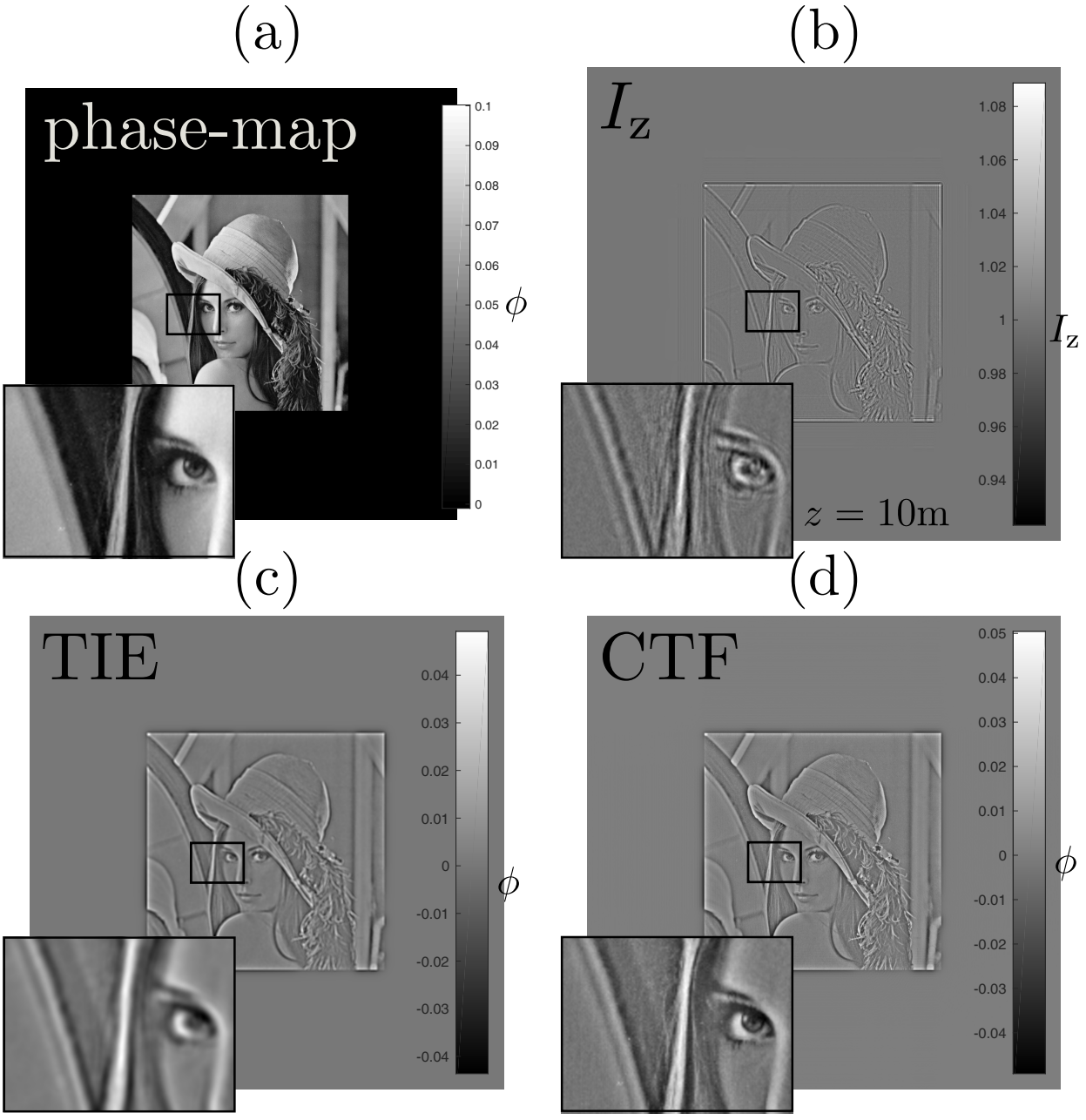

Figure 3.26.: Forward propagation with $E = 10\text{keV}$, $z = 10\text{m}$, phase-map (a) size 4096×4096 pixel (Lena 2048×2048 pixel plus zero-padding), $S = 0.1$, pixel size $\Delta x = 1.6\mu\text{m}$. (b): Intensity I_z at the detector plane. (c): Retrieved phase with TIE approach. (d): Retrieved phase with CTF approach. Note the poorer sharpness of the TIE retrieved phase-map in comparison to the CTF approach.

The observed contrast differences of the TIE and CTF approaches in dependence of spatial resolution and propagation distance motivates a more systematical investigation. We look at the forward propagation and phase retrieval as a system with the original phase-map as input and the retrieved phase-map as output. Here we need a quantity which represents the transfer of contrast (input to output) in dependence of the spatial frequency. Therefore, we define the phase-map as

$$\phi_{\mathrm{pm}}(x,y) = \frac{S}{2}\left(\sin\left(\frac{2\pi f}{N}\cdot x\right)+1\right), \tag{3.65}$$

where S denotes the scaling factor, N the number of pixels in x-direction, and f the number of maxima in the phase-map (in x direction), defining the spatial frequency ζ as

$$\zeta := \frac{f}{N\cdot\Delta x}, \tag{3.66}$$

where Δx denotes the pixel size. Such a sine-shape test-pattern is a common method to specify imaging systems [23].

We define the contrast of the phase map as

$$C_{\mathrm{pm}} := \max(\phi_{\mathrm{pm}}) - \min(\phi_{\mathrm{pm}}) = S\,. \tag{3.67}$$

Similarly, we define the contrast of the retrieved phase-map ϕ_{ret} as

$$C_{\mathrm{ret}}(\zeta) := \max(\phi_{\mathrm{ret}})(\zeta) - \min(\phi_{\mathrm{ret}})(\zeta)\,, \tag{3.68}$$

which depends on ζ.

To classify the retrieval system we define the modulation transfer function (MTF)[24] as

$$\mathrm{MTF}(\zeta) := \frac{C_{\mathrm{ret}}(\zeta)}{C_{\mathrm{pm}}}\,. \tag{3.69}$$

Under the assumption that the phase-map is not deformed by the propagation-retrieval-system, a MTF value of 1 implies a perfect contrast transfer and a smaller value of MTF a loss of contrast.

In Figure 3.27 MTFs are plotted for $S = 0.1$ and $E = 10$keV at the propagation distance $z = 1$m (a) and $z = 10$m (b) for the TIE and CTF approach. At $z = 1$m we see that MTF rises slowly for increasing ζ and therefore has a low value for small values of ζ. This illustrates why the larger scales in Figure 3.25 (c) and (d) are suppressed. Also, the low-pass filter effect of TIE on larger propagation distances is well illustrated.

In Section 2.2.4 we deduced CTF phase retrieval by expanding $e^{iS\phi_-}e^{-iS\phi_+} = 1 + S(\phi_- - \phi_+) + \mathcal{O}(S^2)\,.$ and truncating at linear order. Therefore, CTF is restricted to small values of S. Thus the question arises how the MTF changes for larger values of S.
In Figure 3.28 the MTF is plotted for $S = 0.5$ and $S = 1$, and in the CTF case we see peaks which increase for larger values of S. At these peaks the MTF can significantly exceed unity. This means that there are frequencies which are amplified by the CTF retrieval process.
TIE seems to be robust against phase scaling. This is not surprising due to the fact that TIE suppresses high spatial frequency and for low spatial frequency the diffractogram scales quite linearly (recall the first D-band for MOBS (Figure 3.24)).

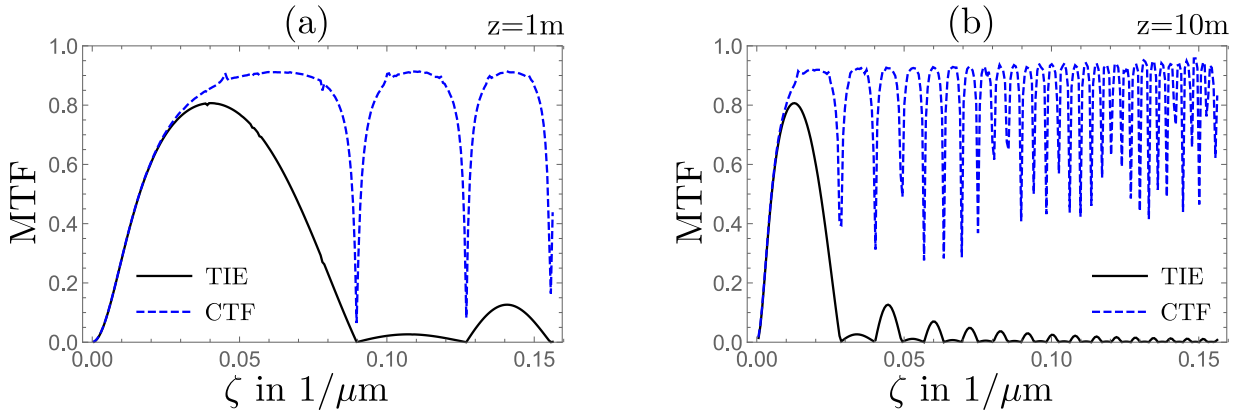

Figure 3.27.: Modulation transfer function (MTF) for $S = 0.1$, $E = 10$keV and the pixel size $\Delta x = 1.6\mu$m for the TIE (solid) and CTF (dashed) approach. (a): Propagation distance $z = 1$m. Note the small MTF at small values of ζ. (b): Propagation distance $z = 10$m. Note the low MTF in the TIE approach for high values of ζ.

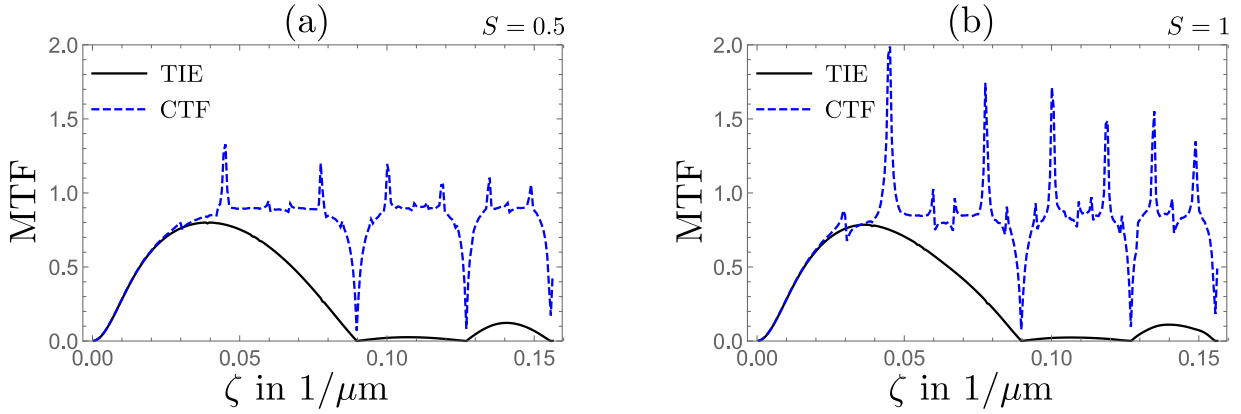

Figure 3.28.: Modulation transfer function (MTF) for $z = 1$m, $E = 10$keV and the pixel size $\Delta x = 1.6\mu$m for the TIE (solid) and CTF (dashed) approach. (a): $S = 0.5$. (b): $S = 1$. Note the peaks with MTF > 1 in the CTF case.

To investigate the peaks in the MTF for CTF retrieval at $S = 1$, we examine the first peak where the MTF exceeds unity exemplary (here at $\zeta = 0.045\frac{1}{\mu\text{m}}$). In Figure 3.29 (a) $|\mathfrak{F}g_z(\vec{\xi})|$ is plotted, and we can see at $|\xi_x| = \xi_1$, where ξ_1 corresponds to $\sigma/\pi = 1$, non-vanishing values of $|\mathfrak{F}g_z(\vec{\xi})|$. Due to the CTF method these frequencies get amplified and lead to higher harmonics of the assumed base base oscillation in the retrieved phase-map (See Figure 3.29 (b)). This indicates that CTF leads to artifacts in the retrieved phase-map when the original phase-map contains strong phase variations.

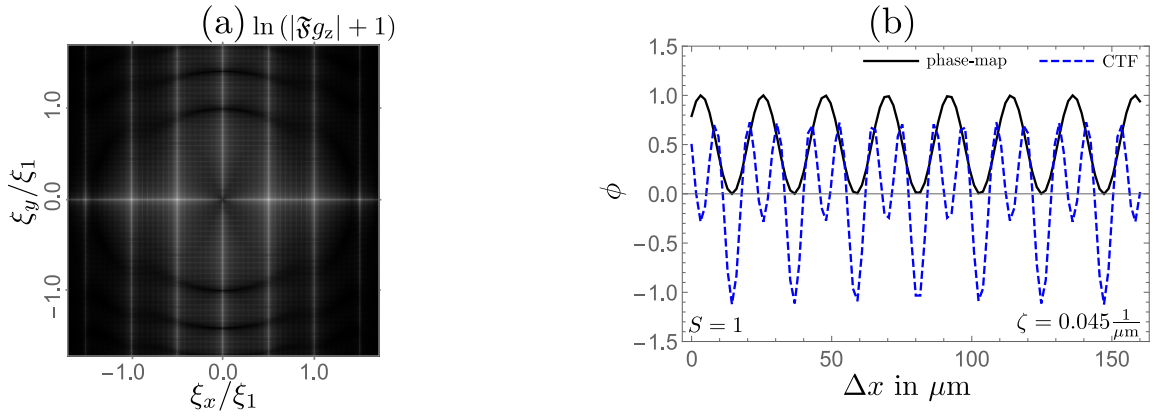

Figure 3.29.: CTF retrieval of sine phase-map at $S = 1$, $E = 10\text{keV}$, $z = 1\text{m}$ and $\zeta = 0.045\frac{1}{\mu\text{m}}$. (a): Representation of $|\mathfrak{F}g_z\xi_1|$ where ξ_1 corresponds to $\sigma/\pi = 1$. Note the high values of $|\mathfrak{F}g_z$ near $|\xi_x| = \xi_1$. (b): Cut through the original phase-map (solid) and CTF retrieved phase-map (dashed) parallel to the x-Axis. Note that the retrieved phase contains an additional oscillation and therefore is not even qualitatively correct.

These artifacts in CTF retrieval indicate the need of taking care of non-linear effects for the retrieval of large phase variations. As we know from previous investigations on scaling-linearity (recall Section 3.1.4, Section 3.2.2 and Section 3.3.2) we know that the most non-linear regions in the diffractogram are located around $\sigma/\pi = n$ with $n = 1, 2, \ldots$.
A pragmatic approach [25] to deal with this issue is to modify the intensity contrast by applying a filter in Fourier space, such that

$$\mathfrak{F}g_{z,\text{QP}}(\vec{\xi}) := \begin{cases} \mathfrak{F}g_z(\vec{\xi}) & \text{for } \sigma \leq \frac{\pi}{2}\,, \\ \Theta\left(|\sin(\sigma)| - \varepsilon\right) \cdot \mathfrak{F}g_z(\vec{\xi}) & \text{for } \sigma > \frac{\pi}{2}\,, \end{cases} \tag{3.70}$$

where Θ denotes the Heaviside step function and $0 \leq \varepsilon \leq 1$ is the threshold parameter for this binary filter.
We substitute Eq.(3.70) into Eq.(3.64) and obtain the quasiparticle[11] approach (QP)[25][22]

$$\mathfrak{F}\phi = \mathfrak{F}g_{z,\text{QP}}\frac{\text{sgn}(\sin\sigma)}{2|\sin\sigma| + \alpha}\,. \tag{3.71}$$

The MTF for the QP approach with $\varepsilon = 0.1$ is plotted in Figure 3.30. We see that the peaks are suppressed in comparison to CTF in Figure 3.28 (b). Therefore, the artifacts in the QP-reconstructed phase-map are suppressed, compare the retrieved phase-map at $\zeta = 0.045\frac{1}{\mu\text{m}}$ in Figure 3.30 (b) with Figure 3.29 (b).

The threshold parameter ε determines how well the peaks in the MTF, and therefore artifacts in the reconstructed phase-map, are suppress at the expense of sharpness. In Figure 3.31 the MTF of QP is plotted for $\varepsilon = 0$ (CTF), $\varepsilon = 0.2$ and $\varepsilon = 0.4$. We see stronger suppression of the peaks and loss of wider frequency bands at higher values of ε.
An exemplary visualization of a phase-map (Lena), retrieved by QP, is given in Figure 3.32. Note the suppression of artifacts for larger values of ε and also the significant loss of resolution and details at $\varepsilon = 0.99$.

[11] This name has been chosen in analogy to the quasiparticle concept [26] in the quantum theory of condensed-matter physics and quantum field theory. There a free dispersion law is altered by strong interactions yielding a free quasi particle. [25]

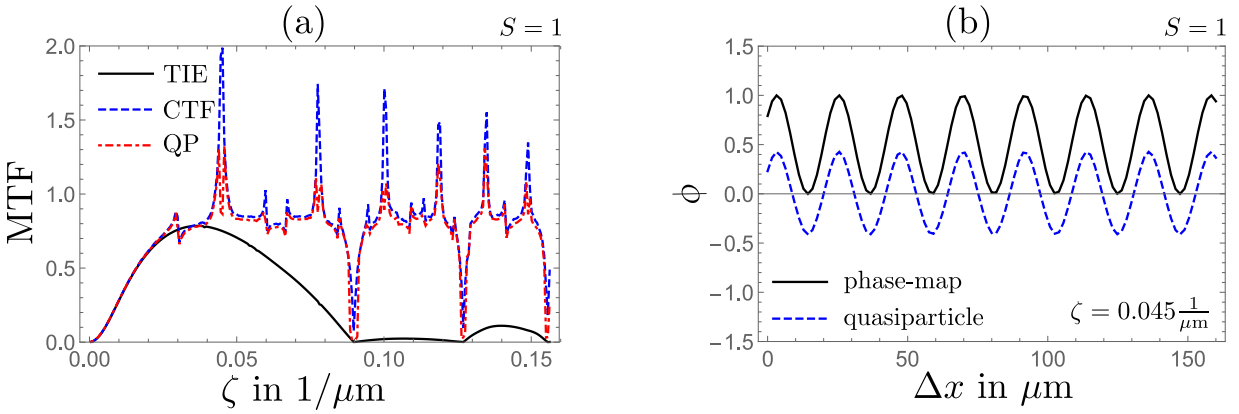

Figure 3.30.: (a): MTF for quasiparticle approach (QP) ($\varepsilon = 0.1$) at $z = 1$m, $E = 10$keV, $\Delta x = 1.6\mu$m, $S = 1$. Note that the spikes are suppressed in comparison to CTF in Figure 3.28 (b). (b): Cut through phase-map and QP reconstructed phase map parallel to x-axis for $\zeta = 0.045\frac{1}{\mu\text{m}}$. Note the qualitative improvement in comparison to Figure 3.29 (b).

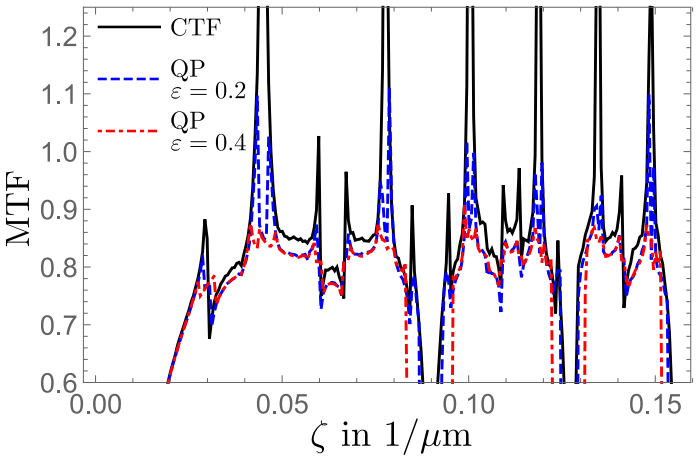

Figure 3.31.: MTF for CTF and quasiparticle approach (QP) ($\varepsilon = 0.2$, $\varepsilon = 0.4$) at $z = 1$m, $E = 10$keV, $\Delta x = 1.6\mu$m, $S = 1$.

Recall the D-bands in the MOBS case (see Figure 3.24), here we see that $D_{B,n}/\pi \geq 0.75$ for $n > 1$ so that the extent of the non-linear region is approximately $\bar{\sigma}_{\text{non-lin}} \approx 0.25$. Cutting out this region $\bar{\sigma}_{\text{non-lin}} = 0.25$, which is associated with the threshold parameter $\varepsilon = 0.38$, gives good suppression of MTF peaks and therefore suggests a reasonable QP phase-retrieval.

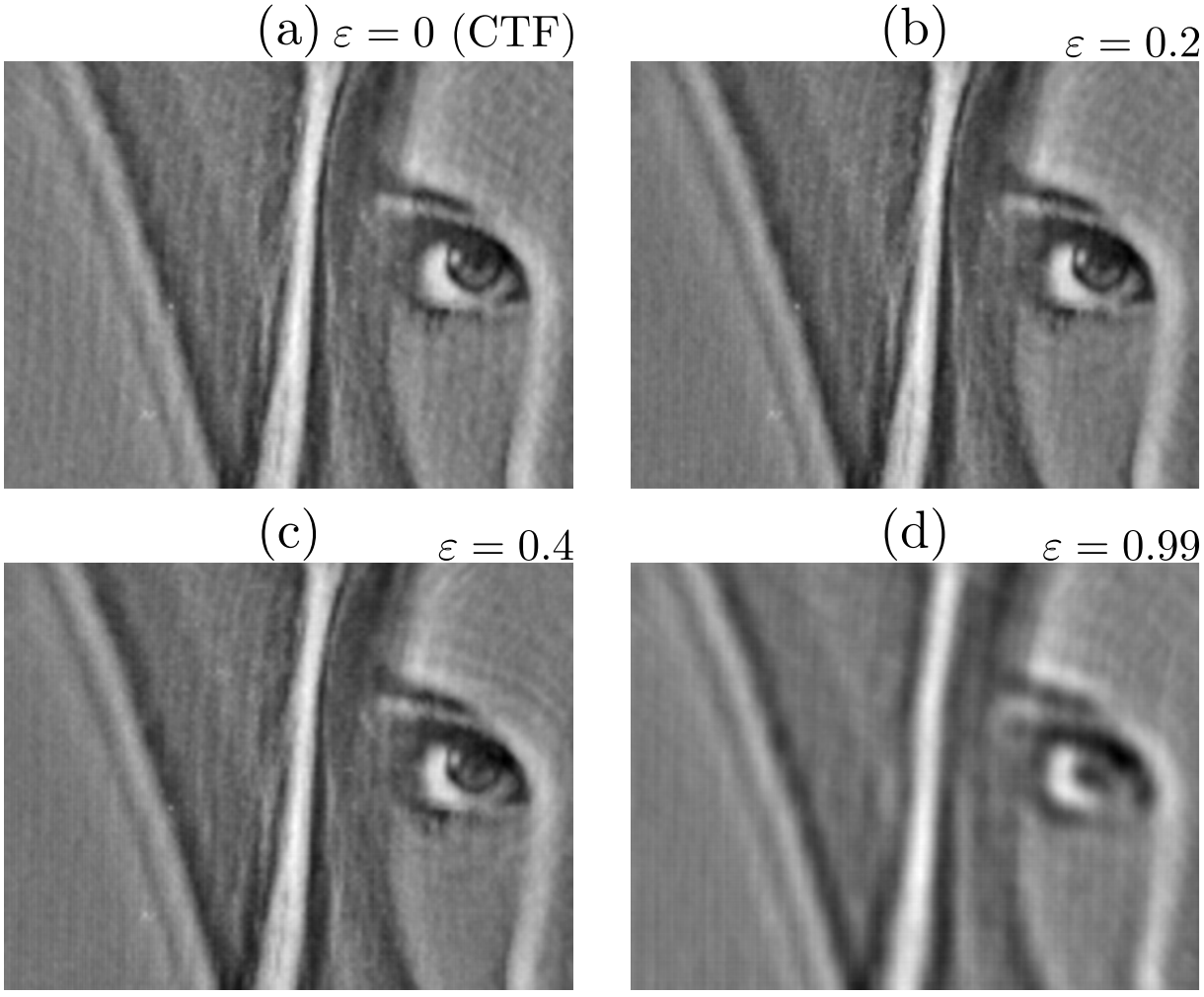

Figure 3.32.: Retrieved Lena phase-map (zoomed in) with quasiparticle approach. Propagation parameter: propagation distance $z = 10$m, energy $E = 10$keV, pixel size $\Delta x = 1.6\mu$m, $S = 1$. (a): $\varepsilon = 0$ which is equivalent to CTF. (b): $\varepsilon = 0.2$. (c): $\varepsilon = 0.4$. (d): $\varepsilon = 0.99$.

4. Conclusion

In this thesis we have investigated systematically the dependencies of a diffractogram (intensity-contrast spectrum) on propagated, initially phase-modulated wave fields, the associated propagation distance z and the strength of the phase variation. The main motivation for this was that in commonly applied single-distance phase-retrieval approaches (TIE and CTF) small phase variations and/or small values of z are assumed. For real objects this is not always guaranteed. In case of TIE a short propagation distance z is required, which in real experiments leads to a poor signal to noise ratio [27].

Shape of the diffractogram
In the local case, which occures in the far-field regime and for small phase variations, the diffractogram exhibits oscillatory behavior which arises due to sinusoidal contrast transfer. We have shown for Gaussian phase-maps, that in the near-field regime (large Fresnel number) and/or large phase variation the diffractogram transmutes critically into an over-damped shape. This behavior could also be identified for two-scale and multi-scale objects (e.g. as seen in the experimental data of [17]).
We also have investigated the movement of the first regular CTF zero σ_1 in the diffractogram under scaling of the phase variation strength. While for Gaussian phase-maps σ_1 moves to higher values under increases of the phase variation, we could construct two-scale phase maps, where σ_1 moves into the opposite direction. For multi-scale objects, we saw, that this effect is suppressed until the diffractogram (critically) assumes an over-damped shape.

Scaling linearity
We investigated the scaling linearity of diffractograms. For Gaussian phase-maps a single physical frequency modulus was identified where the diffractogram scales in a maximally linear way.
We also identified frequency bands D_B where the diffractogram exhibits good scaling linearity. We demonstrated for single-scale and two-scale phase-maps that the width of these bands depends on the shape of the phase-map and the Fresnel number. We also saw, independently of the phase-map, that the maximally non-linear scaling behavior occurs around the zeros/minima of the diffractogram (at integer values of σ/π). This is caused by the slightly movement of the zeros/minima compared to the CTF case.

Consequences for the phase-retrieval approaches

We compared TIE and CTF in dependence of the propagation distance and the phase-scaling. We showed that both approaches suffer from poor contrast in the retrieved phase-map for low spatial frequencies at small propagation distances. This can be explained by the fact that both approaches assume locality. But in fact, non-local effects are non-negligible in the near field and even can dominate the spectrum there (recall the transmutation into an over-damped shape of the diffractogram).

At larger propagation distances, the low frequency contrast improves, but TIE suffers from poor resolution. This is because for TIE, due to the expansion in powers of a small propagation distance, the high spatial frequencies are suppressed in the retrieved phase-map.

For stronger phase variation CTF causes artifacts due to an amplification of frequencies which are associated with non-linear scaling. This problem can be mitigated by the quasiparticle (QP) approach. We demonstrated that the bands of linear scaling D_B introduce a good binary threshold filter for QP phase-retrieval.

Appendix

A. Error estimations

This chapter contains the estimation of numerical uncertainties in Chapter 3.

A.1. Onion-shell expansion for Gaussian phase-map - error estimation

The onion-shell expansion contains an infinite summation in l see Eq. (2.80) and an infinite summations in k see Eq. (2.81). For numerical evaluation both of them need to be truncated at finite order. Therefore, we introduce the truncation L and c and thus obtain

$$\begin{aligned}\mathfrak{F}g_z = &\sum_{l=0}^{L} S^{2l}\frac{1}{(l!)^2}(1-\delta_{0,l})\mathfrak{F}\left[(\phi_-\phi_+)^l\right] \\ &+ 2S^{2l}\mathfrak{F}\left[(\phi_-\phi_+)^l\right] * \left(\sin\sigma \sum_{k=l}^{c}\frac{(-1^{k+l})S^{2(k-l)+1}}{(2k+1-l)!l!}\mathfrak{F}\left[\phi^{2(k-l)+1}\right]\right) \\ &+ 2S^{2l}\mathfrak{F}\left[(\phi_-\phi_+)^l\right] * \left(\cos\sigma \sum_{k=l+1}^{c}\frac{(-1^{k+l})S^{2(k-l)}}{(2k-l)!l!}\mathfrak{F}\left[\phi^{2(k-l)}\right]\right) .\end{aligned} \tag{A.1}$$

To estimate how fast Eq. (A.1) converges, with respect to L, we calculate $\frac{\mathfrak{F}g_{z,L+1}-\mathfrak{F}g_{z,L}}{\mathfrak{F}g_{z,L}}$.
In Figure A.1 $\frac{\mathfrak{F}g_{z,L+1}-\mathfrak{F}g_{z,L}}{\mathfrak{F}g_{z,L}}$, for Gaussian phase-maps, is plotted as a function of σ for various F_ω. We see, that the gained numerical accuracy which we obtain by adding the ninth onion-shell never exceeds 10^{-7}, 10^{-12} for $\sigma/\pi > 0.1$, respectively.

The second expansion we need to truncate is k at the order c. Two examples of the gained accuracy when increasing c by one are given in Figure A.2.

In the Sections 3.1.1 and 3.1.3, for numerical evaluations of diffractograms with $F_\omega \neq 0$ the first ten (zeroth to ninth) onion-shells ($L = 9$) and $c = 39$ was used. For the evaluations with $F_\omega = 0$, the zeroth onion-shell ($L = 0$) and $c = 39$ was used. Because of the good convergence we neglected an explicit error treatment for further going evaluations, as for example the description of the transition form damped to oscillatory behavior in Section 3.1.3.

A.2. Non linearity expansion for Gaussian phase-map - error estimation

For the determination of scaling linearity in Section 3.1.4 a non-linearity expansion (see Eq. (2.75)) has been performed and substituted into Eq.(3.27), using the phase-map Eq. 3.1. An onion-shell expansion would have been possible, too, but the numerigac evaluation for the non-linearity expansion is faster and the accuracy sufficient as we demonstrate in this section.
This non linearity expansion has one infinite sum, which needs to be truncated finite order c

$$e^{iS\phi_-}e^{-iS\phi_+} = \sum_{n=0}^{c}\frac{(iS)^n}{n!}\sum_{j=0}^{n}\frac{(-1)^j n!}{(n-j)!j!}\phi_-^{n-j}\phi_+^j . \tag{A.2}$$

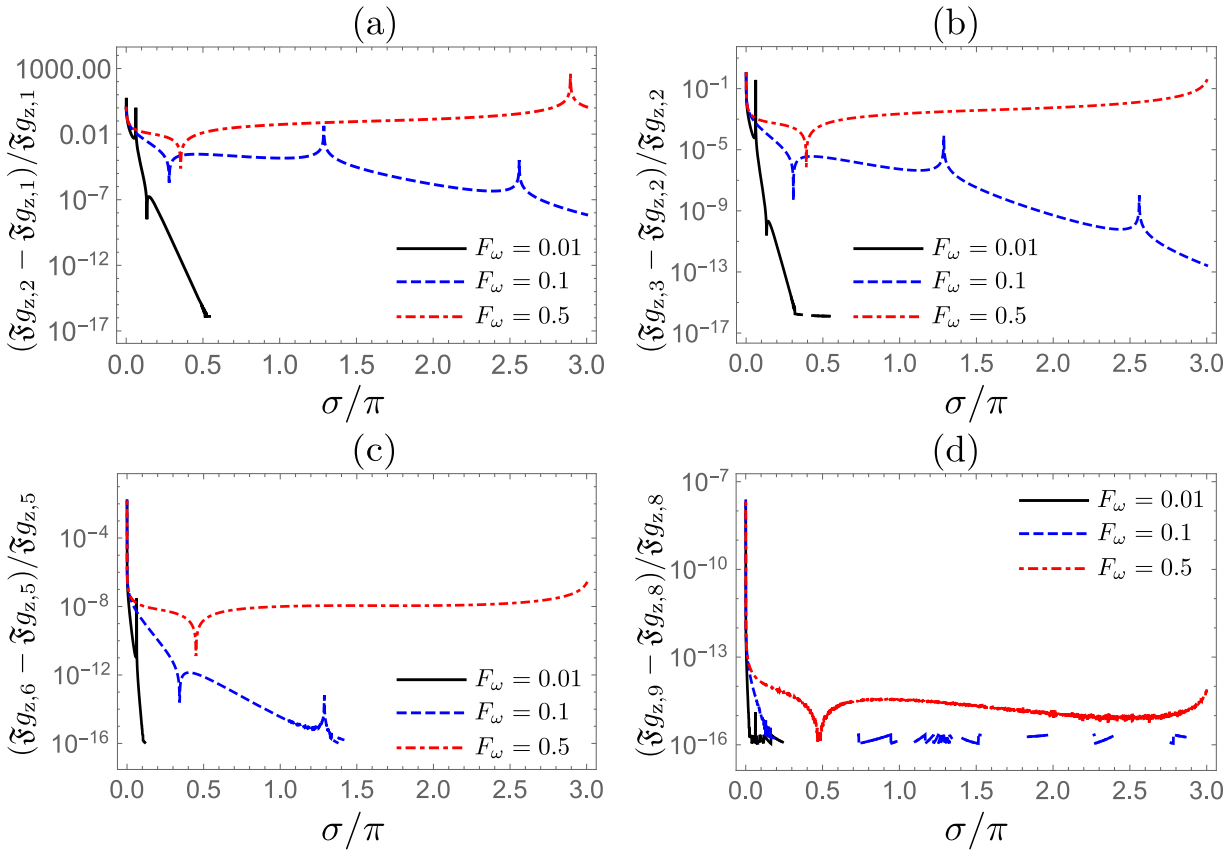

Figure A.1.: Accuracy estimation for numerical SOBS evaluation using the onion-shell expansion. Difference by adding the next onion-shell to a certain cut in l. All plots are functions of σ with $S = 1$, $c = 40$ at $F_\omega = 0.01$, $F_\omega = 0.1$ and $F_\omega = 0.5$. (a): $\frac{\mathfrak{F}g_{z,2} - \mathfrak{F}g_{z,1}}{\mathfrak{F}g_{z,1}}$, note the fast convergence at F_ω for larger values of σ. (b): $\frac{\mathfrak{F}g_{z,3} - \mathfrak{F}g_{z,2}}{\mathfrak{F}g_{z,2}}$. (c): $\frac{\mathfrak{F}g_{z,6} - \mathfrak{F}g_{z,5}}{\mathfrak{F}g_{z,5}}$. (d): $\frac{\mathfrak{F}g_{z,9} - \mathfrak{F}g_{z,8}}{\mathfrak{F}g_{z,8}}$.

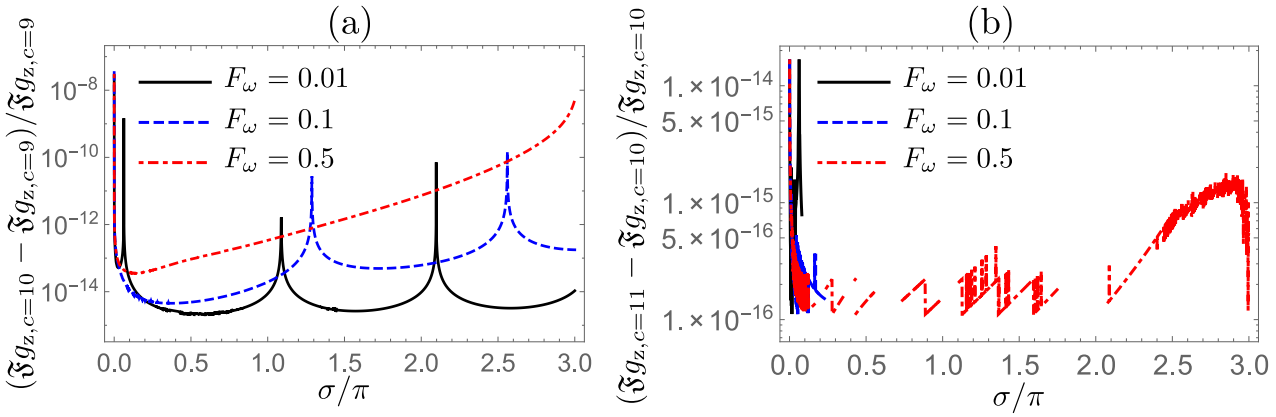

Figure A.2.: Accuracy estimation for numerical SOBS evaluation using the onion-shell expansion. Difference by increasing c by one. All plots are a function of σ with $S = 1$, $L = 9$ and at $F_\omega = 0.01$, $F_\omega = 0.1$ and $F_\omega = 0.5$. (a): $|\frac{\mathfrak{F}g_{z,c=10} - \mathfrak{F}g_{z,c=9}}{\mathfrak{F}g_{z,c=9}}|$. (b): $|\frac{\mathfrak{F}g_{z,c=11} - \mathfrak{F}g_{z,c=10}}{\mathfrak{F}g_{z,c=10}}|$.

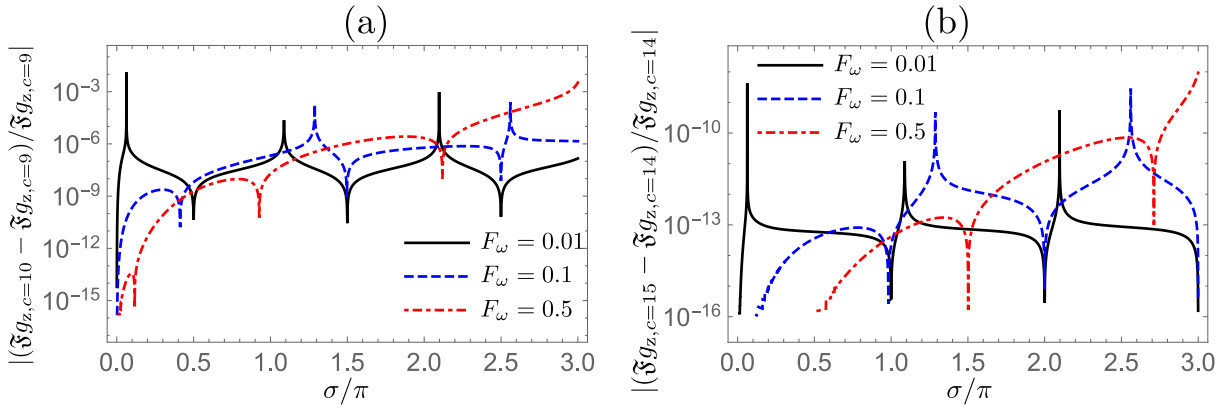

Figure A.3.: Accuracy estimation for numerical SOBS evaluation using the non-linearity expansion by investigating the difference in $\mathfrak{F}g_z$ when increasing c by one. (a): $\left|\frac{\mathfrak{F}g_{z,c=10}-\mathfrak{F}g_{z,c=9}}{\mathfrak{F}g_{z,c=9}}\right|$ (b): $\left|\frac{\mathfrak{F}g_{z,c=15}-\mathfrak{F}g_{z,c=14}}{\mathfrak{F}g_{z,c=14}}\right|$

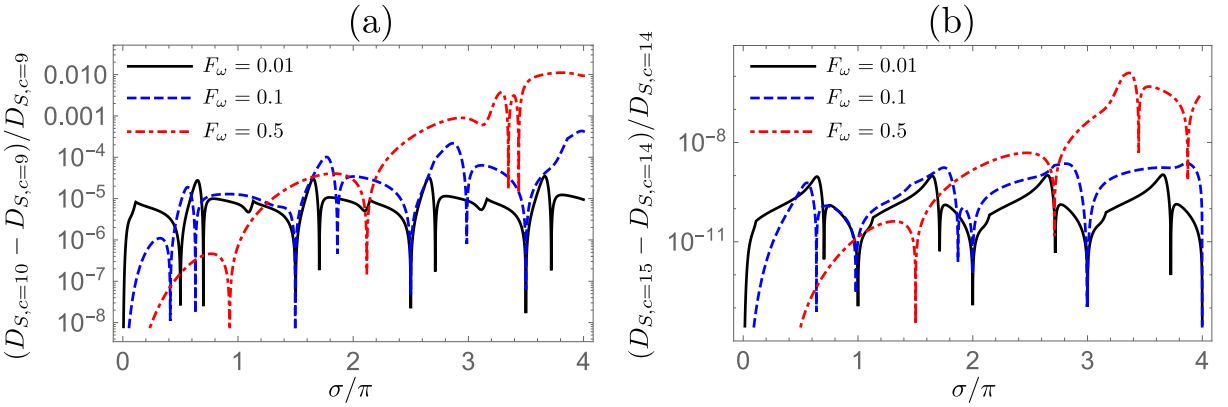

Figure A.4.: Accuracy estimation of D_S (Gaussian SOBS) by investigating the difference in D_S when increasing c by one. (a): $\left|\frac{D_{S,c=10}-D_{S,c=9}}{D_{S,c=9}}\right|$ (b): $\left|\frac{D_{S,c=15}-D_{S,c=14}}{D_{S,c=14}}\right|$

In Figure A.3 the difference of $\left|\frac{\mathfrak{F}g_{z,c}-\mathfrak{F}g_{z,c-1}}{\mathfrak{F}g_{z,c-1}}\right|$ for $c = 10$ (a) and $c = 15$(b) is plotted as a function of σ. This also is done for D_S (for definition see Eq.(3.27)) in Figure A.4. In Section 3.1.4 we used $c = 15$. We can see in Figure A.3 and Figure A.4 that a high precision precision is archived due to this truncation and therefore we can neglect further error treatment here.

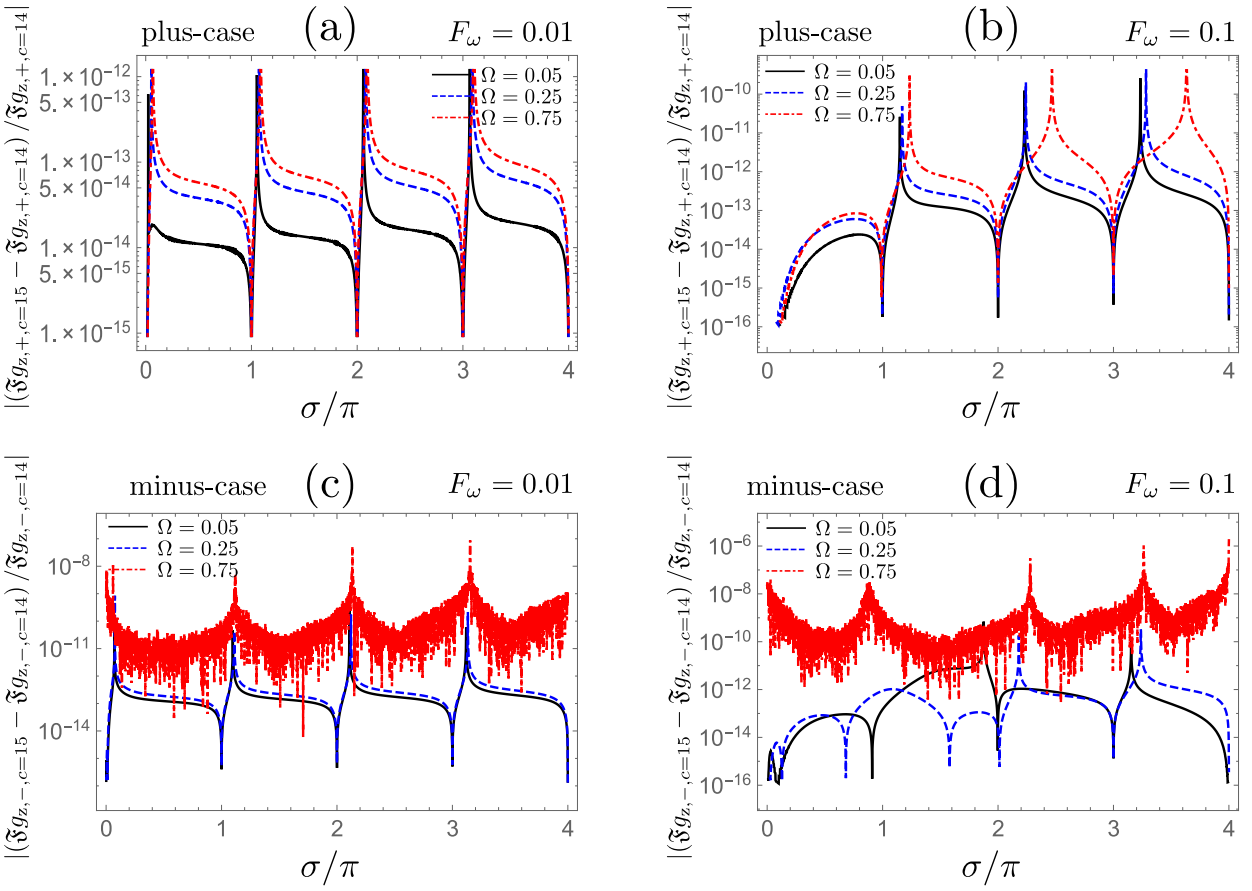

Figure A.5.: Accuracy estimation of $\mathfrak{F}g_z$ (TOBS) by investigating the difference in $\mathfrak{F}g_z$ when increasing $c = 14$ to $c = 15$ $\left(\left|\frac{\mathfrak{F}g_{z,c=15} - \mathfrak{F}g_{z,c=14}}{\mathfrak{F}g_{z,c=14}}\right|\right)$. (a): Plus-case at $F_\omega = 0.01$. (b): Plus-case at $F_\omega = 0.1$. (c): Minus-case at $F_\omega = 0.01$. (d): Minus-case at $F_\omega = 0.1$. All cases are plotted for $\Omega = 0.05, 0.25, 0.75$.

A.3. Non-linearity expansion for TOBS - error estimation

For the numerical evaluation of TOBS the non-linearity expansion Eq. (3.34) has been used with a truncation at the order $c = 15$. To estimate the accuracy of this truncation we investigated the gain in accuracy when increasing $c = 14$ to $c = 15$ (analogue to Section A.2).

In Figure A.5 the difference of $\left|\frac{\mathfrak{F}g_{z,c=15} - \mathfrak{F}g_{z,c=14}}{\mathfrak{F}g_{z,c=14}}\right|$ is plotted for the plus- and minus-case and the second scale factor $\Omega = [0.05, 0.25, 0.75]$. We see that the gained accuracy never exceeds 10^{-5}. In Section 3.2 $C = 15$ is used and therefore, it justifiable to neglect further error treatment due to this truncation.

Analog $\left|\frac{D_{z,c=15} - D_{z,c=14}}{D_{z,c=14}}\right|$ is plotted in Figure A.6. The gained accuracy never exceeds $1 \cdot 10^{-3}$, so we can assume sufficient accuracy for $c = 15$, which we used in Section 3.2.

A.4. D_S-function (MOBS) - error estimation

In Section 3.3.2 D_S is introduced for discrete and numerical calculated diffractograms. The accuracy of D_S is determined by the number N, and therefore determining the scaling steps $\delta S = \frac{S_2 - S_1}{N}$, of diffractograms used to calculate the derivatives. For the evaluations of MOBS D_S in this thesis $N = 100$ has been used.
To estimate the N-dependence $\frac{D_{S,N=200}(\sigma) - D_{S,N=100}(\sigma)}{D_{S,N=100}}(\sigma)$ is plotted in Figure A.7. We see, that the improved accuracy by doubling N to $N = 200$ never exceeds 0.03. This implies good convergence of D_S in N and justifies the use of $N = 100$ in our evaluations.

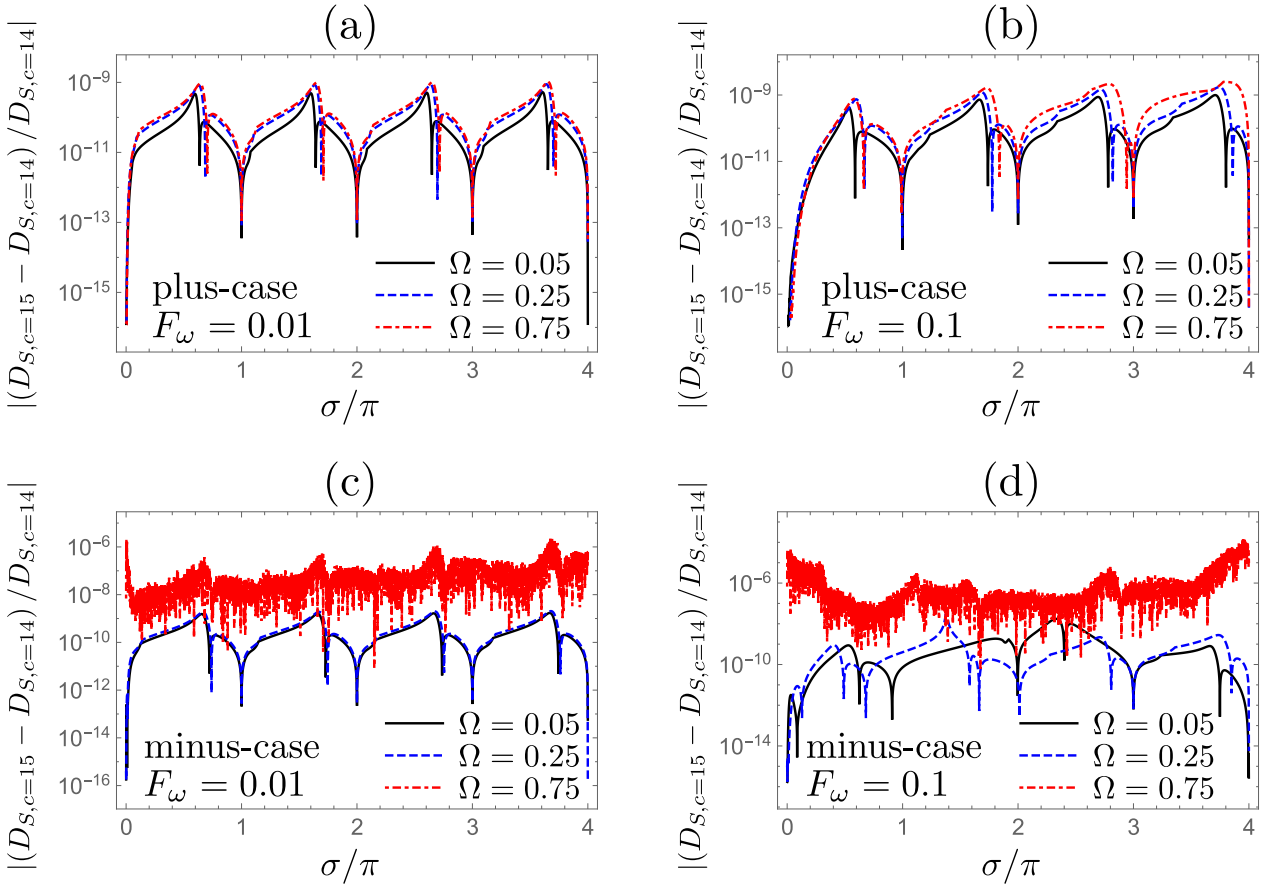

Figure A.6.: Accuracy estimation of D_S (TOBS) by investigating the difference in D_S when increasing $c = 14$ to $c = 15$ $\left(\left|\frac{D_{S,c=15}-D_{S,c=14}}{D_{S,c=14}}\right|\right)$. (a): Plus-case at $F_\omega = 0.01$. (b): Plus-case at $F_\omega = 0.1$. (c): Minus-case at $F_\omega = 0.01$. (d): Minus-case at $F_\omega = 0.1$. All cases are plotted for $\Omega = 0.05, 0.25, 0.75$.

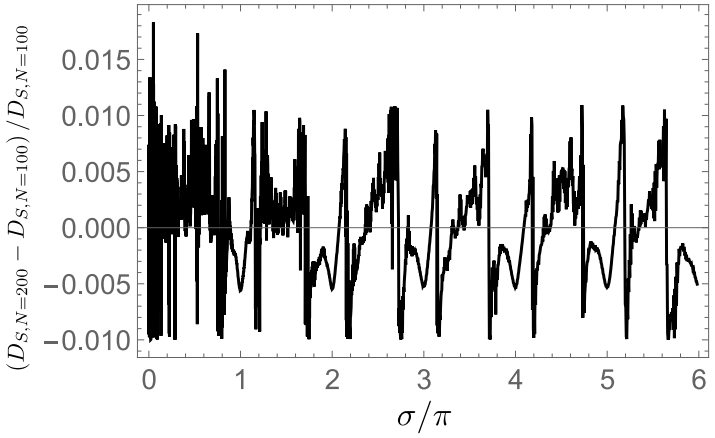

Figure A.7.: Accuracy estimation of D_S (MOBS). The diffractograms of Lena phase-map (1024×1024 pixel) with $E = 1$keV, $z = 1$m and $\Delta x = 1.6\mu$m in the scaling-window $S = [0, 1.5]$ was used to calculate D_S. Here the normalized difference of D_S under the change from $N = 100$ to $N = 200$ is plotted $(\frac{D_{S,N=200}-D_{S,N=100}}{D_{S,N=100}})$. Note that $\max\left(\frac{D_{S,N=200}(\sigma)-D_{S,N=100}(\sigma)}{D_{S,N=100}}(\sigma)\right) - \min\left(\frac{D_{S,N=200}(\sigma)-D_{S,N=100}(\sigma)}{D_{S,N=100}}(\sigma)\right)$ does not exceed 0.03. Therefore implies sufficient convergence.

Bibliography

[1] W.C. Röntgen. *Eine neue Art von Strahlen*. Number Bd. 1 in Collection Léo Pariseau. Stahel, 1896.

[2] P. K. Spiegel. The first clinical X-ray made in America - 100 years. *American Journal of Roentgenology*, 1995.

[3] Computed tomography : From photon statistics to modern cone-beam ct, 2008.

[4] J. Radon. Über die Bestimmung von Funktionen durch ihre Integralwerte längs gewisser Mannigfaltigkeiten. *Akad. Wiss.*, 69:262–277, 1917.

[5] François Arago, Christiaan Huygens, and Thomas Young. *The Wave Theory of Light: Memoirs of Huygens, Young and Fresnel*. Nabu Press, 2010.

[6] B.L. Henke, E.M. Gullikson, and J.C. Davis. X-ray interactions: Photoabsorption, scattering, transmission, and reflection at e = 50-30,000 ev, z = 1-92. *Atomic Data and Nuclear Data Tables*, 54(2):181 – 342, 1993.

[7] J.C. Maxwell. *A treatise on electricity and magnetism*. Number Bd. 2 in A Treatise on Electricity and Magnetism. Dover Publications, 1954.

[8] John David Jackson. *Classical electrodynamics*. Wiley, New York, NY, 3rd ed. edition, 1999.

[9] Hermann Hankel. *Zur allgemeinen Theorie der Bewegung der Flüssigkeiten*. Dieterische Univ. Buchdruckerei, Göttingen 1861.

[10] G. Kirchhoff. Zur Theorie der Lichtstrahlen. *Annalen der Physik*, 254(4):663–695, 1883.

[11] J.-P. Guigay. Fourier transform analysis of fresnel diffraction patterns and in-line holograms. *Optik 49, 121*, 1977.

[12] T.E. Gureyev, Ya.I. Nesterets, D.M. Paganin, A. Pogany, and S.W. Wilkins. Linear algorithms for phase retrieval in the fresnel region. 2. partially coherent illumination. *Optics Communications*, 259(2):569 – 580, 2006.

[13] P. Cloetens. *Contribution to phase contrast imaging, reconstruction and tomography with hard synchrotron radiation: Principles, Implementation andApplications*. PhD thesis, Vrije Universiteit Brussel, 1999.

[14] M. Krenkel. *Cone-beam x-ray phase-contrast tomography for the observation of single cells in whole organs, Ph.D. thesis,*. PhD thesis, Georg-August-Universität Göttingen, 2015.

[15] D. Paganin. *Coherent X-Ray Optics*. Oxford Series on Synchrotron Radiation. OUP Oxford, 2013.

[16] K. A. Nugent, T. E. Gureyev, D. F. Cookson, D. Paganin, and Z. Barnea. Quantitative phase imaging using hard x rays. *Phys. Rev. Lett.*, 77:2961–2964, Sep 1996.

[17] S. Hahn, Y. Müller, R. Hofmann, J. Moosmann, O. Öktem, L. Helfen, J.-P. Guigay, Th. van de Kamp and T. Baumbach. Spectral transfer from phase to intensity in fresnel diffraction. *Phys. Rev. A 93, 053834*, 2016.

[18] I. N. Bronstein, K. A. Semendjajew. *Taschenbuch der Mathematik*. Verlag Harri Deutsch Thun und Frankfurt (Main), 1984.

[19] Yannick Müller. Low-frequency part of diffractogram induced by single-scale phase map via free-space propagation. Bachelor thesis, 2016.

[20] Otto Mildenberger. *Grundlagen der Systemtheorie für Nachrichtentechniker*. Carl Hanser Verlag München Wien, 1981.

[21] Southern California, Signal USC University o. ; Image Processing Institute,Ming Hsieh Department of Electrical E. Girl (Lena, or Lenna), 512x512 pixels, 768kB, Color (24 bits/pixel). `http://sipi.usc.edu/database/database.php?volume=misc&image=12`, Version: 1972.

[22] Julian Moosmann. *Nonlinear approaches to the inverse problem of phase retrieval from single-measurement X-ray intensity data*. Dr. Hut, München, 2015.

[23] John W. Coltman. The specification of imaging properties by response to a sine wave input. *J. Opt. Soc. Am.*, 44(6):468–471, Jun 1954.

[24] John C. Feltz and Mohammad A. Karim. Modulation transfer function of charge-coupled devices. *Appl. Opt.*, 29(5):717–722, Feb 1990.

[25] Julian Moosmann, Ralf Hofmann, and Tilo Baumbach. Single-distance phase retrieval at large phase shifts. *Opt. Express*, 19(13):12066–12073, Jun 2011.

[26] LD Landau. The theory of a fermi liquid. *Soviet Physics Jetp-Ussr*, 3(6):920–925, 1957.

[27] Ralf Hofmann, Alexander Schober, Steffen Hahn, Julian Moosmann, Jubin Kashef, Madeleine Hertel, Venera Weinhardt, Daniel Hänschke, Lukas Helfen, Iván A. Sánchez Salazar, Jean-Pierre Guigay, Xianghui Xiao, and Tilo Baumbach. Gauging low-dose x-ray phase-contrast imaging at a single and large propagationdistance. *Opt. Express*, 24(4):4331–4348, Feb 2016.

Acknowledgments

At the end of my thesis I would like to thank all those people who made this thesis possible.

At first I would like to thank my thesis advisor PD Dr. Ralf Hofmann for the continuous support of my research, for his patience, motivation, and all the good scientific discussions we had. The cooperation during the last year was a very instructive experience. His guidance helped me in all the time of research and writing of this thesis.

Also, I would like to thank Steffen Hahn for the introduction to the preliminary work, the numerical tools and the gainful discussions we had.

My sincere thanks also goes to Prof. Baumbach for his support and the opportunity to write my thesis at IPS.

I also place on record, my sense of gratitude to my friends, who directly or indirectly, have supported me during the writing.

Finally, I would like to express my gratitude to my parents Beate Trost and Markus Trost for providing me with unfailing support and continuous encouragement throughout my years of study and through the process of writing this thesis.